University of Hertfordshire

Centre for Astrophysics Research

Submitted in partial fulfilment of the requirements of the University of Hertfordshire for the degree of Master of Science by Research

Accretion Disc Structure of Supermassive Stars Formed by Collisions

Author:

Katarzyna Nowak

30th September, 2021

Advisors:

Dr habil. Martin G. H. Krause
Centre for Astrophysics Research
University of Hertfordshire

Dr Timothy Gledhill
Centre for Astrophysics Research
University of Hertfordshire

Nowak, Katarzyna:
Accretion Disc Structure of Supermassive Stars Formed by Collisions
Submitted in partial fulfilment of the requirements of the University of Hertfordshire for the degree of Master of Science by Research, University of Hertfordshire, 2021.

Abstract

Globular clusters (GCs) display large variations in light elements; the main one being O-Na, C-N and Mg-Al anticorrelations. Additionally most GCs demonstrate multiple sequences in the colour-magnitude diagram, proving that globular clusters host multiple stellar populations. It has been suggested that the second population forms from the hot-hydrogen burning yields of the first population, which then also explains the chemical peculiarities via self-enrichment. One of the leading proposals for the polluter is a supermassive star (SMS) ($\gtrsim 10^3$ $M_\odot$), which forms via runaway collisions, simultaneously with the globular cluster [Gieles et al., 2018].

At the present time it is very hard to observe a SMS due to its location. The candidate forming massive clusters are located outside the Milky Way with very dense centers, where the SMS would be obscured by gas and dust. One way to detect it could be the use of MASER, where 22.2 GHz H_2O, water masers, are in general associated with massive star formation. Gorski et al. [2018] found a very strong MASER, a kilomaser in the nearby galaxy NGC 253 associated with a young massive cluster.

A SMS disc is perturbed by stellar flybys, inspiralling and colliding stars. I investigate what the predicted MASER spectrum of that disc looks like using 2D hydrodynamic simulations and compare this to the W1 kilomaser in NGC 253. The simulations are modelled using the finite volume fluid dynamics code PLUTO starting from the standard Disk-Planet problem. I derive model maser spectra from the final simulations by using the general maser model from Kartje et al. [1999] for appropriate disc temperatures against velocity along the line of sight.

The model maser spectra for the most destructive case for the simulations of M_{SMS} = 1000 $M_\odot$ are a good match with W1 kilomaser spectrum obtained from Gorski et al. [2018], in terms of scaling, flux values and some of the signal trends. For the more massive star of 10,000 $M_\odot$ the spectra start to resemble megamasers from AGNs rather than stellar masers. I have also observed changes in flux values for "high-velocity" features and their outwards and inward movement due to the presence of a dense spiral arm, rotating around the central star.

Acknowledgments

First and foremost I would like to thank my supervisor, Dr Martin Krause. Without his remarkable insight, patience and support this thesis would not be possible. I would also like to thank the University of Hertfordshire for allowing me to use their computing facilities.

A sincere thank you to Calum Morris for his diligent proofreading of this thesis.

Finally I would like to thank my family and friends for always being supportive and helping me through tough times.

Contents

List of Figures

List of Tables

1. Introduction

Globular clusters (GCs) were traditionally believed to be simple, single population objects born in one coeval formation event and were not subjected to any internal chemical evolution. Nevertheless those ancient clusters have puzzled astronomers for decades. For example, the 2nd parameter problem [Sandage and Wildey, 1967] arose in the 1960's when a sample of globular cluster colour-magnitude diagrams revealed that GCs with the same metallicity have different horizontal branch morphologies. GCs' with peculiar chemical compositions, including large variations in certain elements, were detected already in the 1970's [Osborn, 1971], however their origins were then assigned to internal deep mixing processes as a consequence of the evolution of stars. Nevertheless spectroscopic measurements in the 2000's showed that all the Galactic and extra-galactic globular clusters host multiple stellar populations and display similar ratios of elements [Krause et al., 2020]. To explain this abnormal chemical makeup, an extremely hot, supermassive star (SMS) was suggested to account for the strange composition of GCs [Denissenkov and Hartwick, 2014; Gieles et al., 2018]. The SMS is believed to be of a mass of at least 10^3 $M_\odot$ and it is expected to form simultaneously with the globular cluster, usually in a very dense central region with lots of collisions and fly-bys. It is unclear if fly-bys and stellar collisions could disturb any accretion disk and if a large molecular column would survive in a disk. Supermassive stars are extragalactic objects, surrounded by gas and dust, resulting in higher extinction. On top of that with such a high effective temperature of around 40,000 K, the star would be classified as blue, emitting in EUV radiation. Hence it is very hard to observe those massive objects. An alternative method to detect them could be MASER emission, where GHz MASERs are often associated with a massive star formation [Krause et al., 2020]. Recently a high-resolution spectrum became available - a nuclear kilomaser found in the nearby galaxy NGC 253 linked to a young massive cluster [Gorski et al., 2018].

It is therefore important to clarify how the predicted spectrum of an SMS disc with the expected disturbance would look like. I address this issue by modelling the accretion disc around a supermassive star using the hydrodynamic code - PLUTO; with the inspiralling and/or accreted objects being added to simulate the formation of a SMS via runaway collision.

The report starts with the overview of star cluster formation and its evolution, the overview of the chemical anomalies observed in globular clusters, as well as proposed possible polluters responsible for those peculiarities in Chapter 2. This chapter also includes a framework for the formation of a SMS as well as its evolution and MASERs as a possible way to detect SMSs. In Chapter 3, I give a step-by-step summary of hydrodynamics modelling that will be used for this project, as well as how the maser spectrum is derived. I present the results in Chapter 4 for every intermediate step as well as for the final simulation, followed by the discussion of those results in Chapter 5. The conclusion and future work are outlines in Chapter 6.

2. Background

2.1 Cluster formation and evolution

2.1.1 The beginning of star formation in molecular clouds

Star clusters form in dense molecular clouds with hierarchical structures, consisting mostly of molecular hydrogen. It has been proposed that the properties of the clouds influence the early structure and kinematics of star clusters that are being formed as a result of gravitational collapse. Currently there are two paradigms explaining the onset of the star formation: the gravoturbulent (GT) one and global hierarchical collapse (GHC) [for a review see: Krause et al., 2020]

In the former, the supersonic non-thermal motions detected in the molecular clouds are explained as supersonic turbulence stirred by external forces like supernova explosions, bipolar outflows etc. In the GT scenario, turbulence supports the clouds globally against self-gravity, whilst locally it produces shocks that in turn generate small-scale fluctuations in density. Those density enhancements can become Jeans unstable and collapse, forming sheets, filaments and clumps. Therefore the gravoturbulent scenario is stationary, meaning the cloud is in approximate virial equilibrium between turbulence and self-gravity [Klessen et al., 2000].

By contrast, the GHC scenario is chaotic, and is best described as a system of collapses within collapses [Vázquez-Semadeni et al., 2017], meaning that all scales accrete from their parent structures. A cloud that is acquiring a mass larger than its Jean's mass is approaching the pressureless regime and thus collapses. Such conditions also amplify initial anisotropies, driving a large-scale collapse along the shortest axis first, creating sheets, which then contract along their shortest dimensions, producing filaments [Lin et al., 1965]. Within those newly-formed structures, there is a growth of roundish density fluctuations, clumps or hubs, which have a faster collapse timescale than the other parts of filaments. Therefore the filaments act as 'rivers' funneling material from large to small scale, because of the clump's deeper gravitational potential [Vázquez-Semadeni et al., 2019]. Initially the star formation rate (SFR) in the GHC scenario is increasing as a consequence of the growth in

density, which allows larger fraction of mass to have shorter free-fall than its parent structure. The low mass stars first appear after several Myr after the beginning of global contraction. It is worth mentioning that the maximum limit on the mass of the star is influenced by the instantaneous mass of the hub where the star forms. The capped value increases, as the mass in the hub increases, therefore there is a delay by several Myr in the formation of the massive star over the low-mass stars. Eventually the SFR decreases due to the feedback from the massive stars, and that happens over around 10 Myr [Krause et al., 2020].

2.1.2 Accretion Models

Star formation is not an isolated event, as most stars formed as members of a star cluster, and as such are not necessarily bound [Lada and Lada, 2003; Krumholz et al., 2019]. They can stay bound to the original group of stars or later drift apart from it. Accretion discs are a standard feature of star formation for all masses. The models of accretion presented below are based on the properties of cores containing protostars as well as the disk-protostar relationship and models focusing on feedback. In reality, the accretion is driven by a range of non-linear processes and therefore the models are divided as such purely for convenience.

Core-regulated models assume that collapsing gas proceeds efficiently from scales of ~ 0.1 pc to 0.1 au; essentially the protostellar accretion rate is equal to the infall rate. That would infer that the only environmental variable that influences accretion is the local gas temperature. In the simplest models, only thermal pressure and gravity is taken into consideration, showing that accretion is independent of stellar mass. Yet, cores are observed to be both magnetised, moderately turbulent and are often asymmetric. Turbulent core model and competitive accretion models take those characteristics into account and both predict that the stellar accretion increases with the stellar mass. However this is not observed and the core-regulated models fall somewhere between the limits of constant accretion rate and constant star formation time [Krause et al., 2020]. As the core-regulated model falls short of observations, that suggest that the mass does not accrete smoothly from the outer envelope onto the protostar, but in more variable manner facilitated by an accretion disk.

This leads to the second class of theoretical models, disc-regulated accretion. The disc acts as a repository for high-angular momentum gas. The mechanisms responsible for the redistribution of mass within the disc is an area of ongoing research. The current research indicates the most plausible main processes are: viscous torques as a result of turbulence triggered by the magnetorotational instability and gravitational torques induced by gravitational instability [Krause et al., 2020]. Episodic accretion can also be caused by thermal-viscous instability, gravitational fragmentation and infall of disc fragments onto the protostar [Audard et al., 2014].

The feedback-regulated accretion model emphasises the role the stellar feedback plays in influencing the accretion process. The feedback in the form of ionising radiation, winds and outflow can disperse star-forming gas therefore ultimately halting the accretion or reducing the mass available for accretion [Krause et al., 2020].

2.1.3 Star cluster evolution

Protostars, formed in less than a core free-fall time, are clumped in subclusters. Here the local formation efficiency is high, therefore subclusters of protostars virialise in their own potentials resulting in contraction. Subsequently they merge with each other forming a dense, self-gravitating stellar cluster, enclosed in lower density gas [Moeckel and Clarke, 2011]. For the case of globular cluster formation, Gieles et al. [2018] considered a cluster of protostars with a stellar mass of $M \simeq 10^5$ $M_\odot$ with a half-mass radius of $R_h \simeq 2.3$ pc; those quantities refer to the values at the start of gas accretion. The resulting dynamical time is $\tau_{dyn} \sim (GM/R_h^3)^{-1/2} \simeq 0.16$ Myr, where G is the gravitational constant. Hence at this point the cluster is considered as a single entity. Moeckel and Clarke [2011] have proven that in the populous, dense cluster, collisions play an important role and lead to the runaway collisions that form a large object with the mass exceeding 30 $M_\odot$. Interestingly they argue that the densest star cluster in the Milky Way, the Arches, is still not big enough for this to happen. They prove that in the smaller star forming regions collisions do not play an important role, therefore the mass accretion process proceeds only via an accretion disk. However this may not hold true for massive star clusters, where collisions may hold an important role.

Once the star formation is terminated and the parental gas has been transformed into stars and any remaining gas dispersed, the cluster becomes exposed. To understand the mechanism for the disruption of the gas it is worth looking at gas expulsion and slow gas clearance.

In the definition of Hills [1980] primordial gas expulsion removes more than half of the total mass from the cluster in a quick manner. Some or most of the stars can become unbound and escape and as a consequence lead to the young cluster being dissolved. In the case of massive clusters the gas expulsion is propelled by supernovae and more importantly by stellar winds, that produce thin shell bubbles [Krause et al., 2013]. Kuhn et al. [2019] have used the data obtained from Gaia Data Release 2 to study kinematics of a sample of 28 young stellar groups with masses up to 10^4 $M_\odot$. The study has revealed that at least 75% of their objects have positive expansion velocities, ranging up to 2 km s^{-1}, therefore expansion of the system is commonly seen. The data provides direct evidence that gas expulsion aid the likelihood of immediate dispersion of stars formed in compact massive star forming regions.

One mechanism how slow gas clearance can be realised is through the indirect radiation pressure on dust, that smoothly expands the gas, and thereafter that same pressure expels the gas, on the dynamical timescale. This is expected to be less efficient than stellar winds but with comparabable magnitudes [Crocker et al., 2018].

Once the gas has been removed from the cluster, by either accreting onto stars or due to the removal by feedback, stellar cluster winds can form as a product of the gas being heated faster than it can cool. In order for the stellar winds to play crucial role in the cluster evolution, it needs to contain a significant amount of massive stars. The gas freed by the stellar winds and supernovae accumulates mass and energy into the gas reservoir, in which the cluster is embedded [Krause et al., 2020].

The fate of the cluster at this stage is governed by gravity as well as stellar evolution. The latter one drives a decrease of the total mass in the cluster, leading to a reduction of the binding energy and therefore an increase of the cluster radius [Hills, 1980].

The tidal shocks of passing molecular gas clouds or transient spiral arms lead to the expansion and disruption of the cluster by accelerating its stars and increasing its total energy. This leads to the expansion and cluster dissolution [Spitzer, 1958]. Collisional dynamics or so-called two-body relaxation play an important role from the very beginning of cluster evolution. They occur frequently and last long because of the relatively low velocity of stars, ~ 10 km s^{-1}, and high stellar densities, $\sim 10^{4-6}$ pc^{-3}. The two-body relaxation process will equalize kinetic energy between stars, hence massive stars will have lower velocity to match the kinetic energy of the low mass stars. That leads to the mass segregation, where massive stars are found closer to the centre of the cluster [Krause et al., 2020].

2.2 Globular cluster

2.2.1 Chemical anomalies

Globular clusters compared to the open clusters are massive ($\gtrsim 10^5$ M$_\odot$) and generally are older than 1 Gyr, with the oldest GC having an age of > 13 Gyr. Therefore they are survivors from the early Universe [Krause et al., 2020]. Additionally most GCs demonstrate multiple sequences located in colour-magnitude diagram. The main-sequence broadening is considered as a result of a spread in helium abundance (ΔY), proving that globular clusters host multiple stellar populations [Bastian and Lardo, 2018; Milone et al., 2018].

Most globular clusters show no spread in iron abundance but display a similar maximum sodium enhancement. Helium abundance spreads vary ($\Delta Y \approx 0.013$ - 0.035) from cluster to cluster, but are generally low [Bastian et al., 2015; Bastian and Lardo, 2018; Milone et al., 2018].

GCs display large variations in light elements: Na-O, C-N and Mg-Al anticorrelations. Still the most noticeable feature in most globular cluster is the Na-O anticorrelation (see Fig. 2.1). A hot-hydrogen burning environment is needed to vary those abundances with the concurrent p-capturing reactions of the CNO-cycle ($\gtrsim 20$ MK), NeNa ($\gtrsim 45$ MK) and MgAl ($\gtrsim 70$ MK) chains leading to the rise of those anticorrelations [Gratton et al., 2012].

Most models, seeking to explain the anomalies in globular clusters, refer to self-enrichment, where certain stars, polluters, within a cluster are capable of enriching other stars within the same cluster. It is also vital to include in the models how the observed amount of sodium can be produced, and therefore be accreted by the low mass stars in the GCs; a requirement that multiple generation models struggle to meet, an issue generally referred to as the 'mass budget problem' [Bastian and Lardo, 2018; Gieles et al., 2018].

2.2.2 Possible polluters

In order to explain the above-mentioned anomalies three potential polluters have been proposed: AGB, fast-rotating massive star (FRMS) and a supermassive star.

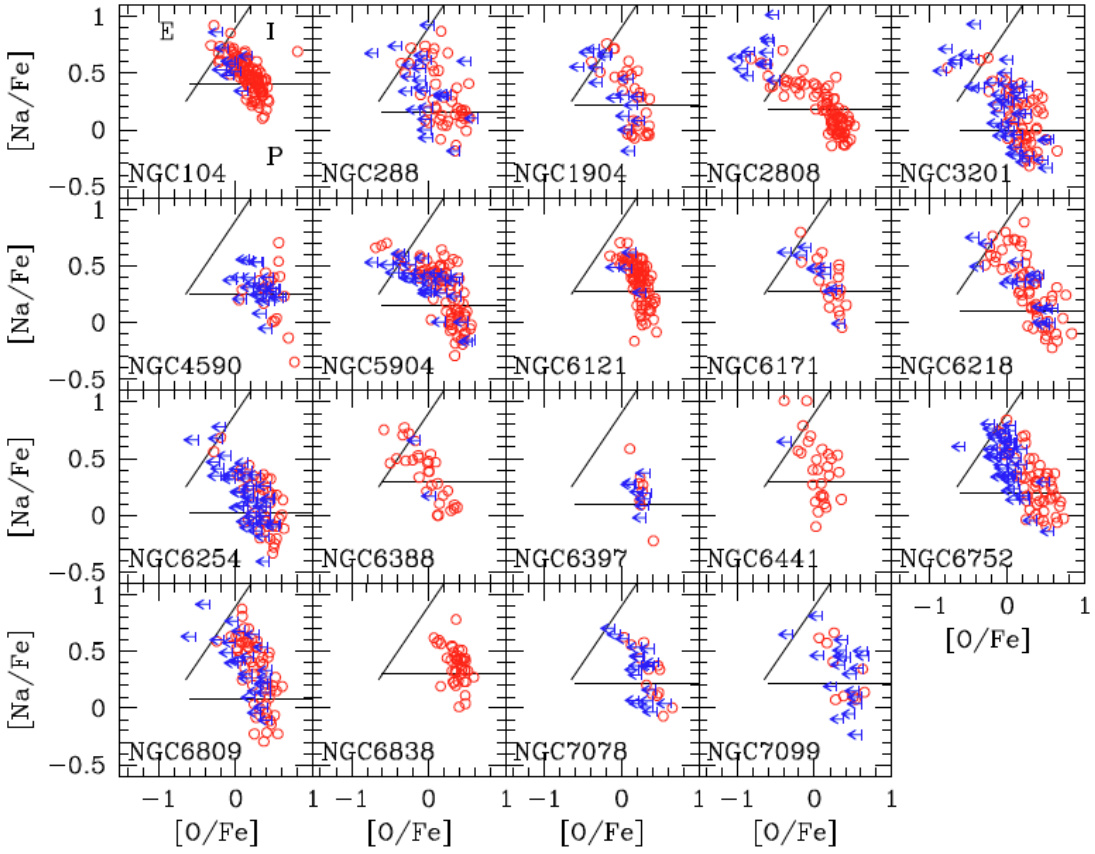

Figure 2.1: A collection of the Na-O anticorrelation observed in a sample of 19 GCs, as part of FLAMES survey. Red circles indicate measurements for both O and Na, and blue arrows for Na but only upper limits for O. The lines separate the first (P) and second generation (I and E) [Carretta et al., 2010]

The nucleosynthesis of the first two proposed polluters does not correspond to the ones of GCs. AGB stars display O-Na correlation instead of the anticorrelation observed, furthermore it releases He-burning products, that are not widely detected in GCs. FRMSs on the other hand are able to produce Mg-Al anticorrelations but simultaneously would show a strong He enrichment [Bastian and Lardo, 2018; Krause et al., 2020].

The essential central temperature to activate MgAl chain is reached by a supermassive star at the very beginning of its evolution when the abundance of He is still low. Thereupon, in its early evolutionary phase, the H-burning products show agreement with various anticorrelations observed in the GCs [Denissenkov and Hartwick, 2014]. The SMS is assumed to be fully convective and therefore releases the material at the very beginning of the main sequence phase in a radiatively driven wind. The ejecta would then mix with star-forming gas that either accretes onto proto-stars or collapses to form stars independently [Krause et al., 2020].

Gieles et al. [2018] propose that the SMS forms via runaway collisions, simultaneously with the globular cluster; therefore the SMS pollutes the cluster gas and consequently the low-mass protostars during the cluster formation.

2.3 Supermassive star

Globular clusters are the ideal environment for a SMS to form. As the proto-GC contracts and accretes gas onto protostars it allows for the stellar collisions [Moeckel and Clarke, 2011]. In the following, we summarise the SMS formation model from Gieles et al. [2018]. The runaway collisions need to occur before two-body relaxations halts the adiabatic contraction of the cluster. Therefore the number of stars in GC must be $\gtrsim 10^6$ with the gas accretion rate of $\gtrsim 10^5$ $M_\odot$ Myr^{-1}. The cluster will only be able to form a supermassive star if the runaway collision process will occur before the end of the contraction stage [Gieles et al., 2018].

The relation between mass and radius for SMSs is very uncertain therefore it has been adopted from Crowther et al. [2010] for stars with masses $\sim$ 90 - 130 $M_\odot$:

$$r_{\rm SMS} = 30 R_\odot \left(\frac{m_{\rm SMS}}{100 M_\odot}\right)^{\delta} \tag{2.1}$$

with $0 < \delta \lesssim 1$ for $m_{\rm SMS} > 100$ $M_\odot$ and $\delta = 0.5$ for $m_{\rm SMS} < 100$ $M_\odot$. The luminosity of a SMS, $l_{\rm SMS}$, after incorporating the ratio $\Gamma = l_{\rm SMS}/l_{\rm Edd} = 0.75$ is:

$$l_{\rm SMS} \simeq 2.8 \times 10^6 L_\odot \frac{m_{\rm SMS}}{100 M_\odot}. \tag{2.2}$$

Taking both Eqns. 2.1 and 2.2 with the Stefan-Boltzmann law, the effective temperature expression becomes:

$$T_{\rm eff} \simeq 43 {\rm kK} \left(\frac{m_{\rm SMS}}{100 M_\odot}\right)^{1/4-\delta/2} \tag{2.3}$$

where the δ-dependence suggests a mass-independent $T_{\rm eff}$ for $\delta = 0.5$ and for larger values of δ the supermassive stars are cooler than a star of 100 $M_\odot$.

In order to discuss the mass growth of a SMS, it is worth defining the collisional rate a star with mass $m_{\rm SMS}$ and radius $r_{\rm SMS}$ experiences:

$$\dot{N}_{\rm coll} = 2\sqrt{2\pi} \left(\frac{m_{\rm SMS} + m}{m_{\rm SMS}}\right)^{1/2} n V_{\rm rms} d^2 \left(1 + \frac{G m_{\rm SMS}}{d V_{\rm rms}^2}\right), \tag{2.4}$$

in a system with stellar number density n, velocity dispersion $V_{\rm rms}$, with other stars with mass m and radius r. The distance at which the collisions happens is defined as $d = r + r_{\rm SMS}$. The final term in the brackets has an input due to the geometrical cross-section of the star and a contribution due to gravitational focusing. The latter one dominates in the case of stellar collisions, enhancing the cross-section of stars [Hills and Day, 1976].

From the Eqn. 2.4 it can be seen that the cross-section and collisional rate increases after a collision between stars, due to the product of the interaction having larger mass and radius. Therefore one very massive star forms as a consequence of continuous collisions with the growth rate of:

$$\dot{m}_{\rm SMS}^{\rm coll} \simeq 2\sqrt{2\pi} G m_{\rm SMS} r_{\rm SMS} \frac{\rho_{\rm c}}{V_{\rm rms}}, \tag{2.5}$$

where it is linearly dependent on ρ_c, central mass density of the cluster. The time-scale for the growth of the SMS is defined as:

$$\tau_{\dot{m}_{\rm SMS}} = \frac{1}{2\sqrt{2\pi}Gr_{\rm SMS}}\frac{V_{\rm rms}}{\rho_c}. \tag{2.6}$$

Gieles et al. [2018] adopted initial values for a SMS before the accretion: $m_{\rm SMS} = 5\ {\rm M}_\odot$ with a radius of $r_{\rm SMS} = 6.7\ {\rm R}_\odot$. Therefore for the initial conditions of the model, when the contraction starts, the time-scale is around 1680 Myr. As the cluster of protostars contracts due to the accretion of gas onto the protostars, the ratio ${\rm V_{rms}}/\rho_c \propto {\rm M}^{-8}$, makes the SMS growth timescale really short.

By ignoring feedback from binaries, the model would allow the mass of the SMS to be as large as the mass of the cluster (i.e. everything collapses onto the SMS). However the predicted exponential growth of the $\rm m_{SMS}$ will not occur. In high stellar densities, triple interactions or tidal capture would cause the stars to become bound to the SMS. Consequently binary systems would heat the surrounding stars in interaction and shrink the binary orbit, causing the star to collide with the SMS. Those binaries will decrease the rate of collisions before reaching equilibrium. The growth rate of the SMS as a result of the collisions from coalescence following binary formation and hardening is:

$$\dot{m}_{\rm SMS}^{\rm coll,rel} = \zeta\frac{r_{\rm SMS}}{m_{\rm SMS}}\frac{M^2}{R_{\rm h}\tau_{\rm rh}}, \tag{2.7}$$

with M being the total mass of the cluster with half-mass radius $R_{\rm h}$, the half-mass relaxation time-scale $\tau_{\rm rh}$ and $\zeta \simeq 0.1$. Comparing this expression with Eqn. 2.5, it can be noted that this collision rate is less dependent on the properties of the SMS but rather on the amount of energy that can be transported by two-body relaxation [Gieles et al., 2018].

The mass of SMSs also increases as a result of gas accretion, but it is assumed to be non-dominant in the model, since the model assumption is that a SMS can be formed from collision alone. Therefore the rate of growth is given by

$$\dot{m}_{\rm SMS} = \dot{m}_{\rm acc} + \min\left(\dot{m}_{\rm SMS}^{\rm coll}, \dot{m}_{\rm SMS}^{\rm coll,rel}\right), \tag{2.8}$$

where $\dot{m}_{\rm acc}$ is the rate of growth due to gas accretion, it is not so well constrained and hence is conservatively assumed to be low. The second term contains both equations 2.5 and 2.7, where equation 2.5 dominates before $\dot{m}_{\rm SMS}^{\rm coll,rel} < \dot{m}_{\rm SMS}^{\rm coll}$, meaning when the growth is regulated by relaxation. After that the SMS rate of growth is expressed by equation 2.7. As the SMS is a hot massive star therefore it will loose mass via stellar winds. The mass-loss rate relation estimated below takes into consideration the fact that a SMS may be out of equilibrium for much of its lifetime, if it will capture stars at a rate of $\gtrsim$ one per 10^3 yr:

$$\dot{m}_{\rm wind} = {\rm A}\left(\frac{m_{\rm SMS}}{100{\rm M}_\odot}\right)^{\eta}. \tag{2.9}$$

Here, ${\rm A} = 10^{-4}\ {\rm M}_\odot\ {\rm yr}^{-1}$ and $10^{-5}\ {\rm M}_\odot\ {\rm yr}^{-1}$ depending on SMS metallicity; $\eta = 0.75$ for constant $T_{\rm eff}$ and $\eta = 1.5$ for the increasing mass-loss rate whilst the He value increases [Gieles et al., 2018].

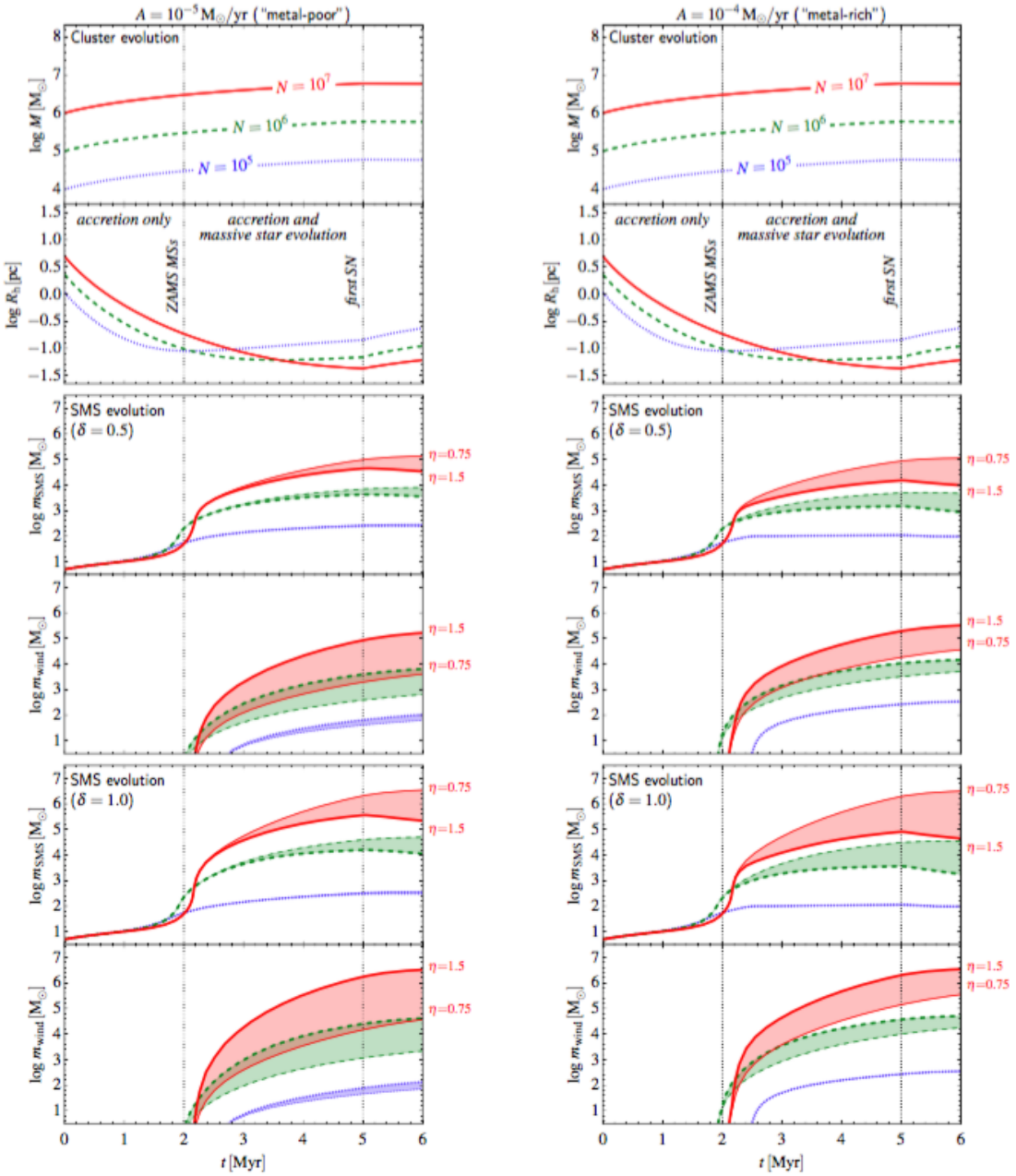

Figure 2.2: Gieles et al. [2018] model for SMS formation in a GC. Gas accretion and cluster contraction begins at t = 0. First massive stars > 10 $M_\odot$ reach ZAMS at t = 2 Myr and the first SNe is also indicated. The left side presents the result for the metal-poor case and the right-side for the metal-rich one.

Taking into account the previously mentioned expressions describing the properties of the SMS, Gieles et al. [2018] have solved the coupled ordinary differential equations and the results are visualised in Fig. 2.2. The parameters δ, A and η are the most uncertain, therefore different values are included. The top two panels correspond to the evolution of the cluster mass and half-mass radius, for different values of N (number of stars). The rest of the panels show $m_{\rm SMS}$ and $m_{\rm wind}$ for varied parameters. It can be seen in the figure that larger δ value increases the values of $m_{\rm SMS}$ and

$m_{\rm wind}$, since that parameter affects mass-radius relation (Eqn. 2.1). Hence the larger the radius and cross-section are, the more frequent collisions in the early phases.

The so-called 'conveyor belt' production of material processed via SMS, overcomes the mass-budget problem. The 'conveyor belt' can be summarised with time-scales for each production step as:

$$\tau_{\rm conv} \lesssim \tau_{\rm NaO} \ll \tau_{\dot{m}_{\rm SMS}} < \tau_{\rm He}. \tag{2.10}$$

Here $\tau_{\rm conv}$ is a convection flow time-scale ($\leq$ yr), since a SMS is a fully convective star, and is shorter than a time-scale for nuclear reactions, $\tau_{\rm NaO} \sim$ yr, responsible for production of the anticorrelations. The main-sequence lifetime for the full conversion of hydrogen into helium is longer: $\tau_{\rm He} \sim$ 0.2-2 Myr. Those nuclear products are transported throughout the SMS by convection and therefore partly ejected via stellar winds. After each collision a SMS is being constantly refurnish with material with low He content with the time-scale $\tau_{\dot{m}_{\rm SMS}} \sim$ 0.1 Myr. In order for this model to work in practice, the mechanism needs to stop before a SMS pollutes the cluster with He-burning products [Gieles et al., 2018].

2.4 MASER

At the present time it is very hard to observe a SMS due to its location: probably in the very dense centre of the forming massive star cluster. One way to detect it could be the use of a MASER, which is a unique tool to probe star-forming regions. The main maser line associated with those environments is water maser: H_2O 6_{16} - 5_{23} (22.2 GHz). According to Gray et al. [2016] dense gas ($> 10^7$ cm^{-3}) and temperature value larger than 300 K is required for the emission to arise if the species is to be collisionally pumped. Alternatively, background infrared radiation with temperature of around 1000 K is needed for the line to be radiatively pumped. Hagiwara et al. [2001] classifies the water maser according to its luminosities:

1. the stellar class: L $<$ 0.1 L$_\odot$,
2. kilomasers: 0.1 L$_\odot$ $<$ L $<$ 1 L$_\odot$,
3. megamasers: L $>$ 20 L$_\odot$.

Elitzur et al. [1991] worked out equations of physics for saturated maser, where the wavelength λ for the water maser transitions is $\approx$ 1.35 cm and the source brightness temperature is $T_b \approx 10^{12} a_{10}^3$, where $a_{10} = a/10$, and a defines the effective aspect ratio:

$$a = \frac{l}{\sqrt{A/\pi}}. \tag{2.11}$$

For a larger than a few the maser is saturated. The half-length of the maser emission region that lies in a disk along the line of sight is defined as l, D is the distance to the source with the observed area A. Hence for a saturated maser, the emission flux does not depend on the density and the temperature of the medium.

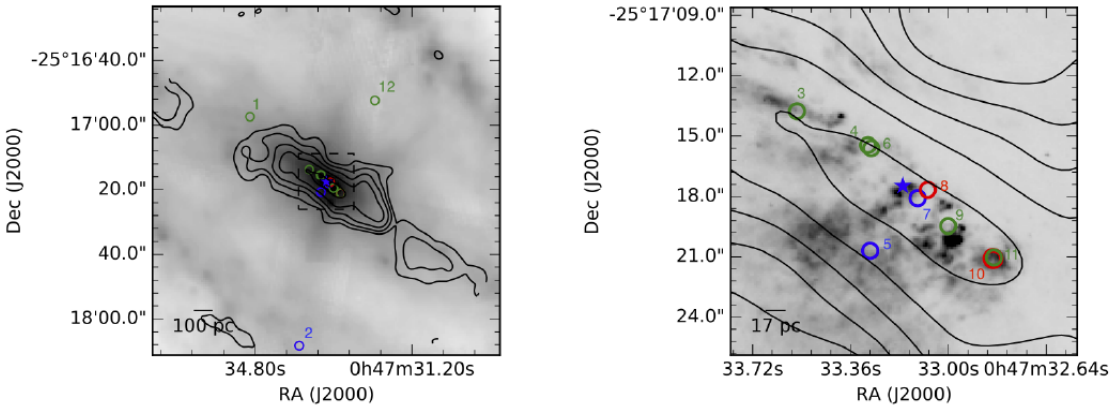

Figure 2.3: Positions of all the water masers detected in NGC 253 galaxy by Gorski et al. [2018]. The H_2O kilomaser, W1, is marked by the blue star. Green masers consistent with velocities of the molecular bar are indicated by green colour, redshifted and blueshifted masers are plotted in red and blue respectively. Both maps show ALMA ^{12}CO (1-0) contours with intensity of 60, 120, 240 and 480 Jy beam^{-1} km s^{-1} [Bolatto et al., 2013]. Left: IRAC 8μm image [Dale et al., 2009] of the central $\sim$ 1500 pc of NGC 253. Right: The nuclear 300 pc of the galaxy indicated in the box on the left panel. The image is the HST WFPC2 Hα map from Watson et al. [1996].

Kartje et al. [1999] adopted this maser physics to derive the flux equation to model AGN maser discs. They started with the relation of flux to intensity, I, and Ω, the solid angle subtended by the source as F=IΩ. Knowing that the area, A=D$^2\Omega$ then:

$$F = \frac{2kT_b}{\lambda}\frac{A}{D^2} \tag{2.12}$$

where k is Boltzmann constant. Substituting the above mentioned expression for T_b, k, λ and a, aspect ratio, Kartje et al. [1999] derived the equation for measured flux as:

$$F = 4.7 \times 10^{17} a_{10} \left(\frac{l}{D}\right)^2 \text{Jy} \tag{2.13}$$

Gorski et al. [2018] found a very strong MASER, nuclear kilomaser in the nearby galaxy NGC 253 associated with a forming super star cluster (see Fig. 2.3). The spectrum of the W1 kilomaser with luminosity of 1.02 $\pm$ 0.01 $L_\odot$ is shown in the Figure 2.4 (left) with its many velocity components ranging across $\sim$ 170 km s^{-1}.

In order to understand if the accretion disc of the supermassive star could potentially produce a water maser it is worth looking at conditions in which the 22.2 GHz H_2O lines are mased in the circumnuclear region of an active galactic nucleus (AGN). Figure 2.5 shows schematic illustration of the observed water masers positions in NGC 4258. The best conditions for maser are located near the inner edge of the torus along the line of sight and in the two tangential sections of the molecular torus, where there is a low velocity shear [Murayama and Taniguchi, 1997].

The flux density of the W1 nuclear kilomaser is around 85 $\pm$ 1.3 mJy/beam, which is of an order of one or two magnitudes lower than megamasers from AGNs in NGC

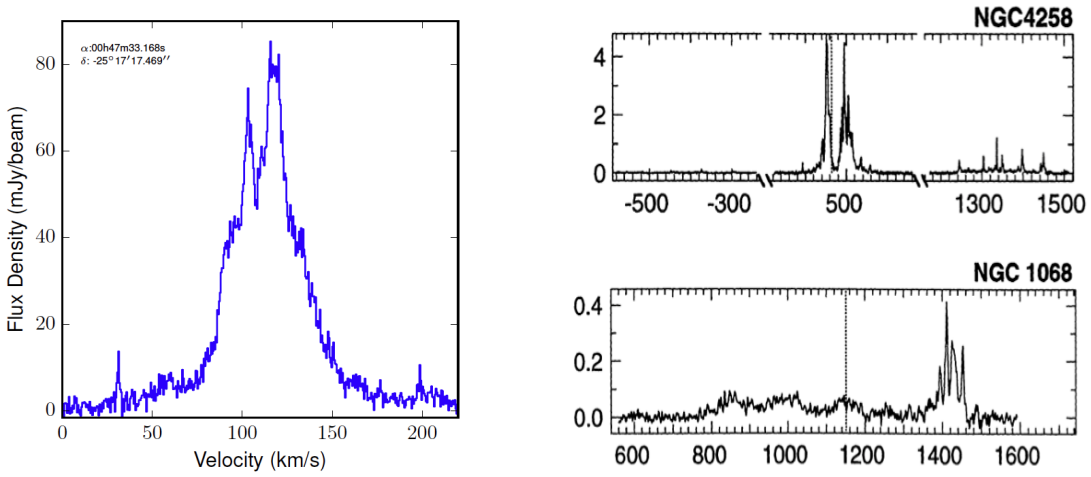

Figure 2.4: Left: Spectrum of W1, nuclear kilomaser detected in NGC 253 Gorski et al. [2018]. Right: Spectrum of the H_2O megamasers in the nucleus of NGC 4258 (top; Greenhill et al. [1995]) and NGC 1068 (bottom; Greenhill et al. [1996]) taken with the Effelsberg 100 m antenna in February 1993. Vertical axis indicates Flux Density (Jy) and horizontal one, Velocity (km/s) and the dotted vertical line indicates systemic velocity.

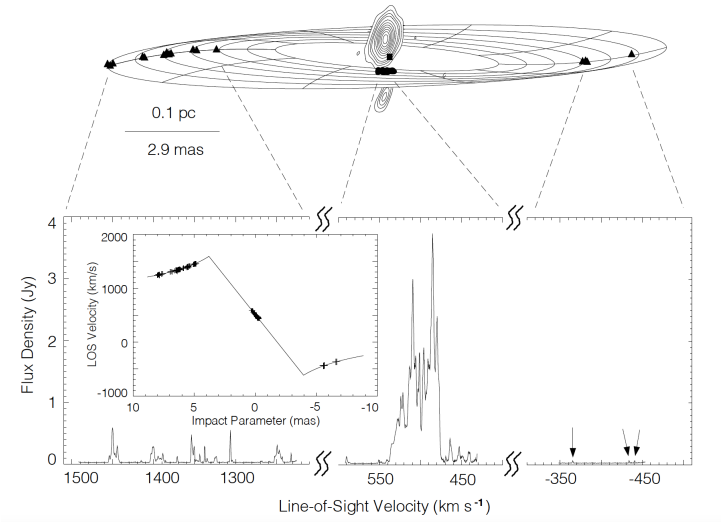

Figure 2.5: Actual maser positions measured by the VLBA in NGC 4252 with the warped disk model. The filled triangles mark the positions of the high-velocity masers, whilst the systemic masers are indicated by filled circles. The inset displays maser data fitted on the plot of line-of-sight velocity versus impact parameter for the best-fitting Keplerian disk [Herrnstein et al., 1999].

4258 and NGC 1068 (see right Fig. 2.4), but it shows some similarities like many velocity components, hence W1 spectrum is almost a blend between the two AGN spectra. Additionally those three spectra are 'clean' disk masers [Pesce et al., 2015], showing at least two of the three sets of maser components: systemic, blueshifted and redshifted features (see Fig. 2.5). The systemic feature, defined also as 'low-velocity', is a result of masing arising along a line of sight through the central part of the disk.

In terms of megamasers and AGN those features correspond to the recession velocity of the galaxy. Blue- and red-shifted features, called 'high-velocity' arise from the midline of the accretion disk, where the line of sight is tangent to the orbital motion. The high-velocity features are offset to the either side of the systemic velocity in the spectrum [Pesce et al., 2015]. Apart from the flux density, another component that distinguishes both megamasers and W1 kilomaser in Fig. 2.4 is that at least one set of features is offset from the systemic velocity by 300 km/s for megamaser, in comparison for the kilomaser, where it is around 83 km/s.

Figure 2.6 compares the W1 kilomaser with water masers from different type of sources, including AGNs, massive young stellar objects (MYSOs) and other kilomaser, associated with other forming super star clusters. I have extracted this data from various references given in the Figure legend. The data is also displayed in Table 2.1. The relationship between luminosity and velocity spread is super-linear, and kilomasers including W1 kilomaser are somewhat in the middle between massive YSOs and AGNs. Therefore it is beneficial to deduce the properties of W1 kilomaser source, masing disk, taking into account the properties of the other mentioned source types.

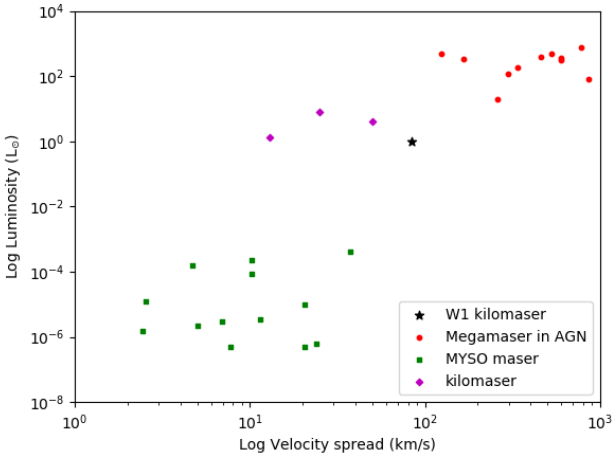

Figure 2.6: Luminosity versus velocity spread plot for water masers from different sources. Red circles indicate megamasers from AGN sources, green one denotes stellar masers from massive young stellar objects (MYSOs), purple circles show kilomasers and the black star is the W1 kilomaser. See Table 2.1 for references.

Table 2.1: H_2O masers in different astronomical sources. Kilomasers have their host galaxy indicated in the brackets in the first column. All the stellar masers are from massive young stellar objects (MYSOs), whilst megamasers are from AGN sources.

Name of the source	Luminosity ($L_\odot$)	Max vel. spread (km/s)	Classification	References
NGC 4258	80	890	Megamaser	[Greenhill et al., 1996]
NGC 3079	500	126	Megamaser	[Yamauchi et al., 2004]
Circinus	20	260	Megamaser	[Greenhill et al., 2003]
UGC 3789	370	725	Megamaser	[Reid et al., 2009]
NGC 2960 (Mrk 1419)	400	465	Megamaser	[Henkel et al., 2002; Kuo et al., 2011]
IC 2560	122	323	Megamaser	[Ishihara et al., 2001]
NGC 3393	320	601	Megamaser	[Kondratko et al., 2008]
J0437+2456	178	338.85	Megamaser	[Gao et al., 2017]
NGC 6323	500	600	Megamaser	[Kuo et al., 2011; Kuo et al., 2014]
NGC 6926	340	200	Megamaser	[Sato et al., 2005]
UGC 6093	770	801.28	Megamaser	[Zhao et al., 2018]
W1 (NGC 253)	1.02	84.4	Kilomaser	[Gorski et al., 2018]
H_2O-East (NGC 4038/NGC 4039)	1.3	13	Kilomaser	[Brogan et al., 2010]
H_2O-SE (NGC 4038/NGC 4039)	4.1	50	Kilomaser	[Brogan et al., 2010]
H_2O-West (NGC 4038/NGC 4039)	7.7	25	Kilomaser	[Brogan et al., 2010]
G229.5711+00.1525	8.5×10^{-5}	10.25	Stellar maser	[Urquhart et al., 2011]
G220.4587-00.6081	2.29×10^{-6}	5	Stellar maser	[Urquhart et al., 2011]
G083.7071+03.2817	4.79×10^{-7}	7.75	Stellar maser	[Urquhart et al., 2011]
G080.8624+00.3827	2.88×10^{-6}	6.9	Stellar maser	[Urquhart et al., 2011]
G081.8652+00.7800	4.27×10^{-4}	37.5	Stellar maser	[Urquhart et al., 2011]
G081.7131+00.5792	3.55×10^{-6}	11.5	Stellar maser	[Urquhart et al., 2011]
G081.7624+00.5916	6.03×10^{-7}	23.85	Stellar maser	[Urquhart et al., 2011]
G084.1940+01.4388	5.13×10^{-7}	20.6	Stellar maser	[Urquhart et al., 2011]
G084.9505-00.6910	1.55×10^{-6}	2.45	Stellar maser	[Urquhart et al., 2011]
G095.0531+03.9724	1.62×10^{-4}	4.7	Stellar maser	[Urquhart et al., 2011]
G094.2615-00.4116	9.55×10^{-6}	20.6	Stellar maser	[Urquhart et al., 2011]
G094.4637-00.8043	1.26×10^{-5}	2.55	Stellar maser	[Urquhart et al., 2011]
G094.6028-01.7966	2.29×10^{-4}	10.2	Stellar maser	[Urquhart et al., 2011]

3. Method

3.1 Computational hydrodynamics

3.1.1 PLUTO

To simulate the accretion disc of the supermassive star, the finite volume fluid dynamics code PLUTO is used [Mignone et al., 2007]. It has been designed to integrate a system of conservation laws given by:

$$\frac{\partial \mathbf{U}}{\partial t} = - \bigtriangledown \cdot \mathbf{T}\left(\mathbf{U}\right) + \mathbf{S}\left(\mathbf{U}\right) \tag{3.1}$$

where $\mathbf{U}$ represents a set of conservative variables, $\mathbf{T}\left(\mathbf{U}\right)$ describes fluxes of each component of state vector and $\mathbf{S}\left(\mathbf{U}\right)$ represents the source terms.

For the case of ordinary hydrodynamics Equation 3.1 reduces to the following Euler equations:

$$\frac{\partial \rho}{\partial t} + \bigtriangledown \cdot \left(\rho \mathbf{v}\right) = 0 \tag{3.2}$$

$$\frac{\partial \rho \mathbf{v}}{\partial t} + \bigtriangledown \cdot \left(\rho \mathbf{v}\mathbf{v} + p\mathbf{I}\right) = -\rho \bigtriangledown \Phi \tag{3.3}$$

where ρ is the mass density, v is the velocity, p is the thermal pressure and gravitational potential is Φ.

The equation of state provides closure:

$$p = \rho c_s^2, \tag{3.4}$$

where the sound speed is a function of radius c_s(r). Therefore it can be summarised that in the HD module the conservative variables, fluxes and source terms are:

$$\mathbf{U} = \begin{pmatrix} \rho \\ \rho \mathbf{v} \end{pmatrix}, \mathbf{T}\left(\mathbf{U}\right) = \begin{pmatrix} \rho \mathbf{v}^T \\ \rho \mathbf{v}\mathbf{v} + p\mathbf{I} \end{pmatrix}, \mathbf{S}\left(\mathbf{U}\right) = \begin{pmatrix} 0 \\ -\rho \bigtriangledown \Phi \end{pmatrix}. \tag{3.5}$$

The time step Δt is determined by the Courant-Friedrichs-Lewy (CFL) condition. The CFL expression is given by :

$$\Delta t \sim \mathrm{C_a} \frac{\Delta l}{\lambda_{\max}}, \tag{3.6}$$

where $\mathrm{C_a}$, the Courant number, is a limiting factor with the value of less than one, Δl represents the cell length and $\lambda_{\max}$ describes the fastest signal speed. The condition represented by Equation 3.6 is implemented in order to restrict any wave from crossing a distance larger than a fraction of a grid cell [Mignone et al., 2012], this is required for numerical stability.

3.1.2 Numerical scaling

I have run PLUTO on the University of Hertfordshire high performance computing cluster (UHHPC). To test the performance of the code, I have run the multiple parabolic stellar flybys problem (see below for details of the setup) for two different resolutions, 50x100 and 100x100, for CPUs number between 4 to 128. I have run the code for 100 timesteps only, to analyse what set up is the most efficient. From Figure 3.1 it can be seen that doubling the CPU number does not exactly double the speed of the simulation. The more processors are used, the more time it takes to communicate between each of the CPUs in parallel mode. As expected, doubling the resolution in radial direction does increase the computational time accordingly. Overall, the scaling is very reasonable, up to the highest number of cores tested, and therefore, I have used 64 cores for most of my runs.

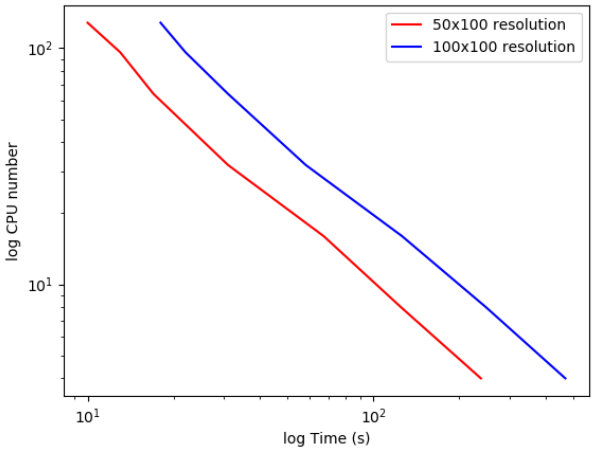

Figure 3.1: Numerical scaling for different number of CPUs.

3.2 Setups

3.2.1 Standard Disk-Planet problem

I use the two dimensional Disc-Planet test problem, available as part of PLUTO, to act as the start point for the modelling of accretion disc around the SMS. The

problem simulates the interaction of the planet of a mass comparable to Jupiter's mass, $m_p = 320\ M_\oplus$ embedded in a viscous disc centered on a star, with the masses of $M_{disc} = 0.01\ M_\odot$ and $M_\star = 1\ M_\odot$ respectively. The M_{disc} is contained between the $r_{min} = 0.4$ to $r_{max} = 2.5$ in unit of $r_0 = a_{Jup} = 5.2$ au. The ratio of the disc's vertical height H to the radius $R = r \sin\theta$ is set as $H = 0.05\ R$. The simulation is calculated with the isothermal equation of state. The initial density is represented by:

$$\rho(r,\theta) = \frac{1}{R\sqrt{R}} \exp\left\{-0.5\left[\left(\frac{\pi}{2} - \theta\right)\frac{r}{H}\right]^2\right\} \tag{3.7}$$

The calculations are performed in the observer's frame of reference using a second-order unsplit Runge-Kutta method with a CFL number of 0.4 [Mignone et al., 2012].

The planet is characterised by additional term in the total gravitational potential that acts on the disc, adapted from Klahr and Kley [2006]:

$$\Phi = \Phi_\star + \Phi_p = -\frac{GM_\star}{r} + \Phi_p, \tag{3.8}$$

where the cubic planetary potential Φ_p is defined as:

$$\Phi_p = \begin{cases} -\frac{m_p G}{d}\left[\left(\frac{d}{r_{sm}}\right)^4 - 2\left(\frac{d}{r_{sm}}\right)^3 + 2\frac{d}{r_{sm}}\right] & \text{for } d \leqslant r_{sm} \\ -\frac{m_p G}{d} & \text{for } d > r_{sm}, \end{cases} \tag{3.9}$$

with $r_{sm} = 0.6\ H$. The top term in the above equation has an additional term in the square brackets. The term artificially reduces the strength of the potential below r_{sm}, because the true potential diverges and it would produce very high acceleration. Since the resolution is limited and the region is unresolved, the value of the acceleration would be wrong. The application of the above term allows for the correct calculation of the accelerations on the scales that can be resolved, minimising the errors.

The next simulation set up is modified in order for the static potential to be adapted to a moving one, where the planet has traced orbits from its initial position at disc radius = 1.5 to disc radius of 0.5 units. This worked well, and a plot of the results is shown in Figure 4.1.

3.2.2 Parabolic stellar flyby

To simulate parabolic stellar flybys around a supermassive star first I recreate a problem from Cuello et al. [2018]. In the mention paper, they use 3D smoothed particle hydrodynamical simulations to model a parabolic flyby by a stellar perturber around the protoplanetary disc with varying values of periastron distance, inclination angle and stellar mass ratios.

According to Clarke and Pringle [1993] the most destructive encounter, where the disc looses around 50% of its mass (if the ratio of the outer edge of the disc and the periastron distance is 0.8) is prograde and coplanar, whilst the retrograde and coplanar one has almost no impact on the disc. In the scenario, where orbital and

disc planes are close to orthogonal, the perturber plunges through the disc without having any previous interaction with it, therefore the disc particles located within periastron remain bound and sustain their alignment. While the rest of the material is transferred out on to orbits inclined to the original orbital plane. Therefore I will only consider the case where the encounter affects the disk in the most destructive manner, namely prograde and coplanar (inclination of the orbit of 0° angle) for both stellar masses being 1 $M_\odot$, in spherical coordinates using the grid code PLUTO. The code is set up to work with non-dimensional units and hence the dimensionalisation to c.g.s. units is essential for both the test problem as well as the further modelling.

3.2.2.1 Circumprimary disc

The inner and outer radius of the 0.01 $M_\odot$ circumprimary disc is given as R_{in} = 10 au and R_{out} = 150 au, assuming a power law surface density at the start of the calculation:

$$\Sigma = \Sigma_0 \left(\frac{R}{R_{in}}\right)^{-1} \tag{3.10}$$

$$\Sigma_0 = \frac{M_{disk}}{2\pi \times R_{in} \times (R_{out} - R_{in})} \tag{3.11}$$

and ratio between height and radius is $H/R = 0.05$ at $R = R_{in}$ and $H/R = 0.1$ at $R = R_{out}$. Therefore the expression for the height varies with radius as:

$$H = 0.05 \times R_{in} \times \left(\frac{R}{R_{in}}\right)^{1.25}. \tag{3.12}$$

The equation for the density of the circumprimary disk is:

$$\rho = \frac{\Sigma}{2H} \tag{3.13}$$

and substituting Eqn. 3.10, I get:

$$\rho = \frac{\Sigma_0 \times R_{in}}{2R \times H} \tag{3.14}$$

with the density outside the disk is set to 10^{-20} g cm^{-3}. The local isothermal equation of state is used, where the temperature is given as a function of radius from the primary star $T(r) = 64\ \mathrm{K}(r/r_{in})^{-1/2}$. Therefore the relevant code file for equation of state is modified to allow it to change with radius.

The angular velocity is calculated from the below equation of radial hydrostatic equilibrium equation, which is preserved by the balance of gravitational acceleration with centrifugal acceleration and the pressure gradient:

$$\frac{1}{\rho}\frac{\partial p}{\partial R} = \Omega^2 R - \frac{GM_\star}{R^2}, \tag{3.15}$$

where G is gravitational constant, pressure is $p = \frac{\rho \times k_B \times T}{\mu m_p}$, with a Boltzmann constant k_B, mean molecular weight $\mu = 2.35$, m_p as a mass of a proton and T, temperature expression mentioned above. Therefore the angular velocity for the circumprimary disk is:

$$\Omega^2 = \frac{GM_\star}{R^3} - 0.5 \times \frac{k_B \times 64\mathrm{K}}{R \times \mu m_p} \times \left(\frac{R}{R_{in}}\right)^{-0.5} \tag{3.16}$$

3.2.2.2 Perturber

The initial position of the 1 $M_\odot$ perturber is 10 times the value of the circumprimary disk's outer radius, R_{out}. As mentioned in Cuello et al. [2018], by setting this initial value in the negative y-direction it removes any artificial effects caused by a sudden introduction of the perturber close to the disc. The perturber is entered in the negative y and x direction, and leaves the grid towards negative y-direction but positive x-direction, allowing for the prograde encounter. The initial y and x values of the perturber are calculated as follows:

$$y_i = -10 \times R_{out} \tag{3.17}$$

$$x_i = -2R_{peri} \times \sqrt{1 - \frac{y_i}{R_{peri}}} \tag{3.18}$$

In order for the perturber to follow parabolic orbit Cuello et al. [2018] use Barker's equation:

$$\Delta t = \sqrt{\frac{2R_{peri}{}^3}{GM_t}} \left(D_f + \frac{1}{3} D_f^3 - D_i - \frac{1}{3} D_i^3 \right) \tag{3.19}$$

where M_t is the sum of the mass of the central star, $M_\star$ and the mass of the perturber, M_{pert}. Subscripts 'i' and 'f' indicate initial and final position of the perturber.

$$D_{i,f} = \tan\left(\frac{\nu_{i,f}}{2}\right) \tag{3.20}$$

and true anomaly is:

$$\nu_{i,f} = \arctan\left(\frac{x_{i,f}}{y_{i,f}}\right). \tag{3.21}$$

I use the equations 3.19, 3.20 and 3.21 to calculate the time it takes for the perturber to arrive at the periastron distance, t_0. Since the perturber is defined as gravitational potential, which is determined from its position at each timestep, Barker's equation is inverted, so the position of perturber is calculated as a function of time. According to Meire [1985] the most practical solution to the Barker's equation follows the below calculations:

$$A = \frac{3}{2} \sqrt{\frac{2GM_\star}{2R_{peri}{}^3}} \times (t - t_0) \tag{3.22}$$

$$B = \left(A + \sqrt{A^2 + 1} \right)^{\frac{1}{3}}. \tag{3.23}$$

Hence the true anomaly of the perturber's orbit is:

$$\nu = 2 \arctan\left(B - \frac{1}{B} \right) \tag{3.24}$$

and its radius is determined as follows:

$$Radius = \frac{2R_{peri}}{1 + \cos\nu} \tag{3.25}$$

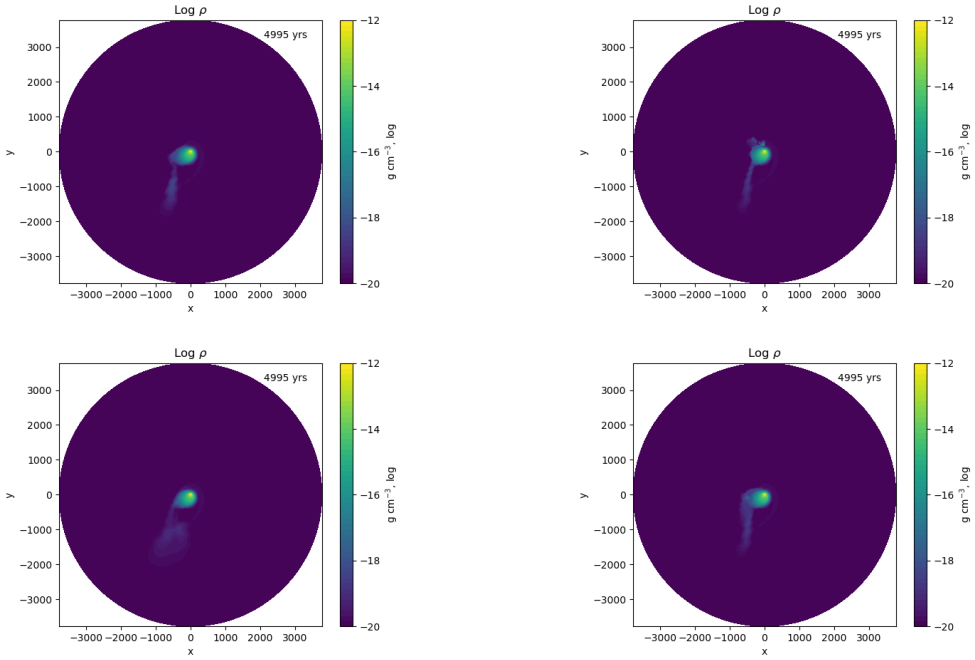

Figure 3.2: Face-on view of the perturber being close to periastron distance, R_{peri} = 200 au with varying r_{sm} values. The upper panel shows plots of simulation, where Eqn. 3.9 has been used, and the bottom with Eqn. 3.26. The plots in the left column, represents r_{sm} with 3 times the value of the length of a grid cell, and in the right column, r_{sm} = length of one grid cell.

For the later computations with a number of perturbers and a range of periastron radii, I define direct stellar collision of the perturber with the central star when the periastron distances, $R_{peri} \leq 10$au. In this instance the position of perturber, xp and yp, as well as its *Radius* are set to 0. The mass of the perturber, M_{pert} is then added to the mass of the central star, $M_\star$.

The central star as well as perturber are characterised by the gravitational potential using Eqn. 3.8 and Eqn. 3.9, where Φ_p in this case represents gravitational potential of the perturber instead of planet as in the previous standard problem. I have tested both the first expression from Eqn. 3.9 when $d < r_{sm}$, smoothing factor as well as the below expression in order to find the optimum value for r_{sm}:

$$\Phi_p = -\frac{GM_{pert}}{r_{sm}}. \tag{3.26}$$

The usual rule is to have r_{sm} set to 3 times the value of the grid cell. I have tested this condition for both expressions, mentioned above, as well as r_{sm} set to a minimum one grid cell. The results are seen in Figure 3.2, where it can be concluded that the r_{sm} set to the value of one grid cell length and using Eqn. 3.9 shows finer details in the plot (see upper right image in Fig. 3.2). Hence, use this equation for the simulations of single and multiple parabolic stellar flyby.

3.2.2.3 Computational set-up

The HD equations are solved in a two dimensions in spherical coordinates, since I am only computing prograde orbit with 0° orbital inclination. The coordinates used are

therefore the radial and azimuthal directions. The spatial integration is performed using piecewise, total variation diminishing, linear reconstruction of the fluxes to the cell boundaries and time evolution is computed using second order Runge-Kutta schemes. The Harten-Lax-van Leer-Contact discontinuity (HLLC) Riemann solver is used to solve the numerical fluxes. The computational grid is defined from 10 au to 4000 au using logarithmic scale for radial grid, therefore the mesh size is increasing with coordinate and both radial boundary conditions are set to reflective. The azimuthal, uniform grid is set from 0 to 2π with periodic boundary. I use a resolution of 100x100 grid elements for radial and azimuthal direction respectively with the $r_{\rm sm}$ = 0.06 $\times Radius$. I run the simulation with different periastron distances as seen in Table 3.1. The CFL number is equal 0.3 except when periastron distance is 1 au and 10 au then the CFL number is set to 0.2. That allows for the time steps to have a lower value and therefore eliminates the chance for the simulation to crash due to the low values of density.

Table 3.1: Set of flyby simulations with various periastron distances, and respective initial position of the perturber and the time for the perturber to arrive at $\rm R_{peri}$.

$\rm R_{peri}$ (au)	$\rm x_i$ (au)	$\rm y_i$ (au)	$\rm t_0$ (yrs)
1	-77	-1500	3096
10	-246	-1500	3180
100	-800	-1500	4039
200	-1167	-1500	5040
300	-1470	-1500	6088

3.2.3 Simulation of accretion disk around SMSs

3.2.3.1 Parameters of the accretion disk

Massive young stars are deeply embedded in their parental clump, hence it is difficult to resolve their accretion disk from the encompassing envelope, even in subarcsecond resolutions [Cesaroni et al., 2006]. One method to detect and estimate the radius of an accretion disk is using maser lines.

I assume that W1 kilomaser detected by Gorski et al. [2018] is associated with a forming cluster with supermassive star in the center. In order to estimate the size of the accretion disk around a supermassive star I first take the value of the velocity spread of the "low-velocity" features from the kilomaser (see left Fig. 2.4), $\Delta\nu = 8.75$ km $\rm s^{-1}$, and I assume it corresponds to the radius of the disk. Using the equation below:

$$R_{\rm out} = \frac{\rm GM_\star}{(\Delta\nu)^2} \tag{3.27}$$

the 1000 $\rm M_\odot$ star would have $R_{\rm out} \sim$ 11589 au ($\sim$ 0.056 pc). Comparing this value to the value of half-mass radius of the forming cluster in Fig. 2.2 at time 2.2 Myr, which corresponds to the value of SMS' mass used in the calculation, the $\rm R_h$ ranges between $\sim$ 0.1-0.3 pc. As the mass increases, the half-mass radius is decreasing until the first supernovae. Thus the value of $R_{\rm out}$, estimated above is not feasible as it

would result in a outer radius, $R_{\rm out}$ of an accretion disk being equal to around half of the $R_{\rm h}$ of the cluster.

As discussed previously, there seems to be a continuity in maser properties from stellar masers to AGN (see Fig. 2.6) and therefore I apply the physics learnt from AGN to kilomasers. Looking at Figure 2.5, "high-velocity" features can be used to calculate the radius of the disk, as they represent emission closer to the outer edges of the disk in AGNs. Hence assuming this also applies to the disk around a supermassive star and the kilomaser it produces, I take the velocity spread out to both "high-velocity" features in the W1 kilomaser to be $\Delta\nu = 83$ km s^{-1}. I assume that all the high-velocity maser spots are on the circular Keplerian orbits and are located on the midline of the disk [Pesce et al., 2015]. Using Equation 3.27 and keeping the rest of the values the same as in previous calculations, I get $R_{\rm out} \sim 129$ au ($\sim 6.2{\times}10^{-4}$ pc). This value is only 29 au higher than the $R_{\rm out}$ value used in the standard Disk-Planet problem and the parabolic stellar flybys for the 1 $M_\odot$ star. The high-velocity maser spots in W1 kilomaser might be located in the closest area to the inner disk that can mase the water line and not necessary in the vicinity of the outer edges of the disk. Thus it is important to look into the literature for possible values of the outer radius of an accretion disks around massive stars.

Cesaroni et al. [2006] presented a list of candidate disks in high mass (proto)stars, although they do warn that some of the values are uncertain. One of the candidate listed, IRAS 20126+4104, is the best-studied case of a Keplerian accretion disk around high mass star. The disk's mass is about 4 $M_\odot$ with a radius of 1600 au around a massive (7 $M_\odot$) YSO [Cesaroni, 2005]. The most common value of radius of the disk is 500 au and some values are as high as 20,000 au. Although the authors argue that those high values of radius would suggest it to be a massive rotating structure called "toroid", rather than an accretion disk around a single star. "Toroids" are believed to host a stellar cluster and might not be in equilibrium, whilst accretion disks are in Keplerian orbits around their central stars [Cesaroni et al., 2006].

Taking all the above arguments into consideration I simulate accretion disks with outer radius of $R_{\rm out} = 500$ au, as it is the most common value in Cesaroni et al. [2006]. I also simulate disks with $R_{\rm out} = 1000$ au, which is the safest guess for an upper limit, since the accretion disk needs to be in equilibrium between gravity and rotation. Of course, the situation might be different in the case of SMS.

The next uncertain value is the mass of the accretion disk. Looking at the above mentioned list of candidate disk in high mass (proto)stars in Cesaroni et al. [2006] I can deduce that this quantity varies largely and does not scale with the radius of the disk or the mass of the central star. Thus I assume the mass of the disk, $M_{\rm disk}$, is 1% of the mass of the central star, $M_\star$, as it was assumed in the case of parabolic stellar flyby in Cuello et al. [2018]. For comparison I also include an upper limit of the $M_{\rm disk} = 10\% \times M_\star$.

The equation of state and angular velocity expressions (eq. 3.16) are adapted to include temperature, T, that correlates to the supermassive star. $T_{\rm eff}$ is estimated to be around 10^4 K at the surface of the supermassive star with the mass $< 10^4$

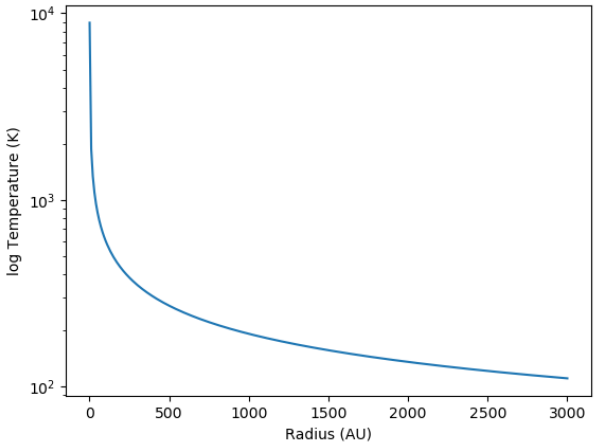

Figure 3.3: Temperature versus radius plot for a supermassive star. The surface temperature is equivalent to $T_{\rm eff}$ of the star, and around 100 au radius the temperature reaches around 10^3 K.

$M_\odot$ [Gieles et al., 2018]. Figure 3.3 shows a temperature versus radius plot, using equation:

$$T = 64 \times 30 \times \left(\frac{R}{R_{\rm in}}\right)^{-1/2}. \tag{3.28}$$

I have adjusted the temperature equation from the previous case of parabolic stellar flyby from Cuello et al. [2018] and multiplied the expression by 30. This number allowed the surface temperature to be equalled to $T_{\rm eff}$ of the SMS, and the temperature around 100 au radius is higher than 300 K, hence allows for the water lines to to be mased.

3.2.3.2 Stellar flybys

As in the previous simulations of a single parabolic stellar flyby, I am only considering encounters that are prograde, as they are the most destructive ones for the accretion disk.

The mass of the perturbers is estimated based on the top plots in Figure 2.2. I take the "metal-poor" plot with the number of stars $N = 10^7$. At the time when log $m_{\rm sms}$ is equal 10^3 $M_\odot$, the total mass of all the stars in the cluster is $10^{6.2}$ $M_\odot$. Thus the average mass of the pertuber is $M_{\rm pert} \sim 0.2$ $M_\odot$.

The number of collisions and their frequency can be also estimated from Figure 2.2, but since mass of the stellar wind also needs to be taken into consideration it would be much harder to calculate those values. Because the order of magnitude for number of collision is sufficient I can use the plot in Figure 3.4 to calculate this value. Following the red line in the plot, I take the initial mass in stars $M_0 = 10^6$ $M_\odot$, the cluster half-mass radius of $R_{\rm h0} \simeq 2.3$ pc and the initial mass of each star, $m_0 \simeq 0.1$ $M_\odot$. The accretion factor, a, for the mass in the cluster i.e. current mass of the stars (when $M_{\rm SMS} = 1000$ $M_\odot$) divided by the initial mass of the stars, is ~ 3. The

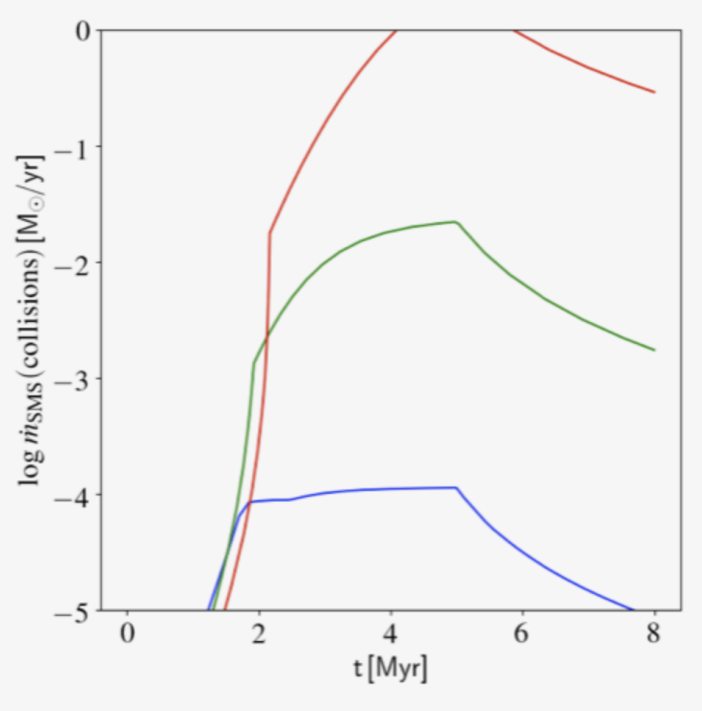

Figure 3.4: Collision rates for a supermassive star. The plot is for model with $\delta = 1$, $\eta = 0.75$ and the number of stars in "metal-poor" cluster is indicated as $N = 10^7$ (red), 10^6 (green), 10^5 (blue) (Gieles, private communication).

value higher than that would corresponds to two-body relaxation becoming more important [Gieles et al., 2018]. Therefore the total mass of the stars in the cluster is:

$$\mathrm{M} = \mathrm{a} * \mathrm{M}_0, \tag{3.29}$$

which gives the value of $3{\times}10^6$ $M_\odot$. The radius, in which the mass of the stars is contained is $r_0 = a^{-3} * R_{h0} = 0.085$ pc (17500 au). The region of interest, r_i, is set to 1000 au, as this is the highest value of the accretion disk's radius I am simulating. The density of stars:

$$\mathrm{n} = \frac{3\mathrm{M}}{4\pi {\mathrm{r}_0}^3 \mathrm{a} \mathrm{m}_0}, \tag{3.30}$$

gives 4.45 $\times 10^{-7}$ stars per (au)^3. Hence the number of stars in the region of interest, r_i:

$$\mathrm{N} = \mathrm{n} \times \frac{4\pi {\mathrm{r}_\mathrm{i}}^3}{3}, \tag{3.31}$$

is N = 1864. The crossing times is defined as $t_{cross} = 2\ r_i/V_{rms}$, where V_{rms}, is the one-dimensional velocity dispersion of the cluster:

$$\mathrm{V}_{\mathrm{rms}} \simeq \sqrt{\frac{\mathrm{GM}}{6\mathrm{R}_{\mathrm{ho}}}}, \tag{3.32}$$

and it gives a value of 159 km/s. Therefore crossing time is, $t_{cross} = 60$ years. Applying the values calculated above, the flyby rate = $N/t_{cross} \simeq 30$ per year. Since I am only interested in the collision that occurs in the plane of the disk, 10% of the

solid angle and only in the prograde ones, therefore the flyby rate is around 1 per year to the order of the magnitude.

Mark Gieles has kindly provided more detailed mass over time plots to estimate the collision rate. If I take the value for log $\dot{m}_{\rm SMS}$ from the Figure 3.4 for red line at 2 Myr and 4 Myr, then within that $\Delta t = 2$ Myr time frame I get accretion rate of $\dot{m}_{\rm SMS}$= 0.005 $M_\odot$ per year. Dividing this value by $M_{\rm pert} = 0.2$ $M_\odot$ I arrive at the collision rate of 0.025 per year, and for the ones that occur in the plane of the disk is equal to 0.0025 flybys per year, therefore around 1 per 400 years. This is certainly a lower limit, as it only takes into account the actual hits, not the near misses that can still impact the accretion disc significantly. Because both of the estimations are either on the high or low side, I simulate both flyby rates as well as the rate of 1 per 10 years for comparison.

In order to include multiple collisions the previous code for single stellar flyby is adapted. A while loop is implemented to iterate over the number of perturbers. Flyby rate as well as the time of the simulation allows for the number of perturbers to be calculated i.e. for 5000 years simulation and flyby rate of 1 per year, I include 5000 perturbers. Periastron distance values are generated using random numbers up to the maximum value of periastron distance set. The start time of the perturbers is also calculated using random numbers for the values set between the start time, when I want the first perturber to enter the grid and finish time, when the last perturber enters the grid. That ensures the the perturbers are spread out in time according to the chosen flyby rate. To ensure perturbers are coming from different angles, without changing the starting values of y_i and x_i, I introduce rotation matrix:

$$R = \begin{bmatrix} \mathrm{xp}\,\cos\theta - \mathrm{yp}\,\sin\theta \\ \mathrm{xp}\,\sin\theta + \mathrm{yp}\,\cos\theta \end{bmatrix}, \tag{3.33}$$

where θ is the orbital angle and its values are generate using random numbers between 0 and 2π.

I simulate only prograde encounters, hence only half of the encounters calculated above, as they are more destructive than the retrograde ones. However, since it is only a factor of 2, this will not affect the chosen flyby rates.

3.2.3.3 Computational set-up

I perform set of simulations, varying different parameters outlined in Table 3.2. First, I have run a set of simulations without any stellar perturbers for 30,000 years, to test if the accretion disk is in equilibrium. Figure 3.5 and Figure 3.6 shows the disk is oscillating with various amplitudes and frequencies depending on the parameters of each disk set up. For SMS with the mass of 1000 $M_\odot$ and outer radius of 500 au, the oscillations' frequency is decreasing after around 25 kyr. For the disk with the larger radius of 1000 au, the oscillations are regular throughout the whole computational time. For the case of 10,000 $M_\odot$ SMS (see Fig. 3.6) the amplitude of the oscillations decreases significantly after the initial 5000 years. Disks with the radius of 500 au continue to have oscillations with regular frequency, whilst the larger disks of 1000 au radius oscillates with smaller frequency compared to the disk with 500 au radius. Therefore I run the simulations without a stellar perturber for the first 5000 years,

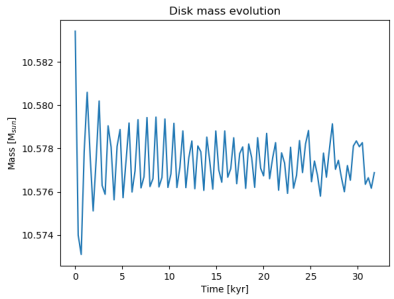

(a) $M_{disk} = 10\ M_\odot$, $R_{out} = 500$ au

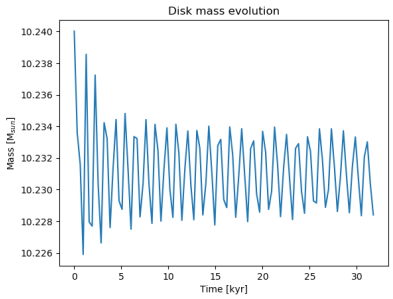

(b) $M_{disk} = 10\ M_\odot$, $R_{out} = 1000$ au

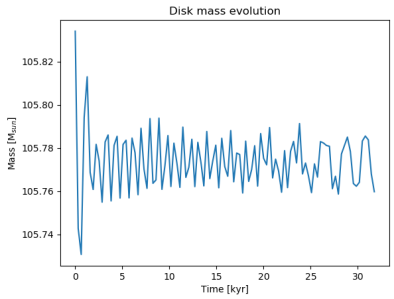

(c) $M_{disk} = 100\ M_\odot$, $R_{out} = 500$ au

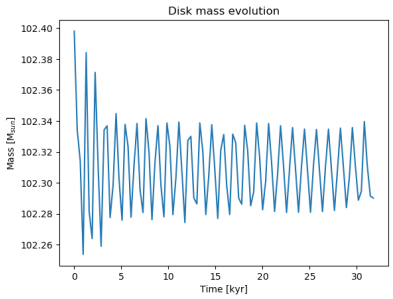

(d) $M_{disk} = 100\ M_\odot$, $R_{out} = 1000$ au

Figure 3.5: Disk mass evolution for 1000 $M_\odot$ supermassive star. The top and bottoms plots are for disks of 10 $M_\odot$ and 100 $M_\odot$ mass, respectively. Right plots show time evolution of the disk mass with outer radius of 1000 au, whilst the left column represents disks with $R_{out} = 500$ au.

that will allow the disk to settle from the initial high-amplitude oscillations. The smaller oscillations are ignored since the high number of stellar flyby and collisions will have a more substantial impact on the disk than the oscillations itself.

In order for the simulation to run faster, I use the resolution of 50x100 grid elements for radial and azimuthal direction respectively. The simulation time is set to 10,000 years for the disk's radius of 500 au and 15,000 years for the 1000 au radius ones; the stellar perturbers are entered after 5,000 years. Some of the set ups have been run for twice as long, to allow the disk to fully react to the flybys and collisions. The radial grid is defined from 10 au to 5000 au for $R_{out} = 500$ au and from 10 au to 10,000 au for $R_{out} = 1000$ au using logarithmic scale. The rest of the set up is the same as in the case of the single stellar parabolic flyby, described in section 3.2.2.3

3.3 Derivation of maser spectrum

I derive the model maser spectra using a python code, initially provided by my supervisor and modified by me (see Appendix A.1), and plot it together with the W1 kilomaser from Gorski et al. [2018], kindly provided in electronic form by Mark Gorski, for direct comparison. The model of maser spectrum is plotted with flux against velocity along the line of sight, where velocity ranges up to 250 km/s to match the W1 kilomaser velocity spread. For the case of SMS with mass of $10^4\ M_\odot$ I had to increase the range of velocity spread to 800 km/s in order to see "high-velocity" features. The systemic velocity of NGC 253, estimated from left spectrum in Figure

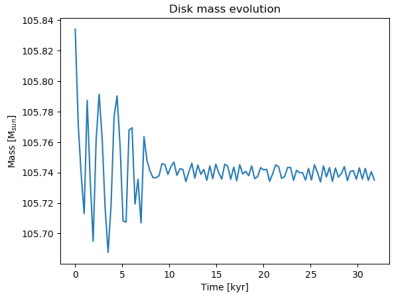

(a) M_{disk} = 100 $M_{\odot}$, R_{out} = 500 au

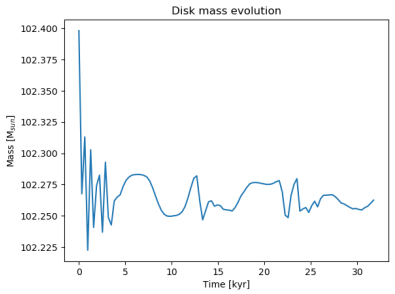

(b) M_{disk} = 100 $M_{\odot}$, R_{out} = 1000 au

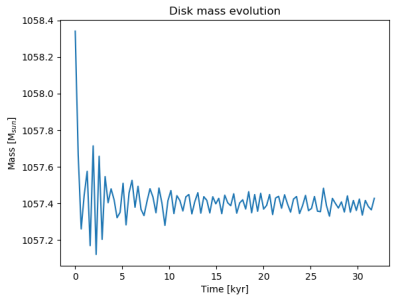

(c) M_{disk} = 1000 $M_{\odot}$, R_{out} = 500 au

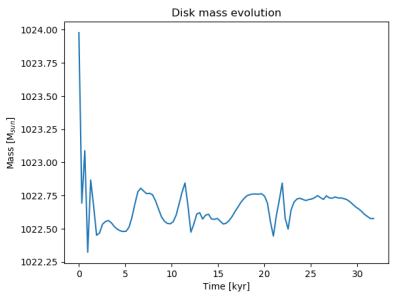

(d) M_{disk} = 1000 $M_{\odot}$, R_{out} = 1000 au

Figure 3.6: Disk mass evolution for 10000 $M_{\odot}$ supermassive star. The top and bottom plots are for disks of 100 $M_{\odot}$ and 1000 $M_{\odot}$ mass, respectively. Right column show time evolution of the disk mass with outer radius of 1000 au, whilst the left column represents disks with R_{out} = 500 au.

2.4, is 115 km s^{-1} and is applied to maser models. For the integration along the line of sight, we map the simulation output on to a Cartesian grid and assume the source to be observed edge-on. Fluxes are calculated using Equation 2.13, where I assume the effective aspect ratio, defined in Equation 2.11 is 10, hence a_{10}=1. That results in Equation 2.13, reducing to:

$$F = 4.7 \times 10^{17} \left(\frac{dy}{\mathrm{D}}\right)^2 \mathrm{Jy}, \tag{3.34}$$

where dy is defined as the length of the Cartesian grid cell in y-direction and D = 3.5 Mpc, the distance to the starburst galaxy NGC 253. The 22 GHz H_2O line requires dense gas of at least 10^7 cm^{-3} and temperatures larger than 300 K [Gorski et al., 2018], hence the densities are limited between the range of 10^7 - 10^{16} cm^{-3} × m_p (mass of the hydrogen). The upper level is estimated based on the density in the outer edges of the accretion disk. The temperature defined by Equation 3.28 is also restricted between the already mentioned minimum of 300 K up to 1500 K, as to allow the gas to remain molecular [Kartje et al., 1999]. Those parameters are required for the water to be mased if it is collisionally pumped.

Table 3.2: Set of simulations of accretion disk around the supermassive star, varying its mass, mass and outer radius of the accretion disk, periastron distance and flyby rate.

$M_\star$ ($M_\odot$)	R_{out} (au)	M_{disk} ($M_\odot$)	R_{peri} (au)	flyby rate
1000	500	10	550	1 per year
1000	500	10	550	1 per 10 years
1000	500	10	550	1 per 100 years
1000	500	10	1000	1 per year
1000	500	10	1000	1 per 10 years
1000	500	10	1000	1 per 100 years
1000	500	100	550	1 per year
1000	500	100	550	1 per 10 years
1000	500	100	550	1 per 100 years
1000	500	100	1000	1 per year
1000	500	100	1000	1 per 10 years
1000	500	100	1000	1 per 100 years
1000	1000	10	1100	1 per year
1000	1000	10	1100	1 per 10 years
1000	1000	10	1100	1 per 100 years
1000	1000	100	1100	1 per year
1000	1000	100	1100	1 per 10 years
1000	1000	100	1100	1 per 100 years
10000	500	100	550	1 per year
10000	500	100	550	1 per 10 years
10000	500	100	550	1 per 100 years
10000	500	100	1000	1 per year
10000	500	100	1000	1 per 10 years
10000	500	100	1000	1 per 100 years
10000	500	1000	550	1 per year
10000	500	1000	550	1 per 10 years
10000	500	1000	550	1 per 100 years
10000	500	1000	1000	1 per year
10000	500	1000	1000	1 per 10 years
10000	500	1000	1000	1 per 100 years
10000	1000	100	1100	1 per year
10000	1000	100	1100	1 per 10 years
10000	1000	100	1100	1 per 100 years
10000	1000	1000	1100	1 per year
10000	1000	1000	1100	1 per 10 years
10000	1000	1000	1100	1 per 100 years

4. Results

4.1 Disk-Planet problem

The simulation was run with the original set up and it can be noticed from the left image in Figure 4.1 that the presence of the large planet leads to the formation of the spiral arms. There is an increase in density behind the planet on the inner side and a decrease in density on the outer side in front of the planet. Subsequently the static potential was adapted to a moving one where the planet has traced orbits from its initial position at disc radius = 1.5 to disc radius of 0.5 (see right image in Fig. 4.1). The well-defined spiral arms visible in the previous static potential image are not that clearly defined and the density perturbations are spread out in more chaotic manner.

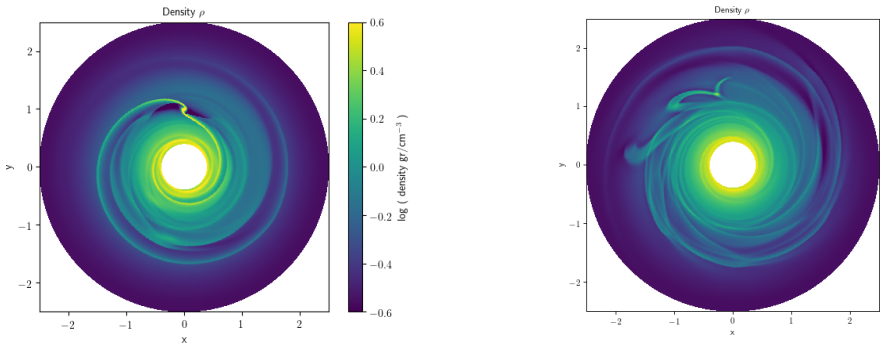

Figure 4.1: Evolution of the surface density perturbation for static potential (left image) and the moving potential (right image). The color bar for the plots was truncated from -0.6 to 0.6 to enhance contrast. 1 unit in the horizontal and vertical axis represents 5.2 au.

4.2 Parabolic stellar flyby

Figure 4.2 shows the density of the gas with three evolutionary stages during the flyby. Each row represents a different periastron distance of 100 au, 200 au and

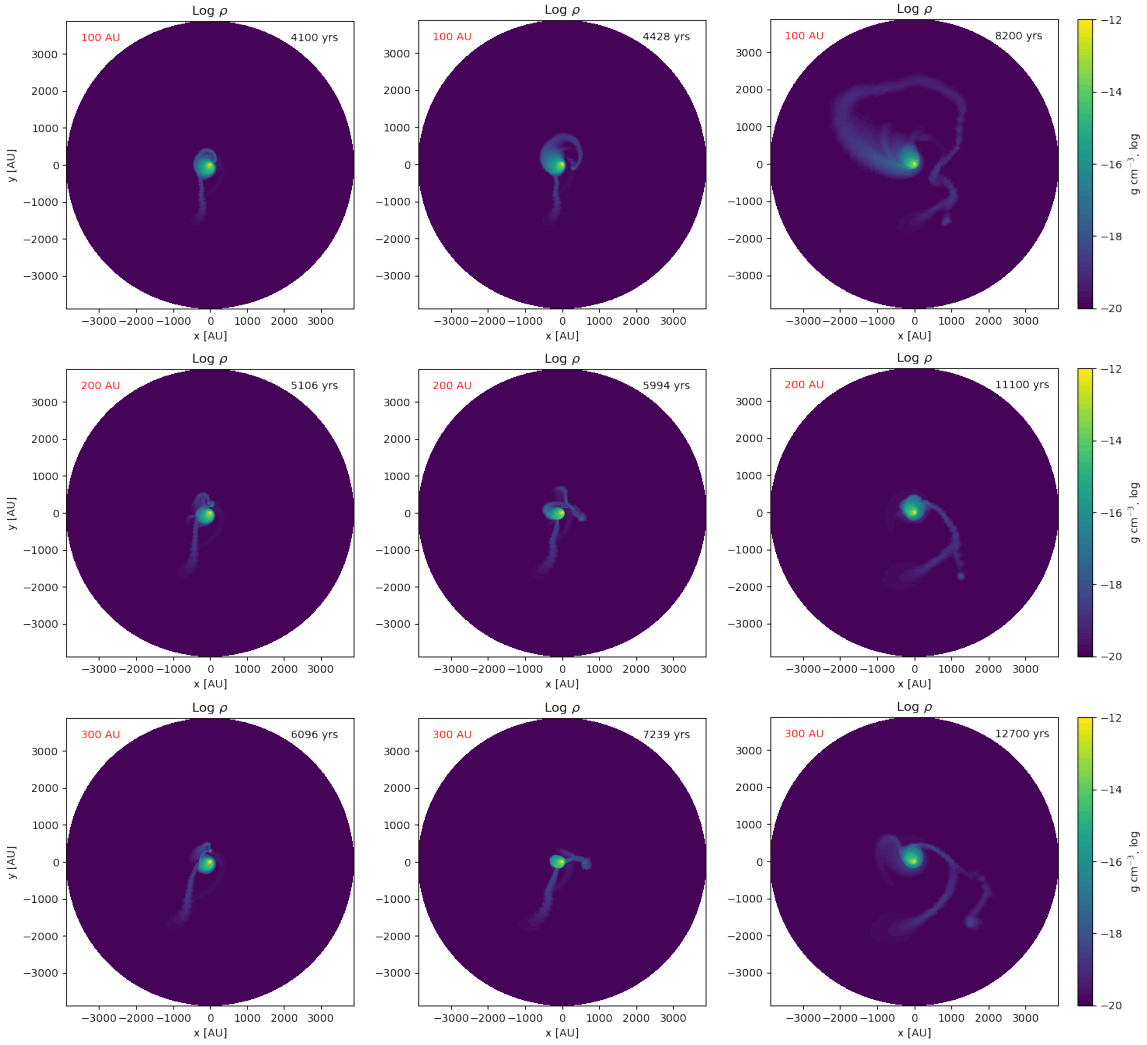

Figure 4.2: Density plots of parabolic stellar flybys for periastron distances: 100 au, 200 au and 300 au. The disc rotation is clockwise. The plots shows different stages of encounters. Starting from the left, the stellar perturber is at the periastron distance, moving towards the other side of the grid and almost leaving the computational grid.

300 au, respectively. The left column represents stellar perturber at the periastron distance, followed by the perturber leaving the proximity of the circumprimary disk, and the right column displays perturber on its way to leave the computational grid.

The results are consistent with the outcome from the simulations performed by Cuello et al. [2018] (presented in Figure 2 in their paper). At the periastron distance the stellar perturber does strip substantial amount of the gas from the circumprimary disk, which is in agreement with the findings of Clarke and Pringle [1993]. There is a visible evolution of two-armed spiral, with one of the arms somewhat stronger than the other one for some R_{peri} values. Comparing different periastron distances, I can notice that the lower the value of R_{peri}, the more destructive the outcome is for the disk, and the stronger spiral arms are during the flyby itself.

At the periastron distance, shown in the left column in Fig. 4.2, both stars connect via a sharp spiral, whilst the disk develops asymmetrical shape. The middle column shows a timestep, when the stellar perturber is still close to the disk, and its shape

can already be distinguished from the disk. Once the perturber is on its way to leave the computational grid (right column) the accretion disk develops longer spiral arms and since the simulation was run without dissipation within the disc, it can also be noticed that the disc is perturbed into eccentric orbit, also consistent with the results in Clarke and Pringle [1993].

Direct stellar collisions, which are defined here as any parabolic stellar flyby with $R_{peri} \leq 10$ au, are visualised in Figure 4.3. In terms of time evolution it is similar to the flybys, described above, with the difference that the perturber does not leave the circumprimary disk, but it is merged with the central star. It can be noticed straight away that for the R_{peri} of 1 au and 10 au, the outcomes after the merger are the same, since the code has been set up to automatically merge two stars once the radius of the perturber is equal or lower to 10 au. The left column shows the perturber approaching periastron distance, and as expected the disc develops a "bulge" with direction towards the perturber, as the mass of the gas is attracted gravitationally toward the mass of the perturber. The middle column shows density of the gas couple hundreds years after the direct collision. The disc's mass is more concentrated in the centre and more spread out in the outer parts with two spiral arms present, again one is much larger and stronger than the other one. The density of the gas is significantly lower than before the collision. Afterwards (the right column) the accretion disc is restoring its original shape with one of the spiral arms spread out to a larger radius.

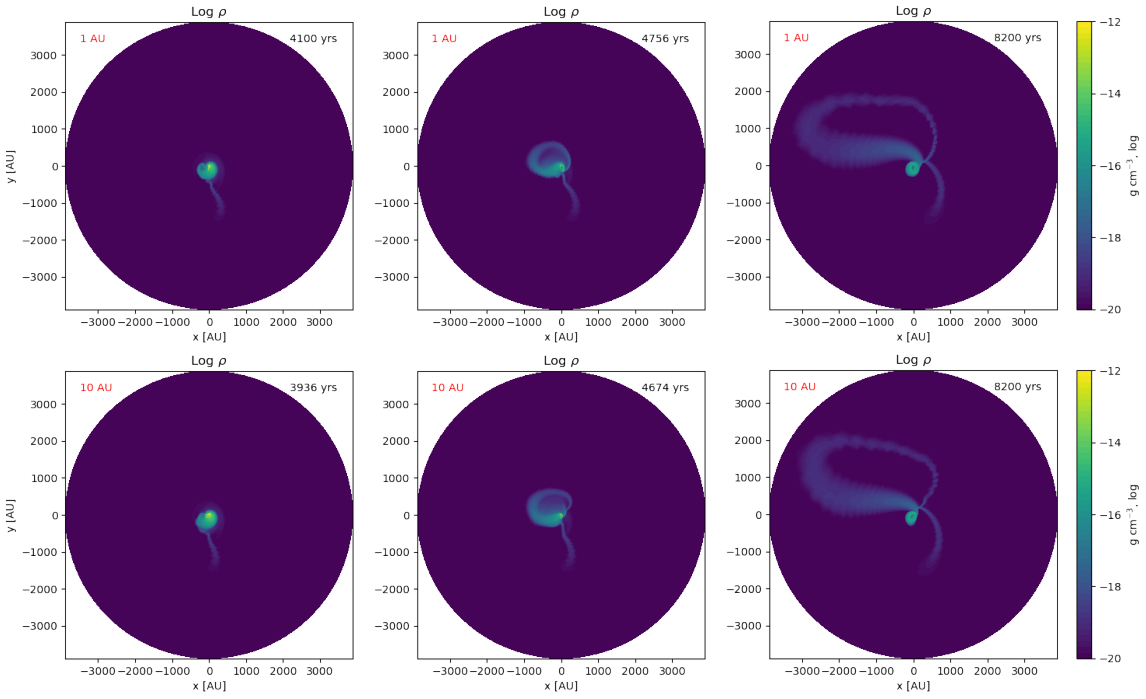

Figure 4.3: Density plots of direct stellar collisions for periastron distances: 1 au and 10 au. The disc rotation is clockwise. The plots shows the time evolution of direct collisions, with the left image representing stellar perturber at the periastron distance.

4.3 Multiple flybys around SMS

In this section, I present results for each simulation set up. Some of the results, especially with same parameters but varying maximum periastron distances or flyby rates do not differ in terms of density plots and model maser spectra. Therefore I will present one comparison of them and then focus on the more destructive ones and how it affects the disk and therefore the maser spectrum. For most cases I present the results only for one timestep if there is no significant difference in the density plot or maser spectrum. I have grouped the results according to the mass of the supermassive star and the outer radius of the disk. Since I only model collisionally pumped masers, the model spectra do not include the "low-velocity" features, which is radiatively pumped by the the background infrared radiation, usually by the central object. For the purpose of this thesis, I only focus on the "high-velocity" features in maser spectra. The model maser spectrum shows positive flux at systemic velocity for each simulation run. This is the result of flux being calculated for each area in the disc that meet the density and temperature requirements for maser emission in the line of sight, thus computing the emission as a ring in the disc. Whilst modelling maser emission I do not search for the longest velocity coherence direction, i.e. the direction along which the ray is amplified by the maser action. Nevertheless according to Elitzur et al. [1991] around 51% of the maser emission is lost through the sides, which results in the positive flux around zero velocity. Hence I approximated the values of the flux for those regions and it needs to be taken into consideration when interpreting the results. Direct collisions are purely determined by the values of R_{peri} for each individual stellar perturber, therefore their number are generated through random numbers function; for the case of flyby rate of one stellar perturber per 100 years there is no direct collision ($R_{peri} \leq 10$ au).

4.3.1 M_{SMS} = 1000 $M_\odot$ and R_{out} = 500 au

Firstly I focus on the time evolution of the multiple stellar flybys for the accretion disk with the outer radius of 500 au and mass of 10 $M_\odot$ around a supermassive star with the mass of 1000 $M_\odot$ and the highest flyby rate i.e. one per year within the periastron distance of 550 au. The left column in Figure 4.4 shows density plots for three time steps. A slow, steady and smooth dispersion of the disk is well visible. The gas in the disk is being spread out over 2000 au distance within 5,000 years. The most interesting results are presented in the right column, namely the comparison of the modelled H_2O maser spectra for each time step with the W1 kilomaser [Gorski et al., 2018] plotted orange for direct comparison. The galaxy's recession velocity was added to the modeled velocities for direct comparison to the observed spectrum. The "high-velocity" features are clearly visible on each side, with comparable flux value but velocity values slightly further from the centre than the W1 kilomaser. Those values are approximately 70 and 165 km/s. Using the Equation 3.27 with $\Delta\nu \sim 47.5$ km/s, it gives radius of the maser spots of $\sim$ 400 au. It can also be noticed that the the "high-velocity" feature at around 70 km/s at the time step of 10,000 years has a slightly higher flux to the feature at 165 km/s. Looking at the corresponding density plot it can be observed that the spiral arm has formed, moving clockwise, and therefore overlapping the maser spots located in the accretion disk. Those maser emissions region could be clumpy, where the densities are higher,

which is the case for that part of the spiral arm. Hence since they overlap within the velocity-coherence length along the line of sight, they most likely contribute to the higher flux of the one of the "high-velocity" features [Kartje et al., 1999] in the mentioned maser spectrum. Additionally it can be noticed from the time evolution of the maser spectra in the same Figure that the spikes of the "high-velocity" features are moving slightly inwards or outwards, depending on the location of the spiral arm, visible in the corresponding density plots. That effect is clearly visible in Fig.4.5 with the plot of unperturbed maser spectrum, i.e. at the very beginning of the simulation run and the spectrum produced at 10,000 years.

Those results in comparison to the higher periastron distance of 1000 au are more destructive, as seen in Figure 4.6. In terms of the "high-velocity" features and their values of the flux, they represent the same values as for the lower periastron distance, described above (see Fig. 4.4). The only difference is a lack of the very distinct spiral arms, that could lead to increase of the flux for some of the features. Figure 4.7 represents disk mass evolution for the disk and the SMS with the parameters discussed above but two different values of R_{peri}, 550 and 1000 au. Both of the plots shows that the disk starts to loose a marginal portion of its mass around 6,000 years and the difference between both cases are minimal. It can also be noticed that around 9,000 years the disc reaches its new dynamical equilibrium. In general 99% of the disc mass stays inside the computational domain, hence I can conclude that the size of the computational grid was well chosen.

Since those differences are minimal, I will focus from now on on the more destructive case for the disk with $R_{out} = 500$ au i.e. for the maximum periastron distance of 550 au.

I keep the parameters of the disk and the central star the same as previous cases for the periastron distance of 550 au but now I look at the cases for different stellar flyby rates. Time evolution for the flybys of rate of one perturber per 10 years is presented in Figure 4.8. The gas in the disc is less spread out than in the case of the higher flyby rates, up to the value of 2000 au, but in comparison to the $R_{peri} = 1000$ au in Fig. 4.6, I noticed that for the final density plot at time 10,000 years, the disk is more spread out. In Figure 4.9 for the rate of one perturber per 100 years, the disk slowly develops a spiral arm, that then spreads out further to the value of less than 2000 au, hence as expected the disk is less destroyed than for the case of higher flyby rates. Comparing maser spectra for all the above mentioned cases, I can see that the "high-velocity" features are also appearing at roughly the same value of velocity with similar flux. Hence I can safely assume that the radius of the maser spots are located roughly at the distance of 400 au in the accretion disk. The movement of the spikes for the "high-velocity" features are less visible than for the case of a flyby rate of one per year, as the spiral arm has not developed the dense features yet.

The acceleration of the disc mass depends only on the potential of the central star, but momentum transfer with the background gas does vary if the disc mass is changed. Keeping the more destructive case for the disc i.e. maximum periastron distance of 550 au, I look at the case for more massive accretion disk, $M_{disk} = 100\ M_{\odot}$, presented in Figure 4.10 for the time step at 10,000 years. The top plots represents flyby rate of one per year, and the disk mass is spread out over the distance of almost 4000 au. There is a distinct spiral arm created, that again leads to slightly higher flux

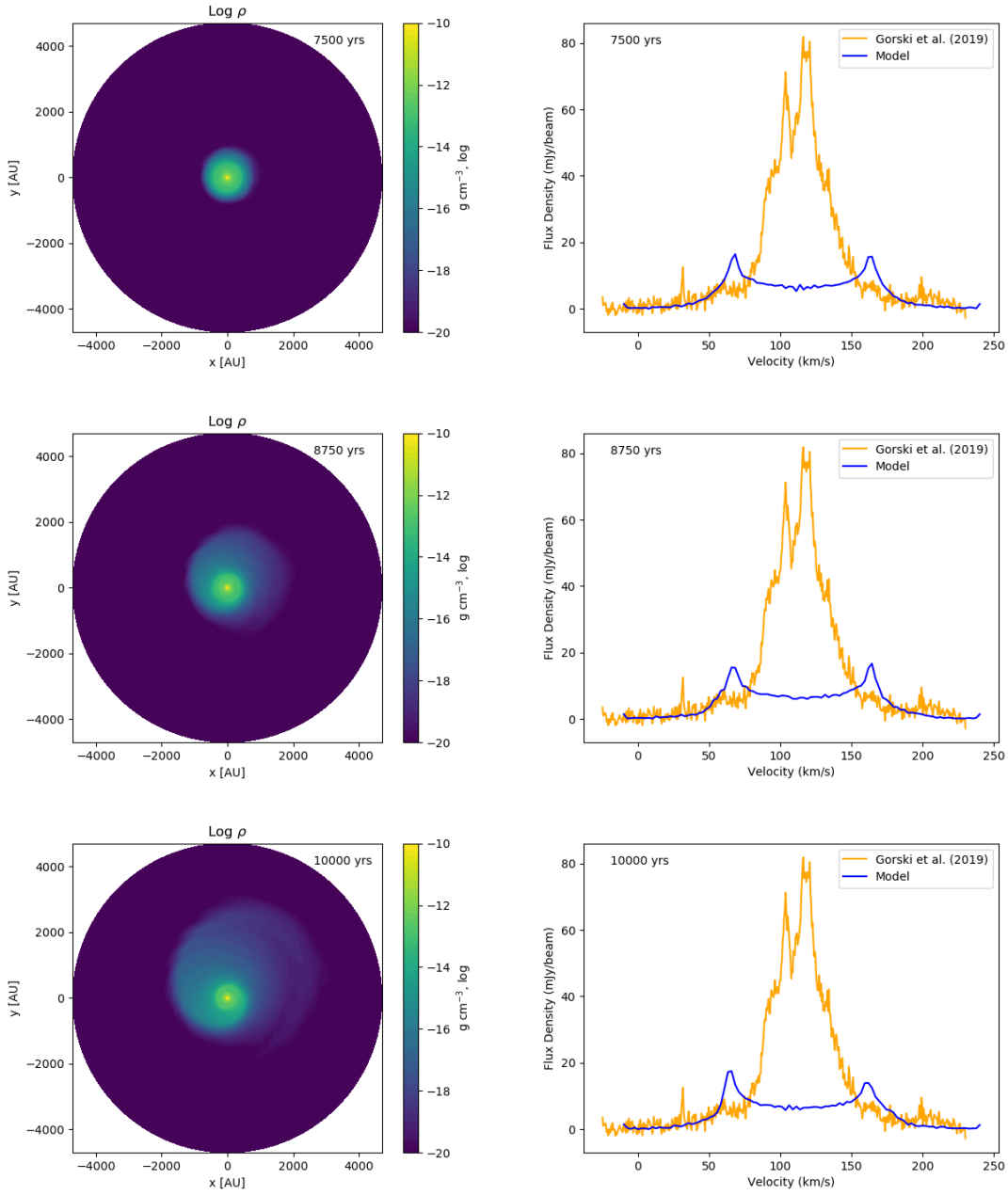

Figure 4.4: Time evolution of a flyby rate of one stellar perturber per year for SMS with $M_{SMS} = 1000\ M_{\odot}$, $R_{out} = 500$ au, $M_{disk} = 10\ M_{\odot}$. The maximum periastron distance is set to 550 au. The left column shows density plots with corresponding maser spectra on the right for selected time steps. The model spectrum is labelled blue, whilst W1 kilomaser from Gorski et al. [2018] for comparison is plotted orange.

in one of the "high-velocity" features in the maser spectrum. The flyby rate of one perturber per 10 years causes less damage than the more frequent case, with the disk spread out slightly over 2000 au. It also shows spiral arm, which causes one of the maser features to spike higher than in any other previous example. The least frequent case (bottom plots) with one flyby every 100 years makes the disc spread out to distances slightly over 1000 au. The maser disc as with previous examples, extend

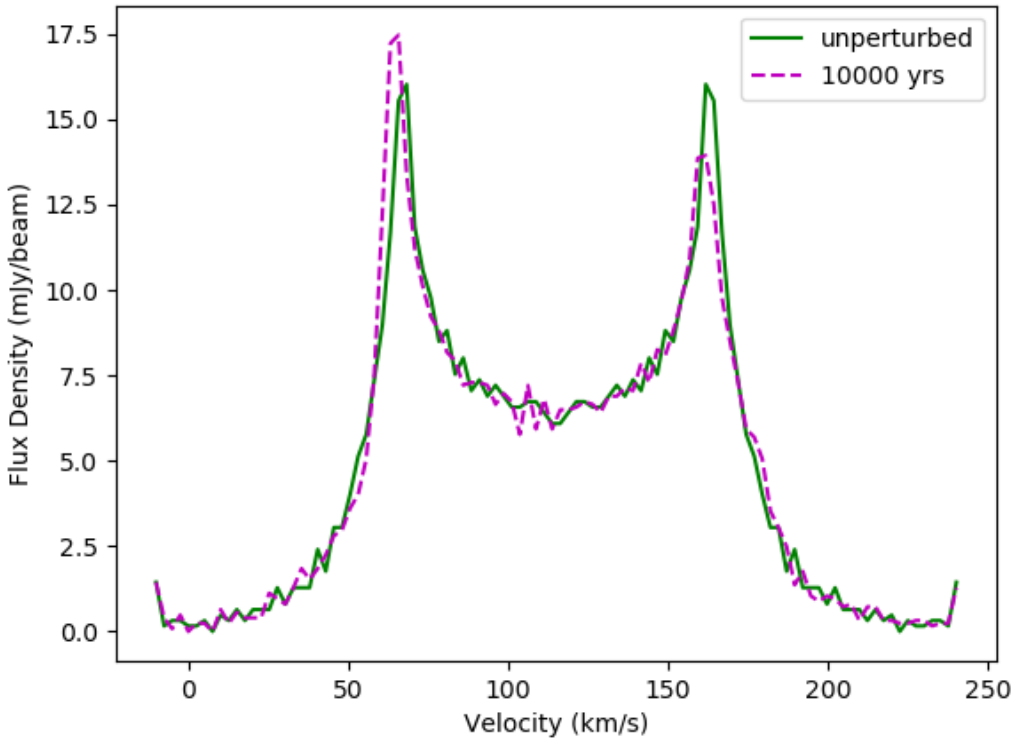

Figure 4.5: Time evolution of the maser spectra for SMS with parameters same as Fig. 4.4. The unperturbed maser spectrum, i.e. at time 0 yr, is plotted green and at 10,000 years is plotted dashed purple.

to the radius of 400 au for each case here. Comparing Figure 4.10 ($M_{disk} = 100\ M_{\odot}$) with previous plots for $M_{disk} = 10\ M_{\odot}$, I notice that the higher the value of the mass of the disk is the more spread out it becomes with the more distinctive features like spiral arms. That is the results of the less interaction with the background gas for higher disc mass. The "high-velocity" features also spike higher and move either inwards or outwards depending on where the spiral arm is positioned.

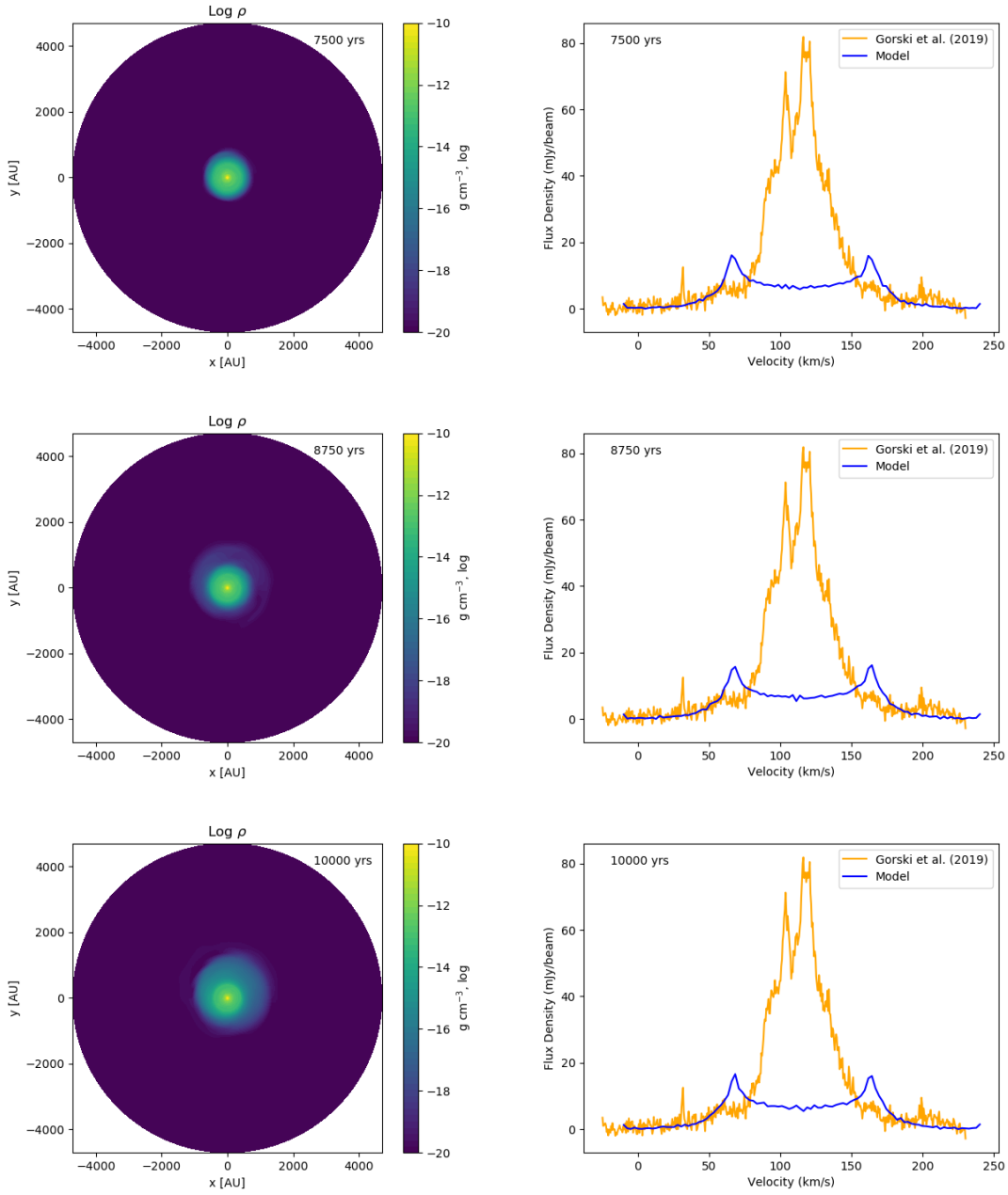

Figure 4.6: Parameters of the simulation are the same as in Figure 4.4. The maximum periastron distance here is set to 1000 au.

4.3.2 M_{SMS} = 1000 $M_\odot$ and R_{out} = 1000 au

Here I will present the results for the most destructive case i.e. a flyby rate of one stellar perturber per year for the case of M_{disk} = 10 $M_\odot$ and M_{disk} = 100 $M_\odot$.

For both of those simulations I note that at around 25,000 years the disk mass that have been spread out to larger distances is reflecting off the boundaries, since there is a large spike in the disk mass evolution plots (seen in Fig. 4.11). Therefore I will only use the results up to that time frame.

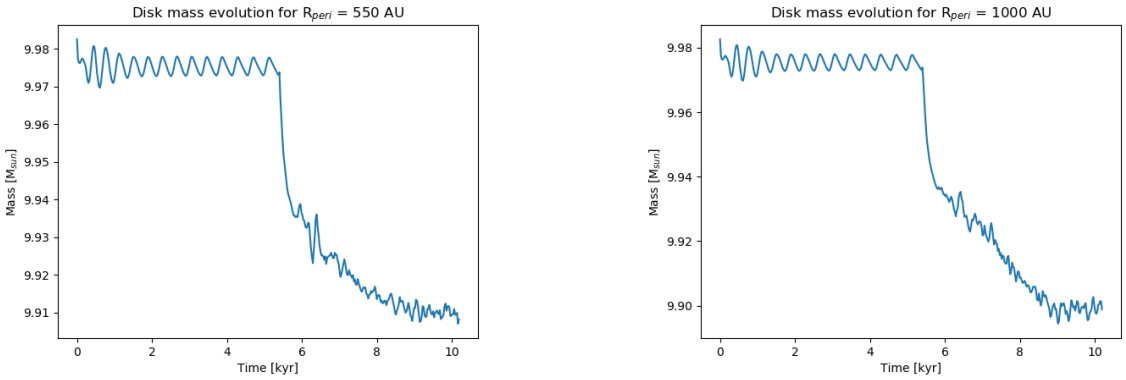

Figure 4.7: Disk mass evolution for SMS with M_{SMS} = 1000 $M_\odot$, R_{out} = 500 au, M_{disk} = 10 $M_\odot$ and a flyby rate of one per year. The maximum periastron distance is 550 au (left image) and 1000 au (right image)

First I look at the results of the simulations for M_{disk} = 10 $M_\odot$, seen in Figure 4.12. At the first timestep of 10,000 years the disk is getting slowly perturbed, as the mass is slowly getting re-distributed over larger orbits with one side being more dense than the other. This reflects on the corresponding maser spectrum where one of the "high-velocity" features at 165 km/s spikes higher than the one at 70 km/s. Using the Equation 3.27, the maser spots in the disk are located at around radius of 355 au and and 440 au, respectively. As the simulations evolve with time, looking at the middle row at around 21,200 years, the mass is being spread out up to the radius of around 7500 au, accompanied with the spiral arm with some distinct dense parts. This feature again impacts the maser spectrum, with again one of the "high-velocity" components having an even higher flux and moving slightly inward to around 160 km/s. That shift corresponds to the maser spot being located now at around 440 au, instead of 355 au. For the last timestep presented in the Figure, just before the mass touches the boundaries, there is a slight spike and a shift outwards to 65 km/s for another "high-velocity" feature. This shift represent a move for that maser spot from 440 au to 355 au during 15,000 years.

Figure 4.13 shows density plots and maser spectra for simulations for the disk mass of 100 $M_\odot$. At the time of 10,000 years the disk is just starting to react to the oncoming perturbers with the maser spectra showing "high-velocity" features at the same values of velocity, 70 km/s and 165 km/s, as for the previous case of M_{disk} = 10 $M_\odot$ (see Fig. 4.12). Those values represent radius of maser spots at around 440 au and 355 au. One of the features, 70 km/s, spikes higher at 18,800 years due to the spiral arm moving and therefore creating higher density along the line of sight for maser emission. The bottom row shows the spiral arm moved within around 2,000 years, which caused the other "high-velocity" feature to spike. As found out in the previously discussed case, both of those velocity features have moved slightly to the velocity values of 65 km/s and 160 km/s. This results in the radius of maser emission at around 355 au and 438 au in the disk.

4.3.3 M_{SMS} = 10,000 $M_\odot$ and R_{out} = 500 au

As I have mentioned before, for the simulations where there are two cases of maximum periastron, I will analyse and present the more destructive ones, if there is no

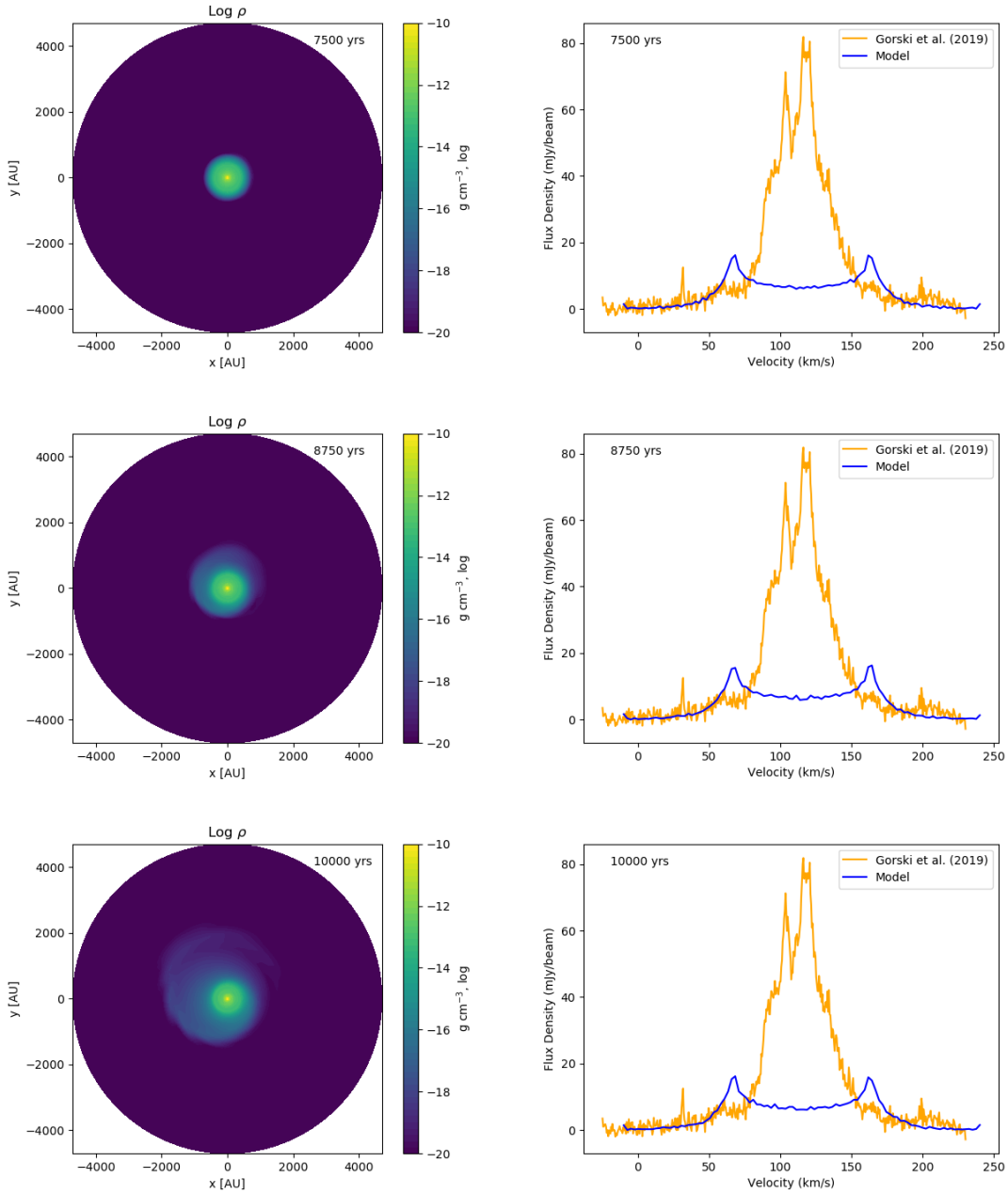

Figure 4.8: Time evolution of a flyby rate of one stellar perturber per 10 years for SMS with $M_{SMS} = 1000\ M_{\odot}$, $R_{out} = 500$ au, $M_{disk} = 10\ M_{\odot}$. The maximum periastron distance is set to 550 au. The left column shows density plots with corresponding maser spectra on the right for selected time steps. The model spectrum is labelled blue, whilst W1 kilomaser from Gorski et al. [2018] for comparison is plotted orange.

significant changes in the results. Hence for the parameters of $M_{SMS} = 10{,}000\ M_{\odot}$ and $R_{out} = 500$ au I will only focus here on maximum periastron distance of 550 au, as in section 4.3.1. I will again analyse the most destructive case for the disk of $M_{disk} = 100\ M_{\odot}$ and $M_{disk} = 1000\ M_{\odot}$, meaning a flyby rate of one stellar perturber per year.

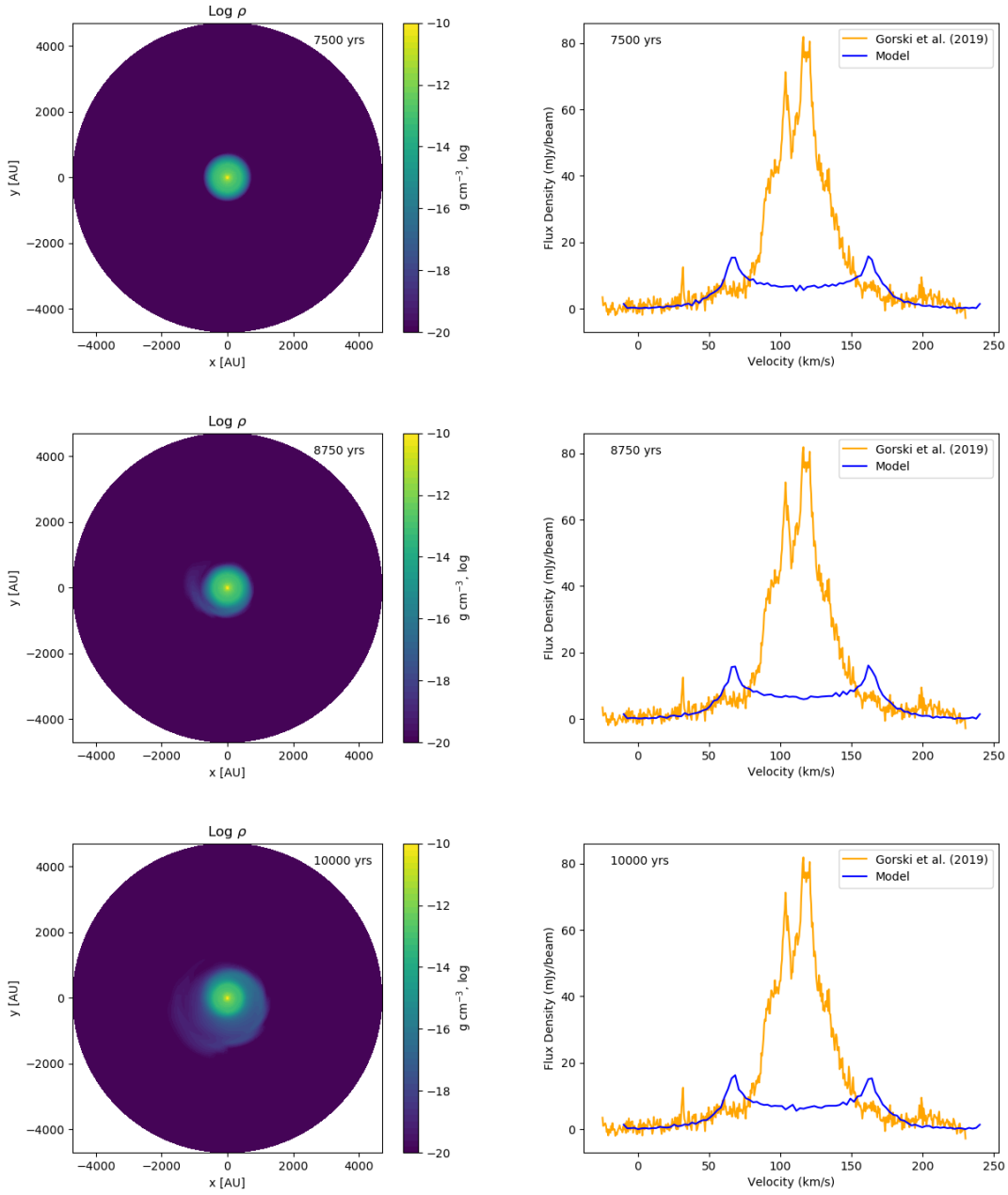

Figure 4.9: Parameters of the simulation are the same as in Figure 4.8 with a flyby rate of one per 100 years.

Figure 4.14 shows disk mass evolution for the parameters described above and both cases of different disk masses. As with the simulations described in the previous section, the computational grid should be extended to at least 10,000 au, as at around 8,000-9,0000 years there is an increase in mass. This is the consequence of the disk's mass being spread out and reflecting back upon touching the boundaries.

I will focus first on the case of $M_{disk} = 100\ M_{\odot}$ using simulations only up to 9,000 years, shown in Figure 4.15. Comparing it to the case of lower M_{SMS} (see top density plot in Figure 4.10) but keeping the other parameters the same, I notice that the disc spreads out faster, with more frequent spiral arms and more mass reaching a

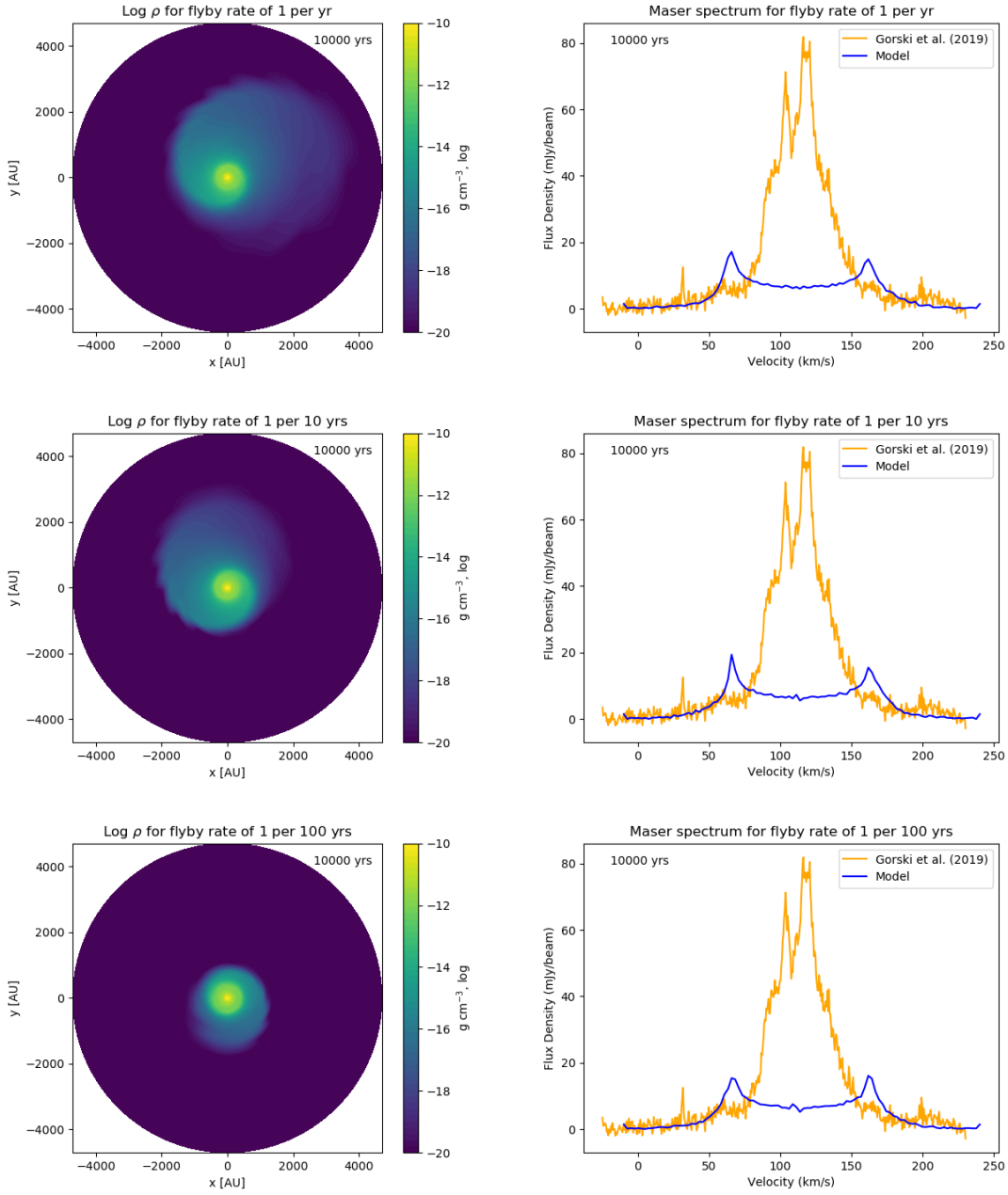

Figure 4.10: Density plots and maser spectra for flyby rates of 1 stellar perturber per 1, 10 and 100 years (top to bottom, respectively) for SMS with M_{SMS} = 1000 $M_{\odot}$, R_{out} = 500 au, M_{disk} = 100 $M_{\odot}$. The maximum periastron distance is set to 550 au. The left column shows density plots with corresponding maser spectra on the right for selected time steps. The model spectrum is labelled blue, whilst W1 kilomaser from Gorski et al. [2018] for comparison is plotted orange.

larger radius. It is hard to establish what maximum distance the mass could reach since I am limited by the computational grid (up to 5000 au). Since the spiral arms and the mass rotates much faster than the previous cases, the velocity-spread in the maser spectrum (right column on the Fig. 4.15) had to be extended to 800 km/s in order to see "high-velocity" features, which appear first symmetrically located at

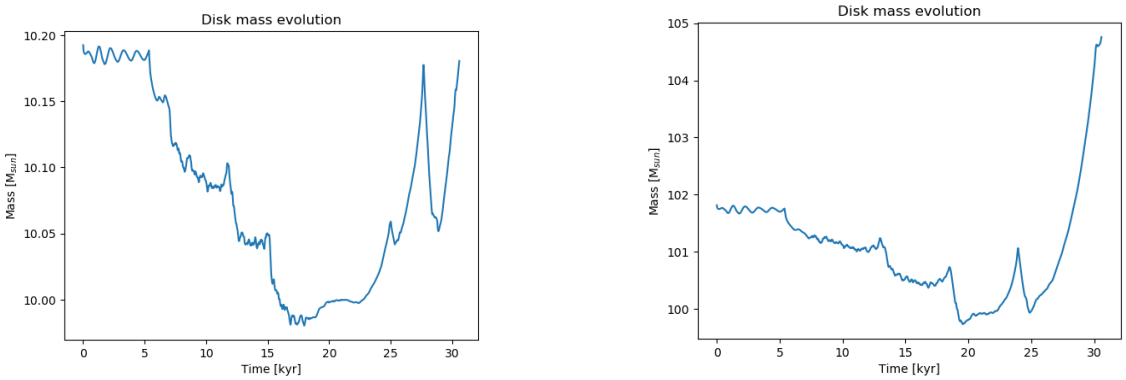

Figure 4.11: Disk mass evolution for SMS with M_{SMS} = 1000 $M_\odot$, R_{out} = 500 au a flyby rate of one per year. Left image shows M_{disk} = 10 $M_\odot$ and right one M_{disk} = 100 $M_\odot$.

around -40 km/s and 270 km/s. Those values gives $\Delta\nu \sim 155$ km/s, with Equation 3.27 I get the radius of maser spot of $\sim$ 369 au. As the disk evolves with time, the mass and spiral arms spread out more (middle row in Fig. 4.15), keeping the maser spectrum in similar shape. At around 8,000 years the "high-velocity" features start either moving slightly outwards from -40 km/s to -45 km/s and from 270 km/s to 275 km/s, leading to the maser spots being now located at the radius of 346 au, therefore slightly closer to the central star. One of the spikes has also increased its flux due to the spiral arm moving and increasing column density along the line of sight, as clearly seen in Fig. 4.16.

Figure 4.18 represents time evolution of the simulation with the M_{disk} = 1000 $M_\odot$. Since the computational grid is set up to 5000 au, therefore the mass reaches the boundaries at around 8,000 years and reflects back, leading to an increase of mass after that timestep. Hence, I will only use the results up to that time. The first row shows density map at around 6300 years with the disk's mass spread out to the distance over 2000 au, hence more spread out than the case of lower M_{disk} of 100 $M_\odot$. At this time step the "high-velocity" features appear symmetrically distributed at around -40 km/s and 270 km/s, again similar to the previous case with a lower disc mass. 700 years later the disk spreads out much further reaching the maximum radius of the grid, 5000 au. At this time one of the features in the maser spectrum spikes higher and shift outwards to the value of around -50 km/s, caused by the dense parts of the spiral arm rotating. This "high-velocity" features corresponds to the maser spot located at the radius of 325 au, whilst the other stays at the value of 370 au. As the simulation progress further the spiral arm spreads out further and the mass keeps accumulating at the boundaries with the "high-velocity" features in the maser spectrum still being located at the same position but one of the spikes is decreasing its flux value.

4.3.4 M_{SMS} = 10,000 $M_\odot$ and R_{out} = 1000 au

The below simulations for M_{SMS} = 10,000 $M_\odot$, R_{out} = 1000 au and M_{disk} = 100 $M_\odot$ and M_{disk} = 1000 $M_\odot$ for the most destructive case of flyby rate of one stellar perturber per year have, as for the previous cases, mass reflecting back on touching

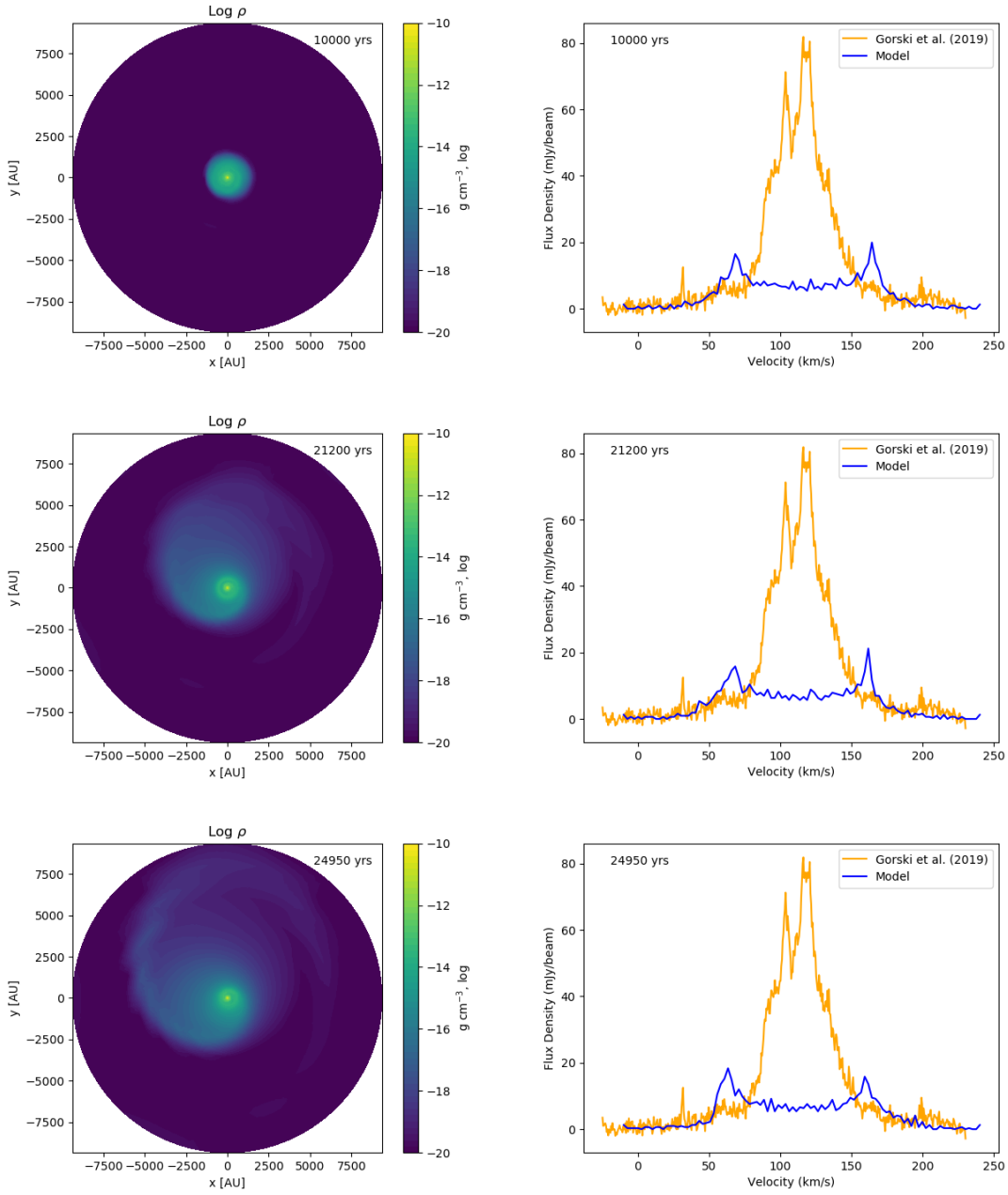

Figure 4.12: Time evolution of a flyby rate of one stellar perturber per year for SMS with M_{SMS} = 1000 $M_\odot$, R_{out} = 1000 au, M_{disk} = 10 $M_\odot$. The left column shows density plots with corresponding maser spectra on the right for selected time steps. The model spectrum is labelled blue, whilst W1 kilomaser from Gorski et al. [2018] for comparison is plotted orange.

the boundaries of computational grid. This can be noticed in the disk mass evolution plots for simulations with varying M_{disk} in Figure 4.17, where there is a steep increase of the mass at around 12,000 years. Hence I will only take into account the results from the simulations up to that timestep.

In Figure 4.19, the top row presents the density plot just when the disk with the mass of 100 $M_\odot$ starts to react to the flybys of multiple perturbers. As the mass just

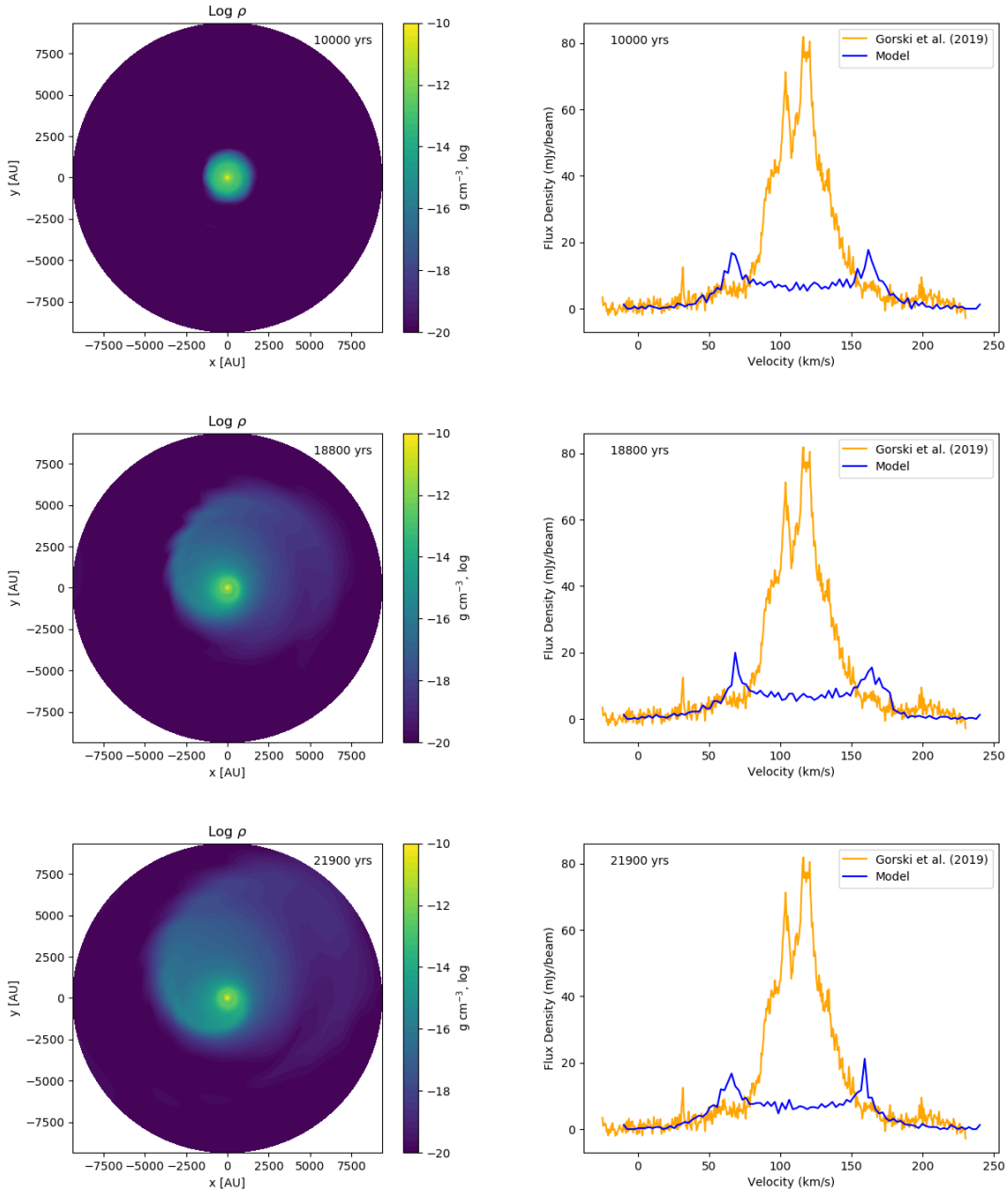

Figure 4.13: Time evolution of a flyby rate of one stellar perturber per year for SMS with $M_{SMS} = 1000\ M_{\odot}$, $R_{out} = 1000$ au, $M_{disk} = 100\ M_{\odot}$. The left column shows density plots with corresponding maser spectra on the right for selected time steps. The model spectrum is labelled blue, whilst W1 kilomaser from Gorski et al. [2018] for comparison is plotted orange.

starts to spread out, the "high-velocity" features in the corresponding maser spectrum are located roughly symmetrically around systemic velocity with their spikes at -30 km/s and 270 km/s. Those values corresponds to a radius distance of maser spots of around 420 au and 370 au. Similarly to the previously discussed simulations, as the mass spreads out to larger distances, those maser features spike higher, depending on the position of the densest parts of the spiral arm. The time of 9600 years the

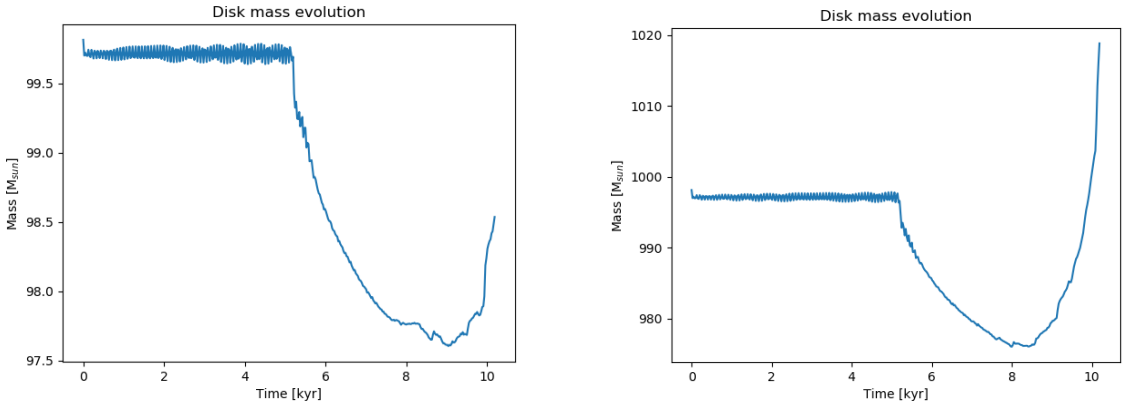

Figure 4.14: Disk mass evolution for SMS with M_{SMS} = 10,000 $M_{\odot}$, R_{out} = 500 au and R_{peri} = 550 au for a flyby rate of one stellar perturber per year. Left image represents disk with mass of 100 $M_{\odot}$, and the right one shows M_{disk} = 1000 $M_{\odot}$.

spikes move from 270 km/s to the value of 280 km/s, hence the maser spots moved from 370 au to 325 au, there is also a slight increase in the flux value. That same spike moves back to the the value of 270 km/s as its flux value decreases, that again correlates to the further movement of the spiral arm. On the other hand the other "high-velocity" feature moves from -30 km/s to -40 km/s, which results in the maser spot moving from 420 au to around 370 au.

Figure 4.20 shows results of the simulations with the disk's mass increased to 1000 $M_{\odot}$. As expected, I notice that there is more mass being spread out to a slightly larger distances to the previous case of M_{disk} = 100 $M_{\odot}$. The "high-velocity" features, present at velocities of -30 km/s and 270 km/s at time of 7150 years, represents maser spots located in the disk at the radius of 420 au and 370 au, respectively. Those results are very similar to the case of lower M_{disk}, discussed above. As the disk evolves with time, the peaks are staying at the same velocity values around 2500 years later and moving slightly outwards or inwards (values of around $\pm$ 1-5 km/s) at the time of 1100 years. Those changes could lead to the maser spots location being shifted by around 4-14 au either way.

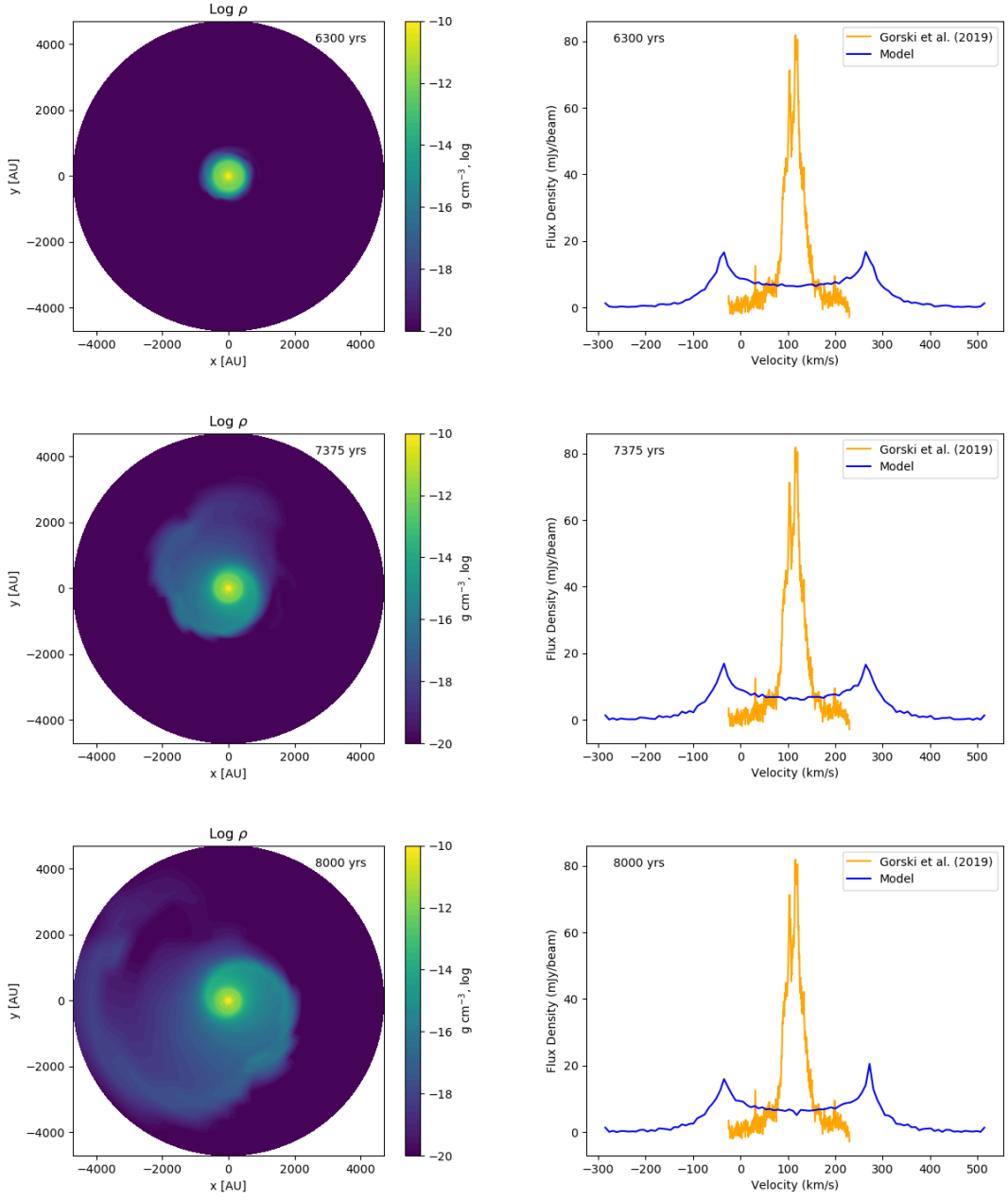

Figure 4.15: Density plots and maser spectra for a flyby rate one stellar perturber per year for SMS with M_{SMS} = 10,000 $M_{\odot}$, R_{out} = 500 au, M_{disk} = 100 $M_{\odot}$. The maximum periastron distance is set to 550 au. The left column shows density plots with corresponding maser spectra on the right for selected time steps. The model spectrum is labelled blue, whilst W1 kilomaser from Gorski et al. [2018] for comparison is plotted orange.

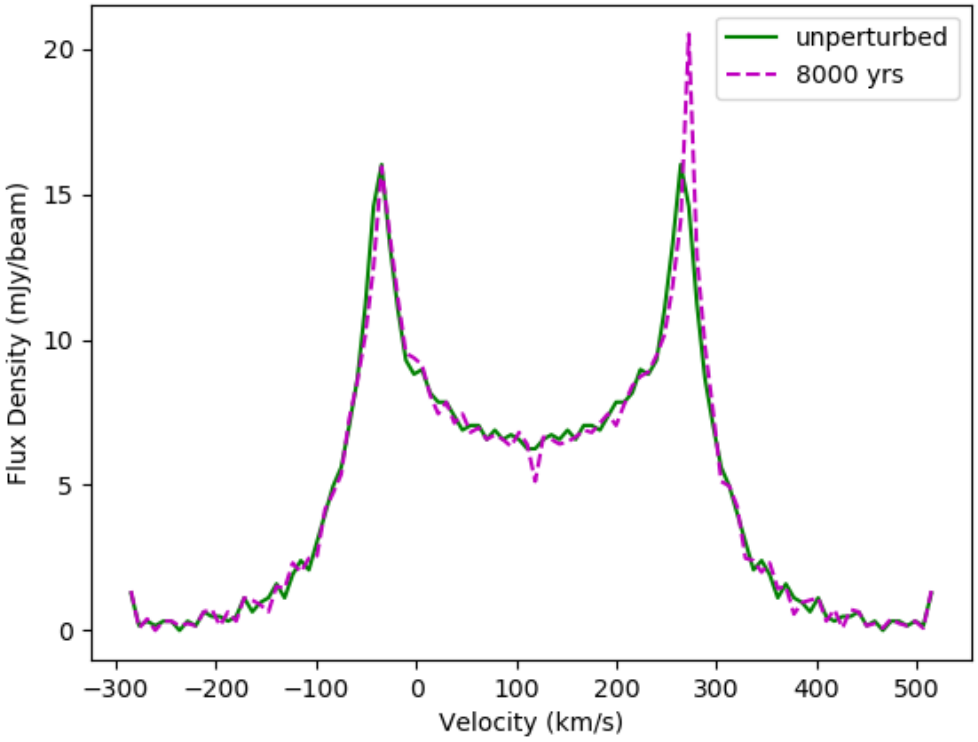

Figure 4.16: Time evolution of the maser spectra for SMS with parameters same as Fig. 4.15. The unperturbed maser spectrum, i.e. at time 0 yr, is plotted green and at 8000 years is plotted dashed purple.

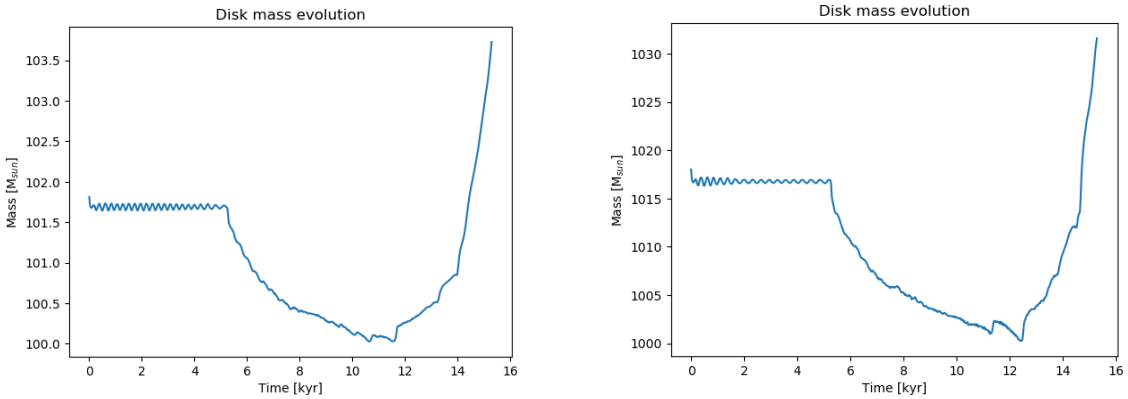

Figure 4.17: Disk mass evolution for SMS with M_{SMS} = 10,000 $M_\odot$ and R_{out} = 1000 au for a flyby rate of one stellar perturber per year. Left image represents disk with mass of 100 $M_\odot$, and the right one shows M_{disk} = 1000 $M_\odot$.

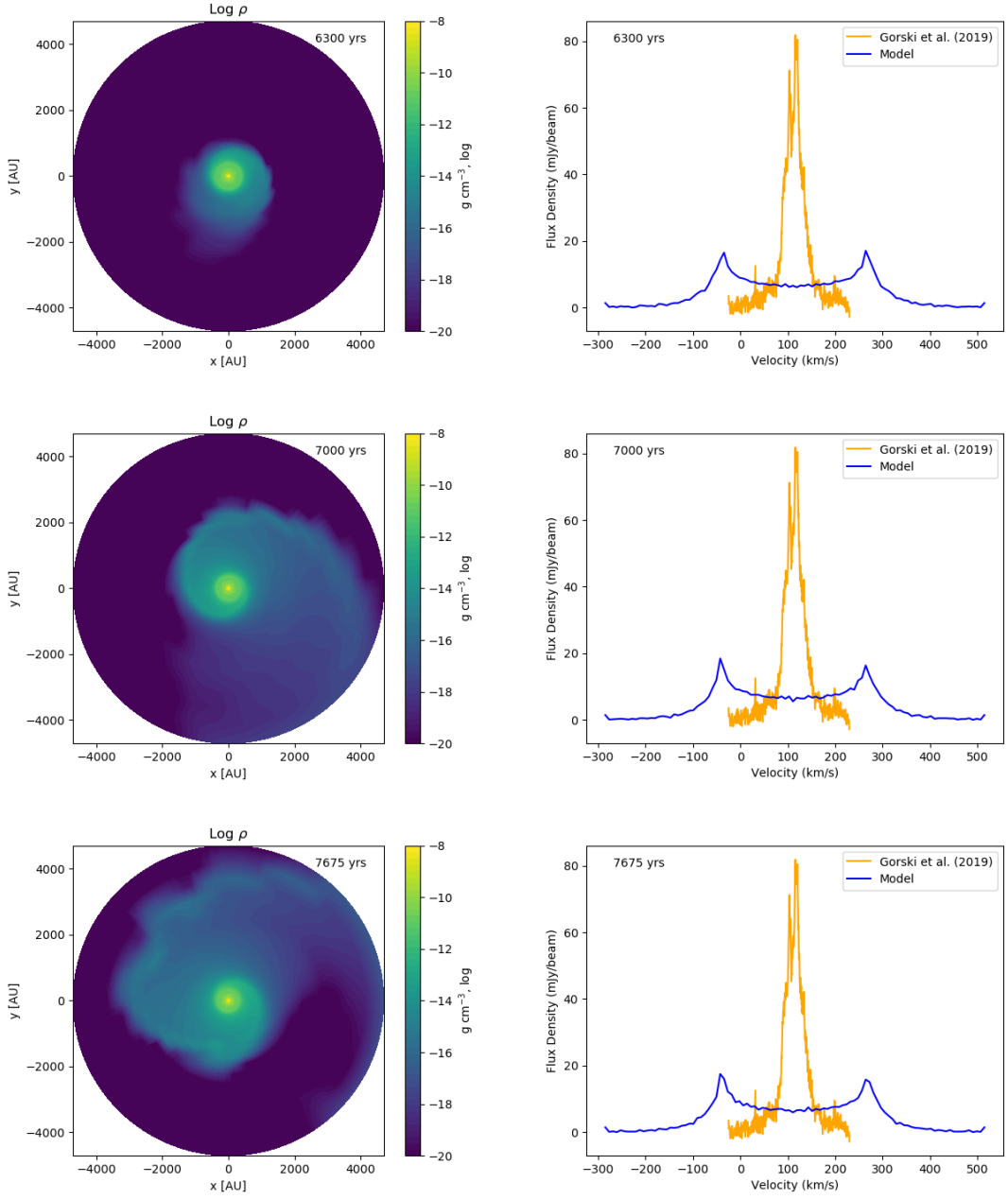

Figure 4.18: Density plots and maser spectra for flybys and direct collisions of rate 1 stellar perturber per 1, 10 and 100 years (top to bottom, respectively) for SMS with M_{SMS} = 10,000 $M_\odot$, R_{out} = 500 au, M_{disk} = 1000 $M_\odot$. The maximum periastron distance is set to 550 au. The left column shows density plots with corresponding maser spectra on the right for selected time steps. The model spectrum is labelled blue, whilst W1 kilomaser from Gorski et al. [2018] for comparison is plotted orange.

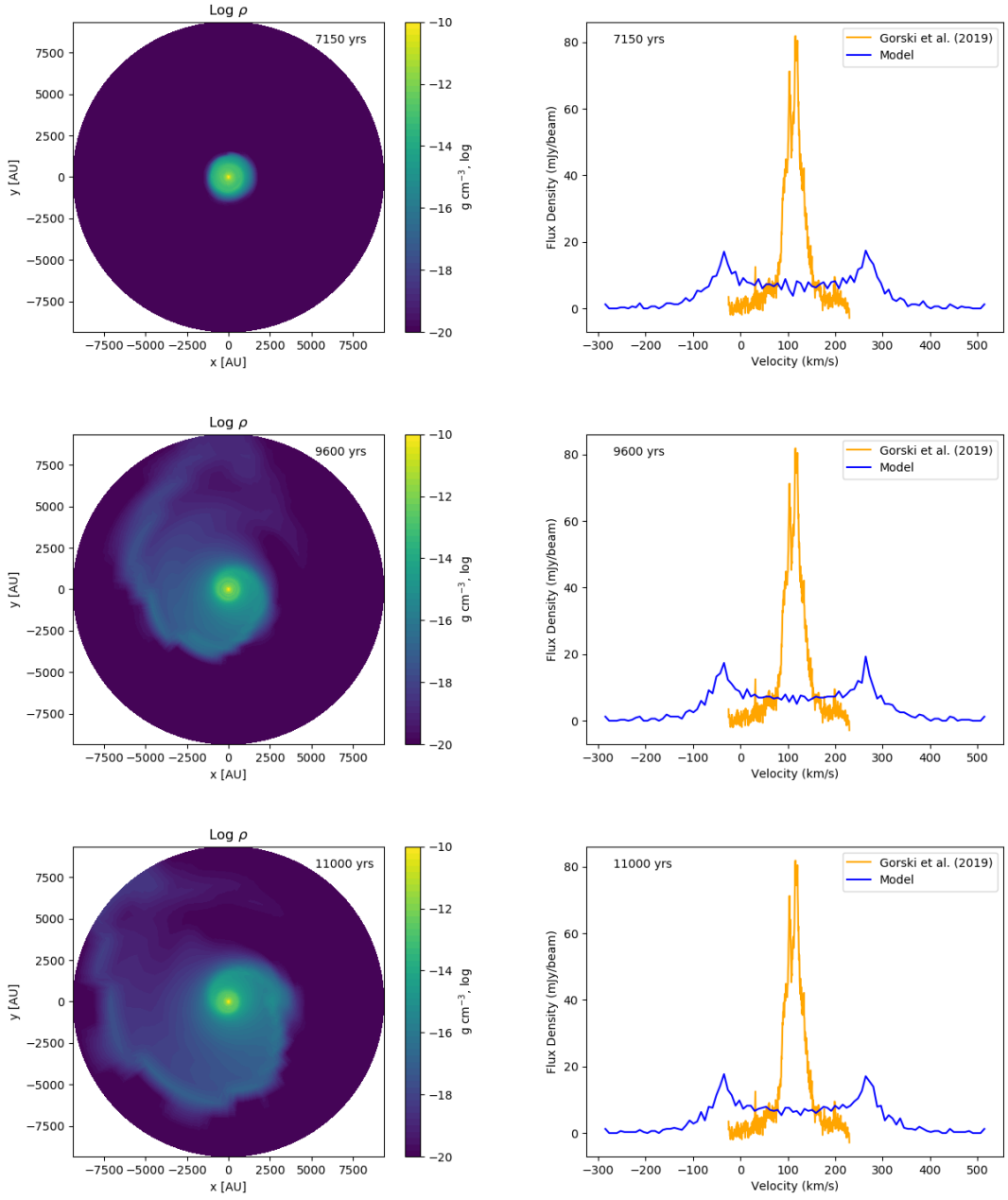

Figure 4.19: Density plots and maser spectra for a flyby rate one stellar perturber per year for SMS with M_{SMS} = 10,000 $M_{\odot}$, R_{out} = 1000 au, M_{disk} = 100 $M_{\odot}$. The left column shows density plots with corresponding maser spectra on the right for selected time steps. The model spectrum is labelled blue, whilst W1 kilomaser from Gorski et al. [2018] for comparison is plotted orange.

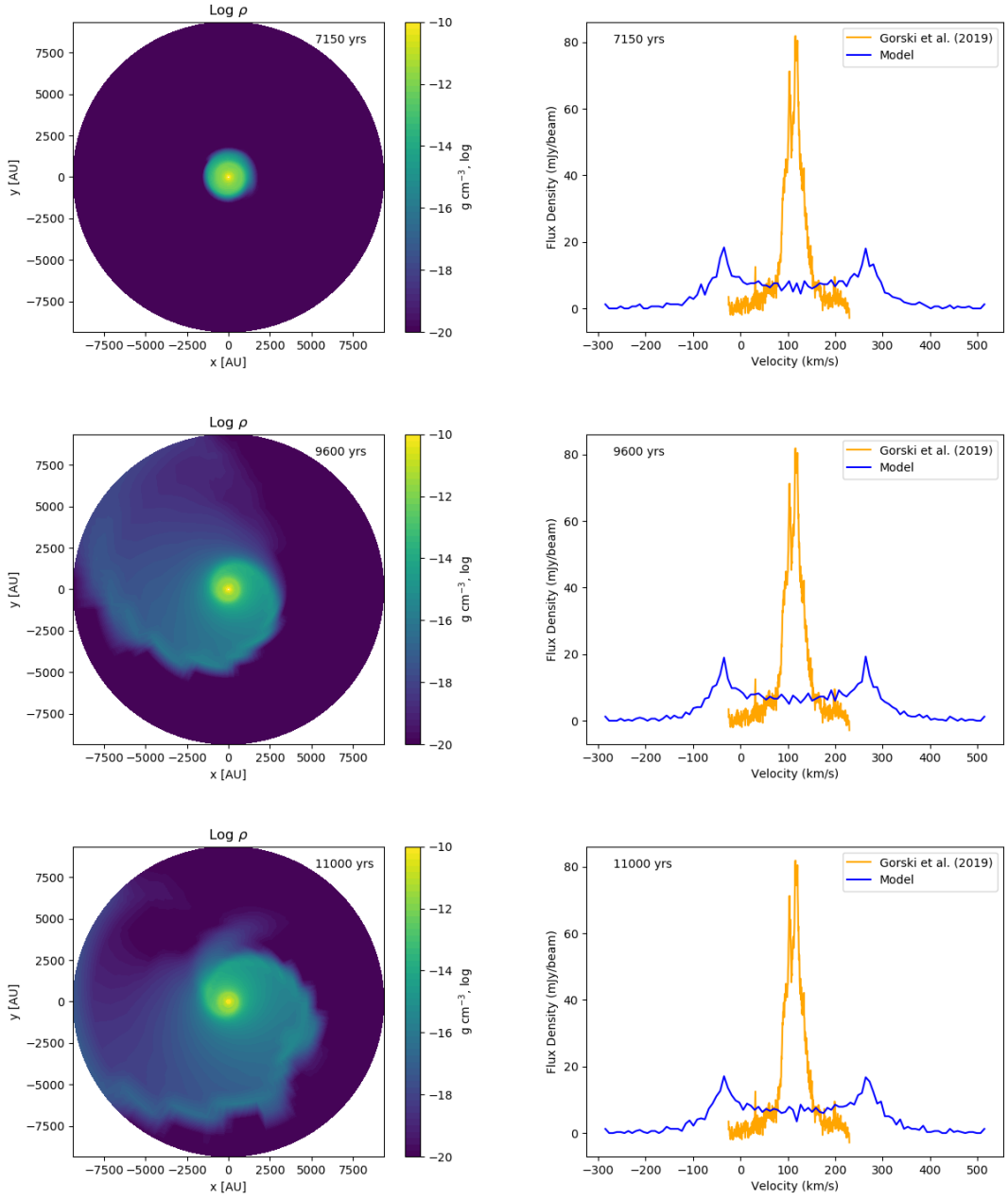

Figure 4.20: Density plots and maser spectra for a flyby rate one stellar perturber per year for SMS with M_{SMS} = 10,000 $M_\odot$, R_{out} = 1000 au, M_{disk} = 1000 $M_\odot$. The left column shows density plots with corresponding maser spectra on the right for selected time steps. The model spectrum is labelled blue, whilst W1 kilomaser from Gorski et al. [2018] for comparison is plotted orange.

5. Discussion

5.1 Analysis of the simulations

With the aim of achieving the highest quality results in the simulations I have progressively changed the set up of the standard disc-Planet problem included in the PLUTO code to the multiple flybys around a supermassive star. I have tested different resolutions, using the lowest one that allowed me to minimize the CPU time, without compromising the quality of the numerical results.

The results of running the standard problem and changing the potential from a static to a moving one, presented in Figure 4.1, show that the Jupiter size planet creates spiral arms in the circumprimary disc and in the case of static potential (left image) it also creates gaps in close proximity to the planet. This could possibly lead to narrow gaps in the accretion disc if the simulation was left to run for longer. Those findings agree with hydrodynamical simulations performed by Zhang et al. [2018], where they find that single planets of similar size to Jupiter can cause gap/ring substructures. The observations provided by the disc Substructures at High Angular Resolution Project (DSHARP) from ALMA, cover a large sample of protoplanetary discs [Andrews et al., 2018]. The data shows that at wide range of radii in the disc, apart from narrow gaps, there are also some large-scale spiral patterns found.

From there on I have reproduced the parabolic stellar flyby simulations by Cuello et al. [2018], where I have adapted the Smooth Particle Hydrodynamics (SPH) code to mesh grid based one. Top row in the Figure 2 in Cuello et al. [2018], presents coplanar and prograde parabolic stellar flyby for a periastron distance of 200 au, where both perturber and central star have a mass of 1 $M_{\odot}$. I have recreated this set up, shown in the middle row in Figure 4.2. Comparing both of those results, I can clearly see that the simulation I have produced shows that the disc behaves in the similar manner as the original simulations by Cuello et al. [2018]: the mass gets stripped from the disc, when the perturber is at the periastron distance, followed by creation of a spiral arm. In both cases after the perturber is about to leave the computational grid the disc is starting to take its original shape with only one spiral arm visible. Both of those results also agrees with the findings from Clarke

and Pringle [1993], where they show that in the coplanar and prograde encounter a fraction of the disc mass gets stripped off at the closest approach, creating a bridge between the stellar perturber and the disc. Their findings also confirm that some of that stripped mass forms a spiral arm and the mass that is more tightly bound to the central star is taking its original shape. On the other hand the results from Cuello et al. [2018] show smoother distribution of mass and more distinct features, which is the result of using Smooth Particle Hydrodynamics. The simulations that use the SPH do not have a background gas, thus there is no interaction with it. The results presented in this thesis are more 'realistic' since there is an application of the low value background gas and visible interaction of the disc mass with it. Following this comparison, I have confidence in my method, hence I can assess the consequences perturbers have on the disc in the simulations with adjusted parameters for the supermassive star.

Further on, I have also run simulations for 'direct stellar collisions', when $R_{peri} \leq$ 10 au, seen in Figure 4.3. Comparing the density plots to the single stellar flyby ones, presented in Figure 4.2, I notice the circumprimary disc retains its original shape after the collision, as it happens for the stellar flybys. The difference between the two types of simulations is the shape of the mass that was striped off the disc. The direct collision density plots show the mass being pulled out to the distance of almost 3000 au, whilst for the case of $R_{peri} = 100$ au (top right plot in Fig. 4.2) the mass reaches the distance of around 2000 au.

In the multiple stellar flybys around the supermassive star, a single 0.2 $M_\odot$ stellar perturber does not have any influence on the central star and its disc. However multiple perturbers of that low mass do have a consequences on the disc, for all the chosen simulations parameters. Taking the case of the most destructive flyby rate of one stellar perturber per year for the 1000 $M_\odot$ star, where I have entered 5000 perturbers of 0.2 $M_\odot$ mass onto the computational domain, the total mass does add up to 1000 $M_\odot$. The total mass of the perturbers therefore equals the mass of the central star, the SMS. Indeed, the overall magnitude of the effects on the accretion discs are very comparable, in particular, the disc spreads out. But comparing the case for the 10 $M_\odot$ accretion disc (Fig. 4.4) with the single stellar flyby seen in Figure 4.2, I also noticed some differences: the density plots of a single perturber parabolic flyby show the disc mass being pulled out as one track, often the shape is reminiscent of spiral arms, whilst multiple flybys show much smoother structure with no preferred direction of the ejected mass from the disc. This is of course an expected consequence of the isotropic bombardment of the disc by the large number of stellar perturbers hitting over a long time allowing the mass distribution to become more homogeneous over larger distances.

Looking at the simulations where the disc mass has increased, either from 10 $M_\odot$ to 100 $M_\odot$ or 100 $M_\odot$ to 1000 $M_\odot$, it is noticeable that the disc mass is being spread out over larger distances. Since the acceleration is only proportional to the potential of the central star, the amount of mass in the disc does not dictate how fast the gas rotates, only the mass of the central star does. As mentioned previously there is an interaction of the disc mass with the background gas. This interaction is driven by

momentum transfer and/or overpressure, where the ram pressure of the spreading disc gas is:

$$p_{\mathrm{ram}} = \rho_{\mathrm{disc}} v^2, \tag{5.1}$$

and the thermal pressure of the background gas is:

$$p_{\mathrm{th}} = \rho_{\mathrm{background}} \mathrm{cs}^2. \tag{5.2}$$

Comparing simulations for both 1000 $M_\odot$ star and 10,000 $M_\odot$, the disc gas rotates much faster for the larger star. For the more massive discs, 10% of the mass of the star, there is more mass available to be spread outwards and the spiral arm becomes more distinct i.e. dense, therefore it does gives us the impression of the more destroyed disc. This also shows that the background gas, with its chosen low value, is still of some significance for the spreading of the gas.

5.2 Model maser spectrum

Pesce et al. [2015] has defined a 'clean' disc maser, as an edge-on maser in a Keplerian rotation structure around a central body. The maser spectrum must show at least two of the three characteristics to be categorised as such: the 'low-velocity' feature, close to the systemic velocity, where water lines are radiatively pumped through the disc from the central object and two 'high-velocity' features, that are offset from systemic velocity of its host object, and are collisionally pumped. The model maser spectra produced in this thesis successfully reproduce the 'clean' disc maser case, as they have two of the features mentioned above: both the 'high-velocity' features. Moreover, as I am only simulating collisionally pumped maser emissions, therefore the systemic feature is not present in those model. In order to model those features, the simulation would have to include background infrared radiation from the central source.

To calculate the flux in the maser model I used Equation 2.13 taken from Kartje et al. [1999]. This expression is considered to be a general formula, assuming optimal collisional pumping conditions. The authors of the paper derive the equation, by considering a velocity-coherence 'box', to which the maser emission is confined to (see Equation 9 in the Kartje et al. [1999]) and the maser features lie in a disk with a plane aligned with the observer. In this model I have applied a decent understanding of physics, especially in terms of maser emissions and the calculation of the flux, mentioned above. The results that I obtained from the simulations are in agreement with the observations: flux values in the order of magnitude correct to the W1 kilomaser from Gorski et al. [2018].

In general the scaling of the model spectra for the simulations for 1000 $M_\odot$ supermassive star is consistent with the W1 kilomaser. I can see similarities in the features with the observed kilomaser, nevertheless I cannot claim that I produce details of the object in my models. Apart from similar fluxes, especially for both 'high-velocity' features, there is a general trend for the signal to follow an increase towards the systemic velocity for the left hand side of the maser for all the models. However looking at the right hand side, the model does not follow the trend of the signal of the W1 kilomaser for the models in all the cases of different parameters.

The models for the higher mass SMS, 10,000 $M_\odot$ does not scale right to the W1 kilomaser. The velocity range was substantially increased in order for the two 'high-velocity' features to be visible. The model maser for the higher mass of the central star, starts to resemble spectra for AGN megamasers, in terms of the offset of those features from systemic velocity. Those results agree with the previous statement, that the kilomaser spectrum, in terms of its luminosity versus velocity-spread relations, lies somewhere between stellar maser and megamasers in AGN, as shown in Figure 2.6. Thus summarising the above findings, the model spectra from simulations for the $M_{SMS} = 1000\ M_\odot$ are a better match with the W1 kilomaser spectrum from Gorski et al. [2018].

The maser spots are located roughly in the distance between 325-440 au, for all the models. The 'high-velocity' features do not appear closer to the inner radius and the center. As shown in Figure 3.3, the temperature increases closer to the center and decreases with the distance approaching the outer radius. The H_2O molecule is dissociated close to the star where $T > 1500$ K. Those conditions does not allow for the water to stay molecular, hence the 22 GHz H_2O lines cannot be mased. Similarly the required water level population inversion does not occur at a larger distances, where temperature remains below 300 K.

The model maser spots move inwards and outwards within that distance range, depending on how the spikes of the 'high-velocity' features move. This in turn depends on the movement of the spiral arm, and its density. The higher the disc mass, the more it spreads out and the denser the spiral arm is. I do not notice the redshifted high-velocity sources to be more numerous and more intense than blueshifted ones in the model masers corresponding to density plots with dense spiral arms. This has been notice in some of the megamasers from the galaxy, like NGC 4258 (seen in top right image in Fig. 2.4). Maoz and McKee [1998] argue that this Doppler shift asymmetry can arise to due spiral shocks in the circumnuclear disc.

I have assumed that the disc is edge on to the observer, but if the disc is inclined then the maser spectrum might start showing slight changes, i.e. decrease in the velocity and flux values, especially of the 'high-velocity' features. As the edge on disc is 90°, if the disc would then be observed at some small angle i.e. 85°, then the flux and velocity values in maser spectrum will show a slight decrease in their values, as $\sin 85° \sim 0.996$. The inclination is well constrained by the fact that I see maser spots, and that the observed velocities are hardly affected by a quite possible small deviation from an 'edge-on' disc.

The 'high-velocity' peaks in the W1 kilomaser (see left image in Figure 2.4) are observed at 31.6 and 199 km s^{-1}. Knowing from the results of the simulations, the model spectra for $M_{SMS} = 1000\ M_\odot$ show a smaller velocity spread between that peaks whilst for the $M_{SMS} = 10{,}000\ M_\odot$ it is larger. I can already conclude that in order for the model peaks to appear at the same velocity values as the W1 kilomaser, the M_{SMS} value needs to be set between the two extreme values used in this thesis. I mentioned before that the maser spots for both cases are located between 325-440 au, with the average value, $R_{out} = 382$ au. The mean value of velocity spread between systemic and peak velocity of W1 kilomaser spectrum is $\Delta\nu = 83$ km s^{-1}. Using

those values and the Equation 3.27, I estimate the value of $M_\star$ that would produce a maser spectrum with aligned peaks to W1 kilomaser:

$$M_\star = \frac{\mathrm{R_{out}}\Delta\nu^2}{\mathrm{G}}, \tag{5.3}$$

which roughly gives me a value of $M_\star \sim 2965\ \mathrm{M_\odot}$. If I would take the top value of $\mathrm{R_{out}} = 440$ au, then $M_\star = 3416\ \mathrm{M_\odot}$. Knowing what radius range the maser spots are located in I can estimated the mass range of supermassive star needed in order for future simulations to produce the model maser with peaks aligned with the W1 kilomaser.

6. Conclusion

In this investigation I have used the extreme case scenarios for the accretion disk, and proved that in the extreme cases, the disk is able to survive and have high enough density to be able to mase the water lines. I have demonstrated model of multiple stellar flyby around accretion disk of SMS, since the results from the test simulations are in reasonable agreement with the findings produced by Cuello et al. [2018].

The range of parameters included plausible upper and lower limits, in terms of number of perturbers entering the grid at a given time, mass of the accretion disk and its outer radius as well as the mass of the central supermassive star. I have proved that even though the flyby rates have been varied, the model maser spectra did not show significant difference for each of them. Further on I have focused on the most destructive case for the disk i.e. the flyby rate of one stellar perturber per year, as well as including only prograde and coplanar encounters.

The results showed that maser models produced for the simulations where $M_{SMS} = 1000\ M_{\odot}$ are the best match for the W1 kilomaser from Gorski et al. [2018]. The model scales correctly to the observed spectrum, it also exhibits two "high-velocity" features with similar fluxes and the left-hand side of the model spectrum shows a similar trend of the flux with the velocity. For larger stars with mass of 10,000 $M_{\odot}$ the high-velocity peaks extend beyond the observed spectrum, starting to resemble megamasers from AGNs. Hence I can conclude that the SMS with 10,000 $M_{\odot}$ is too high a mass for the W1 kilomaser.

Summarising the results presented here, I can confirm that the results support the hypothesis for a supermassive star being present in the forming massive star cluster, and potentially being able to produce the maser spectrum that will be in agreement with the already observed W1 kilomaser, providing that the mass of the SMS will be higher than 1000 $M_{\odot}$ but no larger than 3500 $M_{\odot}$, for the radius of the maser spots estimated in this thesis. In order for the model maser spectrum to have peaks aligned to the observed one, the simulations can be adjusted in terms of the mass of the central star. I have determined the optimal mass to be around 3000 $M_{\odot}$.

The presence of the dense spiral and its movement around the computational grid causes ”high-velocity” features to modulate the peak heights and move them inwards or outwards in the model maser spectra. Hence it would be beneficial to observe the W1 kilomaser with the Very-Long-Baseline Interferometry (VLBI) to obtain more data for another epoch in order to see if there is a slight displacement for the peaks of the ”high-velocity” features. Those findings could potentially confirm the presence of the dense spiral arms moving around the central massive object in the forming superstar cluster in NGC 253.

As a follow-up investigation, I will run the simulations for the three dimensional case and larger computational grid to test if the accretion disk will still be able to produce a water maser and how it will react to the multiple stellar encounters not only in coplanar but also orthogonal orbit, that is known to cause warping of the disk [Clarke and Pringle, 1993].

Appendix

A.1 Appendix 1

```
# The script plots the density, radial and angular velocity maps
# from PLUTO code. It also plots model maser spectrum, together
# with the observed W1 kilomaser from Gorski et al. [2018].
import os
import sys
import matplotlib.pyplot as plt
import matplotlib.tri as tri
import numpy as np
import scipy.interpolate as si
import pyPLUTO as pp
import csv

# Loading the data for W1 kilomaser plot
def Read_Two_Column_File(file_name):
    with open(file_name, 'r') as f_input:
        csv_input = csv.reader(f_input, delimiter=' ',
        skipinitialspace=True)
        x = []
        y = []
        for cols in csv_input:
            x.append(float(cols[0]))
            y.append(float(cols[1]))
    return np.array(x), np.array(y)

W1_v, W1_f = Read_Two_Column_File('W1data.asc')

# Units
au = 1.496e13
pc = 3.0856e18
Mpc = 1.e6 * pc
mp = 1.6e-24
M_sol = 1.989e33
r_i = 10. #*au
r_o = 1000. #*au
```

```
Mdisk = 100.*M_sol
time_output = 8.e8
secinyrs = 3.14e7
years = int(time_output/secinyrs)

# Loading the data into a pload object D.
plutodir = os.environ['PLUTO_DIR']
wdir = plutodir+'/Test_Problems/HD/SMS_final/1000au_Rout/
100Mdisk/1per100yrs/10000yrs_50x100res/'
nlinf = pp.nlast_info(w_dir=wdir,datatype='dbl')


for ifile in range(200,nlinf['nlast']+1):
    D = pp.pload.pload(ifile,w_dir=wdir,datatype='dbl')
    rho = np.squeeze(np.transpose(D.rho))
    vr =  np.squeeze(np.transpose(D.vx1))
    vphi =  np.squeeze(np.transpose(D.vx3))
    radii = D.x1/au
    angles = D.x3
    n_angles = len(angles)
    n_radii = len(radii)
    angles = np.repeat(angles[..., np.newaxis], n_radii, axis=1)
    angles[:, 1::2] += np.pi / n_angles
    x = (radii * np.cos(angles)).flatten()
    y = (radii * np.sin(angles)).flatten()

    rho_f = np.log10(rho.flatten())
    # replace logrho values less than -2, with -2
    np.place(rho_f, rho_f < -20, -20)
    # Create the Triangulation; no triangles so
    Delaunay triangulation created.
    triang = tri.Triangulation(x, y)
    # Mask off unwanted triangles.
    triang.set_mask(np.hypot(x[triang.triangles].mean(axis=1),
                             y[triang.triangles].mean(axis=1))
                    < min_radius)
    fig1, ax1 = plt.subplots()
    ax1.set_aspect('equal')
    levels = np.linspace(-20., -10.)
    tcf = ax1.tricontourf(triang, rho_f, levels=levels, cmap='viridis')
    cbar = fig1.colorbar(tcf, ticks=[-10, -12, -14, -16, -18, -20])
    cbar.set_label(r'g␣cm$^{-3}$,␣log')
    ax1.set_xlabel(r'x')
    ax1.set_ylabel(r'y')
    time = str((ifile)*years)
    textstr = time+r'␣yrs'
    props = dict(boxstyle='round', facecolor='white', alpha=0.0)
```

```
ax1.text(0.78, 0.96, textstr, transform=ax1.transAxes,
fontsize=10, verticalalignment='top', bbox=props)
ax1.set_title(r'Log␣$\rho$')
plt.savefig('fig_logrho_'+str(ifile).zfill(3)+'.png')

vr_f = (vr.flatten()/1.e5)
# Create the Triangulation; no triangles so
Delaunay triangulation created.
triang = tri.Triangulation(x, y)
# Mask off unwanted triangles.
triang.set_mask(np.hypot(x[triang.triangles].mean(axis=1),
                         y[triang.triangles].mean(axis=1))
                < min_radius)
fig2, ax1 = plt.subplots()
ax1.set_aspect('equal')
tcf = ax1.tricontourf(triang, vr_f)
cbar = fig2.colorbar(tcf)
cbar.set_label(r'km␣s$^{-1}$')
ax1.set_xlabel(r'x')
ax1.set_ylabel(r'y')
ax1.text(0.78, 0.96, textstr, transform=ax1.transAxes,
fontsize=10, verticalalignment='top', bbox=props)
ax1.set_title(r'Radial␣velocity')
plt.savefig('fig_vr_'+str(ifile).zfill(3)+'.png')

vphi_f = (vphi.flatten()/1.e5)
# Create the Triangulation; no triangles so
Delaunay triangulation created.
triang = tri.Triangulation(x, y)
# Mask off unwanted triangles.
triang.set_mask(np.hypot(x[triang.triangles].mean(axis=1),
                         y[triang.triangles].mean(axis=1))
                < min_radius)
fig3, ax1 = plt.subplots()
ax1.set_aspect('equal')
tcf = ax1.tricontourf(triang, vphi_f)
cbar = fig3.colorbar(tcf)
cbar.set_label(r'km␣s$^{-1}$')
ax1.set_xlabel(r'x')
ax1.set_ylabel(r'y')
ax1.text(0.78, 0.96, textstr, transform=ax1.transAxes,
fontsize=10, verticalalignment='top', bbox=props)
ax1.set_title(r'Rotation␣velocity')
plt.savefig('fig_vphi_'+str(ifile).zfill(3)+'.png')

# spectrum
# l.o.s. = y
```

```
phi = np.arctan2(y,x)
vy_f = vr_f * np.sin(phi) + vphi_f * np.cos(phi) # in km/s
# Cartesian gridding
res = 1000
default_rho = np.min(rho_f)
points = np.transpose(np.array([x,y]))
xc = np.linspace(np.min(x),np.max(x),res)
yc = np.linspace(np.min(y),np.max(y),res)
dy = yc[2] - yc[1]
grid_x, grid_y = np.meshgrid( xc, yc )
rhoc = si.griddata(points,rho_f,(grid_x,grid_y),
                   method='cubic',fill_value=default_rho)
vyc = si.griddata(points,vy_f,(grid_x,grid_y),
                   method='cubic',fill_value=0.)
nbins = 100
vbin_range = 250 # km/s
vblo = -vbin_range/2
vbhi = vbin_range/2
vbins = np.linspace(vblo,vbhi,nbins)
fluxes = np.zeros(nbins)
# Distance to NGC 253, Gorski+2019
D = 3.5 * Mpc
# Central velocity of superstarcluster, Gorski+2019
V_SSC = 115  # kms, estimated from Fig. 4
# Kartje + 1999 Apj 513:180 eq (3
F0 = 4.7e17 / D**2
rhoc = 10**(rhoc)
rho_lim_lo = 1.e9 * mp
rho_lim_hi = 1.e16 * mp
for ix in range(res):
    for iy in range(res):
        if (rhoc[ix,iy]>rho_lim_lo):
            if (rhoc[ix,iy]<rho_lim_hi):
                iv = int (nbins*(vyc[ix,iy]-vblo)/vbin_range)
                if iv < 0:
                    iv = 0
                if iv > nbins - 2:
                    iv = nbins -1
                fluxes[iv] += F0 * (dy*au)**2

# normalise to Gorski 2019 units:
# we assume source unresolved, so the Jy we get are the Jy for
# the beam we have, i.e., fluxes is in Jy per beam
plt.figure()
plt.plot(vbins+V_SSC,fluxes*1000, label="Model x 20")
plt.plot(W1_v,W1_f*1000., label = "Gorski et al. (2019)")
plt.xlabel("Velocity (km/s)")
```

```
plt.ylabel("Flux␣Density␣(mJy/beam)")
plt.legend()
plt.savefig('fig_mspec_'+str(ifile).zfill(3)+'.png')
plt.close('all')
```

Bibliography

S. M. Andrews, J. Huang, L. M. Pérez, A. Isella, C. P. Dullemond, N. T. Kurtovic, V. V. Guzmán, J. M. Carpenter, D. J. Wilner, S. Zhang, and et al. The disk substructures at high angular resolution project (dsharp). i. motivation, sample, calibration, and overview. *The Astrophysical Journal*, 869(2):L41, Dec 2018. doi: 10.3847/2041-8213/aaf741. URL http://dx.doi.org/10.3847/2041-8213/aaf741. (cited on Page 53)

M. Audard, P. Ábrahám, M. M. Dunham, J. D. Green, N. Grosso, K. Hamaguchi, J. H. Kastner, A. Kóspál, G. Lodato, M. M. Romanova, and et al. Episodic accretion in young stars. *Protostars and Planets VI*, 2014. doi: 10.2458/azu_uapress_9780816531240-ch017. URL http://dx.doi.org/10.2458/azu_uapress_9780816531240-ch017. (cited on Page 4)

N. Bastian and C. Lardo. Multiple stellar populations in globular clusters. *Annual Review of Astronomy and Astrophysics*, 56(1):83–136, Sep 2018. doi: 10.1146/annurev-astro-081817-051839. URL http://dx.doi.org/10.1146/annurev-astro-081817-051839. (cited on Page 6 and 7)

N. Bastian, I. Cabrera-Ziri, and M. Salaris. A general abundance problem for all self-enrichment scenarios for the origin of multiple populations in globular clusters. *Monthly Notices of the Royal Astronomical Society*, 449(3):3333–3346, Apr 2015. doi: 10.1093/mnras/stv543. URL http://dx.doi.org/10.1093/mnras/stv543. (cited on Page 6)

A. D. Bolatto, S. R. Warren, A. K. Leroy, F. Walter, S. Veilleux, E. C. Ostriker, J. Ott, M. Zwaan, D. B. Fisher, A. Weiss, E. Rosolowsky, and J. Hodge. Suppression of star formation in the galaxy NGC 253 by a starburst-driven molecular wind. *Nature*, 499(7459):450–453, July 2013. doi: 10.1038/nature12351. URL https://ui.adsabs.harvard.edu/abs/2013Natur.499..450B. (cited on Page 12)

C. Brogan, K. Johnson, and J. Darling. Water masers associated with star formation in the antennae galaxies. *The Astrophysical Journal*, 716(1):L51–L56, May 2010. doi: 10.1088/2041-8205/716/1/l51. URL http://dx.doi.org/10.1088/2041-8205/716/1/L51. (cited on Page 15)

E. Carretta, A. Bragaglia, R. G. Gratton, A. Recio-Blanco, S. Lucatello, V. D'Orazi, and S. Cassisi. Properties of stellar generations in globular clusters and relations with global parameters. *Astronomy and Astrophysics*, 516:A55, Jun 2010. doi: 10.1051/0004-6361/200913451. URL http://dx.doi.org/10.1051/0004-6361/200913451. (cited on Page 7)

R. Cesaroni. Outflow, Infall, and Rotation in High-Mass Star Forming Regions. *Astrophysics and Space Science*, 295(1-2):5–17, January 2005. doi: 10.1007/s10509-005-3651-8. URL https://ui.adsabs.harvard.edu/abs/2005Ap&SS.295....5C. (cited on Page 24)

R. Cesaroni, D. Galli, G. Lodato, C. Walmsley, and Qingya Zhang. Disks around young o-b (proto)stars: Observations and theory. *Protostars and Planets V*, 04 2006. (cited on Page 23 and 24)

C. J. Clarke and J. E. Pringle. Accretion disc response to a stellar fly-by. *Monthly Notices of the Royal Astronomical Society*, 261(1):190–202, March 1993. doi: 10.1093/mnras/261.1.190. URL https://ui.adsabs.harvard.edu/abs/1993MNRAS.261..190C. (cited on Page 19, 32, 33, 53, and 60)

R. M Crocker, M. R Krumholz, T. A Thompson, H. Baumgardt, and D. Mackey. Radiation pressure limits on the star formation efficiency and surface density of compact stellar systems. *Monthly Notices of the Royal Astronomical Society*, 481(4):4895–4906, Oct 2018. doi: 10.1093/mnras/sty2659. URL http://dx.doi.org/10.1093/mnras/sty2659. (cited on Page 5)

P. A. Crowther, O. Schnurr, R. Hirschi, N. Yusof, R. J. Parker, S. P. Goodwin, and H. A. Kassim. The r136 star cluster hosts several stars whose individual masses greatly exceed the accepted 150m stellar mass limit. *Monthly Notices of the Royal Astronomical Society*, 408(2):731–751, Jul 2010. doi: 10.1111/j.1365-2966.2010.17167.x. URL http://dx.doi.org/10.1111/j.1365-2966.2010.17167.x. (cited on Page 8)

N. Cuello, G. Dipierro, D. Mentiplay, D. J. Price, C. Pinte, J. Cuadra, G. Laibe, F. Ménard, P. P. Poblete, and M. Montesinos. Flybys in protoplanetary discs: I. gas and dust dynamics. *Monthly Notices of the Royal Astronomical Society*, 483(3):4114–4139, Dec 2018. doi: 10.1093/mnras/sty3325. URL http://dx.doi.org/10.1093/mnras/sty3325. (cited on Page 19, 21, 24, 25, 32, 53, 54, and 59)

D. A. Dale, S. A. Cohen, L. C. Johnson, M. D. Schuster, D. Calzetti, C. W. Engelbracht, A. Gil de Paz, R. C. Kennicutt, J. C. Lee, A. Begum, M. Block, J. J. Dalcanton, J. G. Funes, K. D. Gordon, B. D. Johnson, A. R. Marble, S. Sakai, E. D. Skillman, L. van Zee, F. Walter, D. R. Weisz, B. Williams, S. Y. Wu, and Y. Wu. The Spitzer Local Volume Legacy: Survey Description and Infrared Photometry. *The Astrophysical Journal*, 703(1):517–556, September 2009. doi: 10.1088/0004-637X/703/1/517. URL https://ui.adsabs.harvard.edu/abs/2009ApJ...703..517D. (cited on Page 12)

P. A. Denissenkov and F. D. A. Hartwick. Supermassive stars as a source of abundance anomalies of proton-capture elements in globular clusters. *Monthly Notices of the Royal Astronomical Society*, 437(1):L21–L25, January 2014. doi: 10.1093/mnrasl/slt133. URL https://ui.adsabs.harvard.edu/abs/2014MNRAS.437L..21D. (cited on Page 1 and 7)

M. Elitzur, C. F. McKee, and D. J. Hollenbach. Radiative Transfer in Astronomical Masers. III. Filamentary Masers. *The Astrophysical Journal*, 367:333, January 1991. doi: 10.1086/169632. URL https://ui.adsabs.harvard.edu/abs/1991ApJ...367..333E. (cited on Page 11 and 34)

F. Gao, J. A. Braatz, M. J. Reid, J. J. Condon, J. E. Greene, C. Henkel, C. M. V. Impellizzeri, K. Y. Lo, C. Y. Kuo, D. W. Pesce, J. Wagner, and W. Zhao. The Megamaser Cosmology Project. IX. Black Hole Masses for Three Maser Galaxies. *The Astrophysical Journal*, 834(1):52, January 2017. doi: 10.3847/1538-4357/834/1/52. URL https://ui.adsabs.harvard.edu/abs/2017ApJ...834...52G. (cited on Page 15)

M. Gieles, C. Charbonnel, M. G. H. Krause, V. Hénault-Brunet, O. Agertz, H. J. G. L. M. Lamers, N. Bastian, A. Gualandris, A. Zocchi, and J. A. Petts. Concurrent formation of supermassive stars and globular clusters: implications for early self-enrichment. *Monthly Notices of the Royal Astronomical Society*, 478(2):2461–2479, Apr 2018. doi: 10.1093/mnras/sty1059. URL http://dx.doi.org/10.1093/mnras/sty1059. (cited on Page iii, 1, 5, 6, 7, 8, 9, 10, 11, 25, and 26)

M. D. Gorski, J. Ott, R. Rand, D. S. Meier, E. Momjian, E. Schinnerer, and S. P. Ellingsen. Diagnostics of a nuclear starburst: water and methanol masers. *Monthly Notices of the Royal Astronomical Society*, 483(4):5434–5443, Nov 2018. doi: 10.1093/mnras/sty3077. URL http://dx.doi.org/10.1093/mnras/sty3077. (cited on Page iii, 1, 12, 13, 15, 23, 28, 29, 34, 36, 40, 42, 44, 45, 47, 49, 50, 51, 55, 56, and 59)

R. G. Gratton, E. Carretta, and A. Bragaglia. Multiple populations in globular clusters. *The Astronomy and Astrophysics Review*, 20(1), Feb 2012. doi: 10.1007/s00159-012-0050-3. URL http://dx.doi.org/10.1007/s00159-012-0050-3. (cited on Page 6)

M. D. Gray, A. Baudry, A. M. S. Richards, E. M. L. Humphreys, A. M. Sobolev, and J. A. Yates. The physics of water masers observable with alma and sofia: model predictions for evolved stars. *Monthly Notices of the Royal Astronomical Society*, 456(1):374–404, Feb 2016. doi: 10.1093/mnras/stv2437. URL http://dx.doi.org/10.1093/mnras/stv2437. (cited on Page 11)

L. J. Greenhill, C. Henkel, R. Becker, T. L. Wilson, and J. G. A. Wouterloot. Centripetal acceleration within the subparsec nuclear maser disk of NGC4258. *Astronomy and Astrophysics*, 304:21, December 1995. URL https://ui.adsabs.harvard.edu/abs/1995A&A...304...21G. (cited on Page 13)

L. J. Greenhill, C. R. Gwinn, R. Antonucci, and R. Barvainis. VLBI imaging of water maser emission from the nuclear torus of NGC 1068. *The Astrophysical Journal*, 472(1):L21–L24, nov 1996. doi: 10.1086/310346. URL https://doi.org/10.1086/310346. (cited on Page 13 and 15)

L. J. Greenhill, R. S. Booth, S. P. Ellingsen, J. R. Herrnstein, D. L. Jauncey, P. M. McCulloch, J. M. Moran, R. P. Norris, J. E. Reynolds, and A. K. Tzioumis. A Warped Accretion Disk and Wide-Angle Outflow in the Inner Parsec of the Circinus Galaxy. *The Astrophysical Journal*, 590(1):162—-173, Jun 2003. (cited on Page 15)

Y. Hagiwara, C. Henkel, K. M. Menten, and N. Nakai. Water maser emission from the active nucleus in m51. *The Astrophysical Journal*, 560(1):L37–L40, Oct 2001. doi: 10.1086/324171. URL http://dx.doi.org/10.1086/324171. (cited on Page 11)

C. Henkel, J. A. Braatz, L. J. Greenhill, and A. S. Wilson. Discovery of water vapor megamaser emission from Mrk 1419 (NGC 2960): An analogue of NGC 4258? *Astronomy and Astrophysics*, 394:L23–L26, November 2002. doi: 10.1051/0004-6361:20021297. URL https://ui.adsabs.harvard.edu/abs/2002A&A...394L..23H. (cited on Page 15)

J. R. Herrnstein, J. M. Moran, L. J. Greenhill, P. J. Diamond, M. Inoue, N. Nakai, M. Miyoshi, C. Henkel, and A. Riess. A geometric distance to the galaxy ngc4258 from orbital motions in a nuclear gas disk. *Nature*, 400(6744):539–541, Aug 1999. doi: 10.1038/22972. URL http://dx.doi.org/10.1038/22972. (cited on Page 13)

J. G. Hills. The effect of mass loss on the dynamical evolution of a stellar system - Analytic approximations. *Astrophysical Journal*, 235:986–991, February 1980. doi: 10.1086/157703. URL https://ui.adsabs.harvard.edu/abs/1980ApJ...235..986H. (cited on Page 5 and 6)

J. G. Hills and C. A. Day. Stellar Collisions in Globular Clusters. *Astrophysics Letters*, 17:87, February 1976. URL https://ui.adsabs.harvard.edu/abs/1976ApL....17...87H. (cited on Page 8)

Y. Ishihara, N. Nakai, N. Iyomoto, K. Makishima, P. Diamond, and P. Hall. Water-Vapor Maser Emission from the Seyfert 2 Galaxy IC 2560: Evidence for a Super-Massive Black Hole. *Publications of the Astronomical Society of Japan*, 53(2): 215–225, Apr 2001. doi: 10.1093/pasj/53.2.215. (cited on Page 15)

J. F. Kartje, A. Konigl, and M. Elitzur. Megamaser disks in active galactic nuclei. *The Astrophysical Journal*, 513(1):180–196, Mar 1999. doi: 10.1086/306824. URL http://dx.doi.org/10.1086/306824. (cited on Page iii, 11, 12, 29, 35, and 55)

H. Klahr and W. Kley. 3D-radiation hydro simulations of disk-planet interactions. I. Numerical algorithm and test cases. *Astronomy Astrophysics*, 445(2):747–758, January 2006. doi: 10.1051/0004-6361:20053238. URL https://ui.adsabs.harvard.edu/abs/2006A&A...445..747K. (cited on Page 19)

R. S. Klessen, F. Heitsch, and Mordecai-Mark Mac Low. Gravitational collapse in turbulent molecular clouds. i. gasdynamical turbulence. *The Astrophysical Journal*, 535(2):887–906, Jun 2000. doi: 10.1086/308891. URL http://dx.doi.org/10.1086/308891. (cited on Page 3)

P. T. Kondratko, L. J. Greenhill, and J. M. Moran. The Parsec-Scale Accretion Disk in NGC 3393. *The Astrophysical Journal*, 678(1):87–95, May 2008. doi: 10.1086/586879. URL https://ui.adsabs.harvard.edu/abs/2008ApJ...678...87K. (cited on Page 15)

M. Krause, C. Charbonnel, T. Decressin, G. Meynet, and N. Prantzos. Superbubble dynamics in globular cluster infancy. *Astronomy Astrophysics*, 552:A121, Apr 2013. doi: 10.1051/0004-6361/201220694. URL http://dx.doi.org/10.1051/0004-6361/201220694. (cited on Page 5)

M. G. H. Krause, S. S. R. Offner, C. Charbonnel, M. Gieles, R. S. Klessen, E. Vázquez-Semadeni, J. Ballesteros-Paredes, P. Girichidis, J. M. Diederik Kruijssen, J. L. Ward, and et al. The physics of star cluster formation and evolution. *Space Science Reviews*, 216(4), Jun 2020. doi: 10.1007/s11214-020-00689-4. URL http://dx.doi.org/10.1007/s11214-020-00689-4. (cited on Page 1, 3, 4, 5, 6, and 7)

M. R. Krumholz, C. F. McKee, and J. Bland-Hawthorn. Star Clusters Across Cosmic Time. *Annual Review of Astronomy and Astrophysics*, 57:227–303, August 2019. doi: 10.1146/annurev-astro-091918-104430. URL https://ui.adsabs.harvard.edu/abs/2019ARA&A..57..227K. (cited on Page 4)

M. A. Kuhn, L. A. Hillenbrand, A. Sills, E. D. Feigelson, and K. V. Getman. Kinematics in young star clusters and associations withgaiadr2. *The Astrophysical Journal*, 870(1):32, Jan 2019. doi: 10.3847/1538-4357/aaef8c. URL http://dx.doi.org/10.3847/1538-4357/aaef8c. (cited on Page 5)

C. Y. Kuo, J. A. Braatz, J. J. Condon, C. M. V. Impellizzeri, K. Y. Lo, I. Zaw, M. Schenker, C. Henkel, M. J. Reid, and J. E. Greene. The Megamaser Cosmology Project. III. Accurate Masses of Seven Supermassive Black Holes in Active Galaxies with Circumnuclear Megamaser Disks. *The Astrophysical Journal*, 727(1):20, January 2011. doi: 10.1088/0004-637X/727/1/20. URL https://ui.adsabs.harvard.edu/abs/2011ApJ...727...20K. (cited on Page 15)

C. Y. Kuo, J. A. Braatz, K. Y. Lo, M. J. Reid, S. H. Suyu, D. W. Pesce, J. J. Condon, C. Henkel, and C. M. V. Impellizzeri. The megamaser cosmology project. vi. observations of ngc 6323. *The Astrophysical Journal*, 800(1):26, 11 2014. doi: 10.1088/0004-637x/800/1/26. URL http://dx.doi.org/10.1088/0004-637X/800/1/26. (cited on Page 15)

C. J. Lada and E. A. Lada. Embedded clusters in molecular clouds. *Annual Review of Astronomy and Astrophysics*, 41(1):57–115, Sep 2003. doi: 10.1146/annurev.astro.41.011802.094844. URL http://dx.doi.org/10.1146/annurev.astro.41.011802.094844. (cited on Page 4)

C. C. Lin, L. Mestel, and F. H. Shu. The Gravitational Collapse of a Uniform Spheroid. *The Astrophysical Journal*, 142:1431, nov 1965. doi: 10.1086/148428. URL https://ui.adsabs.harvard.edu/abs/1965ApJ...142.1431L. (cited on Page 3)

E. Maoz and C. F. McKee. Doppler shift asymmetry in high-velocity maser emission from shocks in circumnuclear disks. *The Astrophysical Journal*, 494(1):218–235, Feb 1998. doi: 10.1086/305186. URL http://dx.doi.org/10.1086/305186. (cited on Page 56)

R. Meire. An Efficient Method for Solving Barker's Equation. *Journal of the British Astronomical Association*, 95:113, April 1985. URL https://ui.adsabs.harvard.edu/abs/1985JBAA...95..113M. (cited on Page 21)

A. Mignone, G. Bodo, S. Massaglia, T. Matsakos, O. Tesileanu, C. Zanni, and A. Ferrari. Pluto: A numerical code for computational astrophysics. *The Astrophysical Journal Supplement Series*, 170(1):228–242, May 2007. doi: 10.1086/513316. URL http://dx.doi.org/10.1086/513316. (cited on Page 17)

A. Mignone, M. Flock, M. Stute, S. M. Kolb, and G. Muscianisi. A conservative orbital advection scheme for simulations of magnetized shear flows with the pluto code. *Astronomy Astrophysics*, 545:A152, Sep 2012. doi: 10.1051/0004-6361/201219557. URL http://dx.doi.org/10.1051/0004-6361/201219557. (cited on Page 18 and 19)

A. P. Milone, A. F. Marino, A. Renzini, F. D'Antona, J. Anderson, B. Barbuy, L. R. Bedin, A. Bellini, T. M. Brown, S. Cassisi, G. Cordoni, E. P. Lagioia, D. Nardiello, S. Ortolani, G. Piotto, A. Sarajedini, M. Tailo, R. P. van der Marel, and E. Vesperini. The Hubble Space Telescope UV legacy survey of galactic globular clusters - XVI. The helium abundance of multiple populations. *Monthly Notices of the Royal Astronomical Society*, 481(4):5098–5122, December 2018. doi: 10.1093/mnras/sty2573. URL https://ui.adsabs.harvard.edu/abs/2018MNRAS.481.5098M. (cited on Page 6)

N. Moeckel and C. J. Clarke. Collisional formation of very massive stars in dense clusters. *Monthly Notices of the Royal Astronomical Society*, 410(4):2799–2806, Jan 2011. doi: 10.1111/j.1365-2966.2010.17659.x. URL http://dx.doi.org/10.1111/j.1365-2966.2010.17659.x. (cited on Page 5 and 8)

T. Murayama and Y. Taniguchi. Why does ngc 1068 have a more powerful active galactic nucleus than ngc 4258? *Publications of the Astronomical Society of Japan*, 49(4):L13–L18, Aug 1997. doi: 10.1093/pasj/49.4.l13. URL http://dx.doi.org/10.1093/pasj/49.4.L13. (cited on Page 12)

W. Osborn. Two new CN-strong globular cluster stars. *The Observatory*, 91:223–224, December 1971. URL https://ui.adsabs.harvard.edu/abs/1971Obs....91..223O. (cited on Page 1)

D. W. Pesce, J. A. Braatz, J. J. Condon, F. Gao, C. Henkel, E. Litzinger, K. Y. Lo, and M. J. Reid. The megamaser cosmology project. vii. investigating disk physics using spectral monitoring observations. *The Astrophysical Journal*, 810(1):65, Aug 2015. doi: 10.1088/0004-637x/810/1/65. URL http://dx.doi.org/10.1088/0004-637X/810/1/65. (cited on Page 13, 14, 24, and 55)

M. J. Reid, J. A. Braatz, J. J. Condon, L. J. Greenhill, C. Henkel, and K. Y. Lo. The Megamaser Cosmology Project. I. Very Long Baseline Interferometric Observations of UGC 3789. *The Astrophysical Journal*, 695(1):287–291, April 2009. doi: 10.1088/0004-637X/695/1/287. URL https://ui.adsabs.harvard.edu/abs/2009ApJ...695..287R. (cited on Page 15)

A. Sandage and R. Wildey. The Anomalous Color-Magnitude Diagram of the Remote Globular Cluster NGC 7006. *The Astrophysical Journal*, 150:469, November 1967. doi: 10.1086/149350. URL https://ui.adsabs.harvard.edu/abs/1967ApJ...150..469S. (cited on Page 1)

N. Sato, A. Yamauchi, Y. Ishihara, K. Sorai, N. Kuno, N. Nakai, R. Balasubramanyam, and P. Hall. Water-Vapor Maser Survey for Active Galactic Nuclei: A Megamaser in NGC 6926. *Publications of the Astronomical Society of Japan*, 57:587–594, August 2005. doi: 10.1093/pasj/57.4.587. URL https://ui.adsabs.harvard.edu/abs/2005PASJ...57..587S. (cited on Page 15)

Jr. Spitzer, L. Disruption of Galactic Clusters. *The Astrophysical Journal*, 127:17, January 1958. doi: 10.1086/146435. URL https://ui.adsabs.harvard.edu/abs/1958ApJ...127...17S. (cited on Page 6)

J. S. Urquhart, L. K. Morgan, C. C. Figura, T. J. T. Moore, S. L. Lumsden, M. G. Hoare, R. D. Oudmaijer, J. C. Mottram, B. Davies, and M. K. Dunham. The red msx source survey: ammonia and water maser analysis of massive star-forming regions. *Monthly Notices of the Royal Astronomical Society*, 418(3):1689–1706, Oct 2011. doi: 10.1111/j.1365-2966.2011.19594.x. URL http://dx.doi.org/10.1111/j.1365-2966.2011.19594.x. (cited on Page 15)

E. Vázquez-Semadeni, A. González-Samaniego, and P. Colín. Hierarchical star cluster assembly in globally collapsing molecular clouds. *Monthly Notices of the Royal Astronomical Society*, 467(2):1313–1328, May 2017. doi: 10.1093/mnras/stw3229. URL https://ui.adsabs.harvard.edu/abs/2017MNRAS.467.1313V. (cited on Page 3)

E. Vázquez-Semadeni, A. Palau, J. Ballesteros-Paredes, G. C. Gómez, and M. Zamora-Avilés. Global hierarchical collapse in molecular clouds. towards a comprehensive scenario. *Monthly Notices of the Royal Astronomical Society*, 490(3):3061–3097, Oct 2019. doi: 10.1093/mnras/stz2736. URL http://dx.doi.org/10.1093/mnras/stz2736. (cited on Page 3)

A. M. Watson, III Gallagher, J. S., J. A. Holtzman, J. J. Hester, J. R. Mould, G. E. Ballester, C. J. Burrows, S. Casertano, J. T. Clarke, D. Crisp, R. Evans, R. E. Griffiths, J. G. Hoessel, P. A. Scowen, K. R. Stapelfeldt, J. T. Trauger, and J. A. Westphal. The Discovery of Young, Luminous, Compact Stellar Clusters in the Starburst Galaxy NGC 253. *The Astronomical Journal*, 112:534, August 1996. doi: 10.1086/118032. URL https://ui.adsabs.harvard.edu/abs/1996AJ....112..534W. (cited on Page 12)

A. Yamauchi, N. Nakai, N. Sato, and P. Diamond. Water-Vapor Maser Disk at the Nucleus of the Seyfert 2 Galaxy NGC 3079. *Publications of the Astronomical Society of Japan*, 56(4):605–619, Aug 2004. doi: 10.1093/pasj/56.4.605. URL ttps://doi.org/10.1093/pasj/56.4.605. (cited on Page 15)

S. Zhang, Z. Zhu, J. Huang, V. V. Guzmán, S. M. Andrews, T. Birnstiel, C. P. Dullemond, J. M. Carpenter, A. Isella, L. M. Pérez, and et al. The disk substructures at high angular resolution project (dsharp). vii. the planet–disk interactions interpretation. *The Astrophysical Journal*, 869(2):L47, Dec 2018. doi: 10.3847/2041-8213/aaf744. URL http://dx.doi.org/10.3847/2041-8213/aaf744. (cited on Page 53)

W. Zhao, J. A. Braatz, J. J. Condon, K. Y. Lo, M. J. Reid, C. Henkel, D. W. Pesce, J. E. Greene, F. Gao, C. Y. Kuo, and C. M. V. Impellizzeri. The Megamaser Cosmology Project. X. High-resolution Maps and Mass Constraints for SMBHs. *The Astrophysical Journal*, 854(2):124, February 2018. doi: 10.3847/1538-4357/aaa95c. URL https://ui.adsabs.harvard.edu/abs/2018ApJ...854..124Z. (cited on Page 15)

I herewith assure that I wrote the present thesis independently, that the thesis has not been partially or fully submitted as graded academic work and that I have used no other means than the ones indicated. I have indicated all parts of the work in which sources are used according to their wording or to their meaning.

Hatfield, 30th September 2021